

Aerodynamic characteristics of a mission-adaptive stealthy air inlet

Louwrens Marais

Thesis presented in partial fulfilment
of the requirements for the degree of
Master of Science in Engineering
at the University of Stellenbosch.



Study leader: Prof. G.D. Thiart

December 2003

Declaration

I, the undersigned, hereby declare that the work contained in this thesis is my own original work and that I have not previously in its entirety or in part submitted it at any university for a degree.

Signature

Date

Abstract

The aerodynamic performance of a mission-adaptive air inlet for a stealthy unmanned aircraft was examined using CFX 5.5, a commercial Computational Fluid Dynamics package.

In order to ensure that the numerical results were reliable, the package was validated against a number of flow situations for which previously-known results exist. This was done for both external and internal flow, and in all cases the conclusion could be made that the code produces realistic results.

The simulation of the inlet was done in two steps. A first-order design was simulated using robust simulation parameters: the focus was on obtaining a “picture” of the flow into the inlet, not on the quantitative values of flow variables. On account of the results of these simulations, the design was suitably modified. This second-order design was then simulated using more accurate simulation parameters, and the results analysed in detail. Comparative simulations between the two design iterations showed that their pressure recoveries are similar, but that the distortion of the velocity profile at the engine compressor face is lower for the second-order design than for the first-order design over a significant portion of the operational range.

When compared with an idealized theoretical analysis, the numerical results showed that the performance of the inlet was severely degraded at most operating conditions. This is mainly due to the effects of flow separation ahead of the inlet capture plane. To alleviate this problem, recommendations for the modification of the design are proposed.

This thesis demonstrates that CFD is a valuable tool for both qualitative and quantitative evaluation of performance during the design process of an air inlet.

Opsomming

Die lugdinamiese werkverrigting van 'n missie-aanpasbare luginlaat vir 'n radarontduikende onbemande vliegtuig is ondersoek, deur gebruik te maak van CFX 5.5, 'n kommersiële numeriese vloeddinamika-sagteware pakket.

Om te verseker dat die numeriese resultate betroubaar was, is die pakket gevalideer teen 'n aantal gevalle waarvoor vooraf-bekende resultate bestaan. Dit is gedoen vir beide interne en eksterne vloei, en die gevolgtrekking kon gemaak word dat die kode wel realistiese resultate lewer.

Die simulاسie van die inlaat is in twee stappe gedoen. 'n Eerste-orde ontwerp is gesimuleer deur gebruik te maak van robuuste simulاسieparameters: die fokus hiervan was om 'n visuele indruk van die vloeioptrone in die inlaat te kry, nie op kwantitatiewe waardes van die vloei veranderlikes nie. Na aanleiding van hierdie resultate van hierdie simulاسies is die ontwerp dienoreenkomstig aangepas. Hierdie tweede orde ontwerp is dan gesimuleer deur gebruik te maak van meer akkurate simulاسieparameters, en die resultate is in detail geanaliseer. Vergelykende simulاسies tussen die twee ontwerp-iterاسies het gewys dat hulle drukherwinnings soortgelyk is, maar dat die distorsie in die snelheidsprofiel by die enjin kompressor-vlak laer is vir die tweede-orde ontwerp as vir die eerste-orde ontwerp, oor 'n beduidende gedeelte van die operasionele bestek.

Wanneer dit met 'n ideale teoretiese analise vergelyk word, het die numeriese resultate getoon dat die werkverrigting van die inlaat ernstig gedegradeer is by meeste operasionele toestande. Dit kan meestal toegeskryf word aan die effekte van vloei-wegbreking voor die intreevlak van die inlaat. Om hierdie probleem te verlig, word aanbevelings vir die aanpassing van die ontwerp voorgestel.

Hierdie tesis demonstreer dat numeriese vloeddinamika waardevolle gereedskap is vir beide kwalitatiewe en kwantitatiewe evaluering van werkverrigting tydens die ontwerpproses van 'n luginlaat.

Acknowledgements

Firstly, thank you to Professor Thiart for your guidance during this project. Thanks for figuring out how to approach it when I ran out of ideas. Thanks for lending me your computer to crunch the numbers, and for keeping on asking: “How do you know it is right?”

Thank you to my family and friends, who supported me during the whole of my Master’s. Special thanks goes to my mother for being so strong without me there. Cheers to the guys at Beer Club, for sharing one of the few certainties in life; to those who have done this before: Johann, Hano and Anthony, thank you for your encouragement and advice on how (and how not) to do it.

I remember Detlef Grygier, who passed away while working hard to bring a unique idea to reality.

To the Source of all the knowledge goes my greatest thanks, for You Created physics, and then gave us curiosity...

THERE IS AN ART ... OR RATHER, A KNACK TO FLYING.
THE KNACK LIES IN LEARNING HOW TO THROW YOURSELF AT THE GROUND
AND MISS.

— *Life, the universe and everything*
Douglas Adams

Contents

List of Symbols	ix
List of Abbreviations	xi
1 Introduction	1
1.1 Scope of thesis	1
1.2 Stealth technology	2
1.3 Inlet aerodynamic considerations	5
1.4 Current developments	8
1.4.1 Boeing X-45	8
1.4.2 Northrop Grumman X-47	9
1.5 Thesis objectives	9
1.6 First-order design of inlet	10
1.7 Thesis overview	12
2 Validation of CFD package: external flow	13
2.1 Objectives	13
2.2 Validation results	14
2.2.1 Flat Plate	14
2.2.2 Axi-symmetric Rankine halfbody	20
2.2.3 Sphere	23
2.3 Closure	27
3 Validation of CFD package: internal flow	28
3.1 Objectives	28
3.2 Validation results	29
3.2.1 Circular pipe	29
3.2.2 Two-dimensional diffuser	33
3.2.3 RAE inlet model 2129	37
3.3 Closure	41
4 CFD modelling of first-order design; redesign	43

4.1	Background	43
4.2	Numerical simulation	43
4.2.1	CFD models	43
4.2.2	Simulation results	47
4.2.3	Conclusions from simulation results	50
4.3	Redesign	51
4.3.1	Inlet entrance	51
4.3.2	Bump geometry	51
4.4	Closure	52
5	CFD modelling of second-order design	53
5.1	Objectives	53
5.2	CFD model	53
5.3	Inlet performance	58
5.3.1	Theoretical prediction	58
5.3.2	Numerical results	59
5.3.3	Comparison between first and second-order designs	74
6	Conclusion	78
6.1	Review of thesis objectives	78
6.2	Recommendations for redesign of inlet	79
6.3	General conclusions	80
6.4	Recommendations for further work	80
6.5	Closure	81

Appendices

A	Details of conceptual UCAV and preliminary inlet design	82
A.1	Background	82
A.2	Mission profiles	82
A.3	Airframe geometry	82
A.4	Engine	83
A.5	Design specifications	86
A.6	Preliminary concept design	87
A.7	Detailed design	87
A.7.1	External inlet configuration	87
A.7.2	Internal inlet configuration	89
B	Background information on CFX 5.5	92
B.1	Objectives	92
B.2	Governing equations	92

B.3	Meshing	93
B.4	Turbulence modelling	95
	B.4.1 $k - \epsilon$ model	96
	B.4.2 SST model	96
B.5	Boundary conditions	98
	B.5.1 Inlet	98
	B.5.2 Outlet	98
	B.5.3 Opening	98
	B.5.4 Wall	99
	B.5.5 Symmetry plane	99
	B.5.6 Periodic pair	99
B.6	Advection schemes	99
C	Details of CFD models for validation cases	101
C.1	Flat plate	102
	C.1.1 Structured mesh	102
	C.1.2 Unstructured mesh	105
C.2	Rankine halfbody	108
C.3	Sphere	111
C.4	Pipe flow	114
	C.4.1 Structured grid	114
	C.4.2 Unstructured grid	117
C.5	Two-dimensional diffuser	120
C.6	M2129 inlet	122
	C.6.1 Low mass flow case	122
	C.6.2 High mass flow case	124
D	Details of CFD models for UCAV inlet simulations	126
D.1	First-order design	127
	D.1.1 Bump down	127
	D.1.2 Bump up	131
D.2	Second-order design	134
	D.2.1 Bump down	134
	D.2.2 Bump up	142
	References	147

List of Symbols

General

γ	Ratio of specific heats, taken as 1.4 for air
η	Inlet pressure recovery
μ	Inverse flow ratio A_c/A_∞
ρ	Density
a	Velocity of sound
A	Cross-sectional area
A^*	Sonic area
C_p	Pressure coefficient
g	Gravitational constant
\dot{m}	Mass flow
M	Mach number
p	Static pressure
P	Total (stagnation) pressure
q	Dynamic pressure
R	Gas constant, taken as 287.1 [J/kg·K] for air
Re	Reynolds number
T	Temperature
V	Velocity of flow
x	Distance in bulk flow direction, usually measured from stagnation point (external flow) or entrance (internal flow)
y^+	Dimensionless distance from wall

Subscripts

0	Stagnation values of flow quantities other than pressure
1st	Refers to a variable value applicable to the first-order design
2nd	Refers to a variable value applicable to the second-order design
∞	Free stream conditions
ave	Refers to average value of a variable
bd	UCAV bump down
bu	UCAV bump up

Subscripts (continued)

c	Variable value at inlet capture plane
f	Variable value at engine face plane
$known$	Refers to previously known value of a variable
num	Refers to numerically calculated value of a variable
th	Refers to theoretical value of a variable

Chapter 1

$C_{\Delta P}$	Coefficient of total pressure loss
C_{Fa}	Friction coefficient on approach
C_{Fd}	Friction coefficient in duct
I	Duct integral
J	Corrected position ratio
k	Constant in J
ℓ	Local distance on inlet duct
φ	Local perimeter of duct
S	Wetted area ahead of inlet

Chapter 2

ϕ	Generic variable
φ	Geometric angle on Rankine halfbody and sphere
C_f	Local friction coefficient
D	Asymptotic diameter of Rankine halfbody

Chapter 3

d	Pipe diameter
D	Engine face diameter of M2129 inlet
f	Darcy friction factor
H	Entrance height of 2D asymmetric diffuser
L	Pipe length
L_e	Pipe entrance length
u	Local flow velocity
U_b	Bulk flow velocity

Chapter 5

α	Kinetic energy correction factor
----------	----------------------------------

Appendix B

ε	Turbulence eddy dissipation
μ	Dynamic viscosity
μ_t	Eddy viscosity
ω	Turbulence frequency
k	Turbulence kinetic energy

List of Abbreviations

AA	Anti-Aircraft
AAM	Air-to-Air Missile
AGARD	Advisory Group for Aeronautical Research and Development
CAD	Computer Aided Design
CFD	Computational Fluid Dynamics
IGES	Initial Graphics Exchange Specification
IR	Infrared
M2129	RAE inlet model 2129
RAE	Royal Aeronautic Establishment
RAM (Chapter 1)	Radar Absorbent Material
RAM (Chapter 5)	Random Access Memory
RANSE	Reynolds Averaged Navier-Stokes Equations
RCS	Radar Cross Section
SAM	Surface-to-Air Missile
SST	Shear Stress Transport (turbulence model)
UAV	Unmanned Air Vehicle
UCAV	Unmanned Combat Air Vehicle
UDS	Upwind Differencing Scheme

Chapter 1

Introduction

1.1 Scope of thesis

In order to limit aircrew losses in combat operations, unmanned air vehicles (UAVs) have been used for around three decades on high-risk operations such as tactical reconnaissance on highly defended targets. The recent advances in computer processing power made possible the development of UAVs that can operate autonomously, as opposed to earlier aircraft that were remote-controlled, or flew a specific pre-programmed route or mission. This sparked a renewed interest in UAVs as viable military systems.

A military aircraft must generally operate unobserved by the enemy for as long as possible if it is to complete its mission successfully. In a modern war theatre, detection risks in the form of advanced radar and infrared (IR) systems make it increasingly difficult for “normal” aircraft to operate safely. Stealth technology developed since the late 1970’s aim to overcome this problem by reducing the Radar Cross Section (RCS), IR signature and visual signature of aircraft, thereby minimising the risk of detection.

The advances in UAV and stealth technologies led to the emergence of Unmanned Combat Air Vehicles (UCAVs) that rely on stealth to avoid detection, and perform missions ranging from reconnaissance to surgical strikes [1, 2, 3, 4, 7, 8].

Air inlets are large contributors to the overall RCS of an aircraft. This contribution has to be minimised on a stealth aircraft [1, 2, 3]. Because of reasons dicussed in sections 1.2 and 1.3, an air inlet with good stealth characteristics generally has a reduced aerodynamic efficiency, however. A possible solution to this problem is to employ a mission-adaptive inlet which changes shape as the detection threat changes, thereby enabling it to operate more efficiently during low-threat stages of the aircraft mission. This thesis documents the aerodynamic performance evaluation of such a mission-adaptive inlet for a conceptual UCAV.

1.2 Stealth technology

The two main (non-visual) methods that are employed to detect aircraft, are infrared and radar. In designing stealth aircraft, the aim therefore is to minimise the IR signature and RCS.

The largest contributor to the total IR signature of a gas turbine powered aircraft will normally be at the engine exhaust. This signature can be reduced by increasing the area where gas flow mixing occurs, and by ducting cold air from the atmosphere to mix with the exhaust in order to provide cooling.

A further significant contributor to the IR signature is stagnation heating on sharp edges and corners, where the flow comes to a complete rest and kinetic energy is converted into high temperature and pressure. This typically occurs on leading edges and inlet lips. The aerodynamic heating effects of stagnation can be reduced by minimising sharp edges and corners [1, p.1515].

IR detection is normally used for short-range acquisition. For targets that are further away, radar is the main method of detection. It can normally be assumed that once an aircraft is within IR detection range, it would have already been detected by radar, even if it were stealthy. For this reason, minimising the RCS takes priority over reducing the IR signature. Fixing “trouble spots” of high IR signature is also generally easier than those of high RCS.

When the electromagnetic field generated by a radar transmitter encounters a target, the energy returned to the receiver is a combination of three phenomena, namely specular reflection, diffraction and travelling and creeping waves [2, p.1353]. These collectively account for the measured RCS of a target. Specular reflection is the strongest scattering mechanism in non-stealthy designs [3, p.7].

Specular reflection (where incident and reflection angles are equal, like that from a mirror) is reduced mostly through shaping of the airframe and the external components of the aircraft to deflect reflected radar energy away from radar receivers. Diffraction and travelling waves are normally attenuated using Radar Absorbent Materials (RAM). RAM would also be applied to cure local “problem areas” on a given geometry. It comes in two varieties, namely electric and magnetic RAM. As the name implies, they work by dissipating the electric and magnetic components of the incident radar energy, respectively [4, pp.271-2].

The measured RCS of an aircraft, in units of $[dB m^2]$, is a function of the direction from which it is illuminated, and can be represented with a polar plot, as in Figure 1.1.

For a new design the planned missions therefore have to be properly defined, in order to

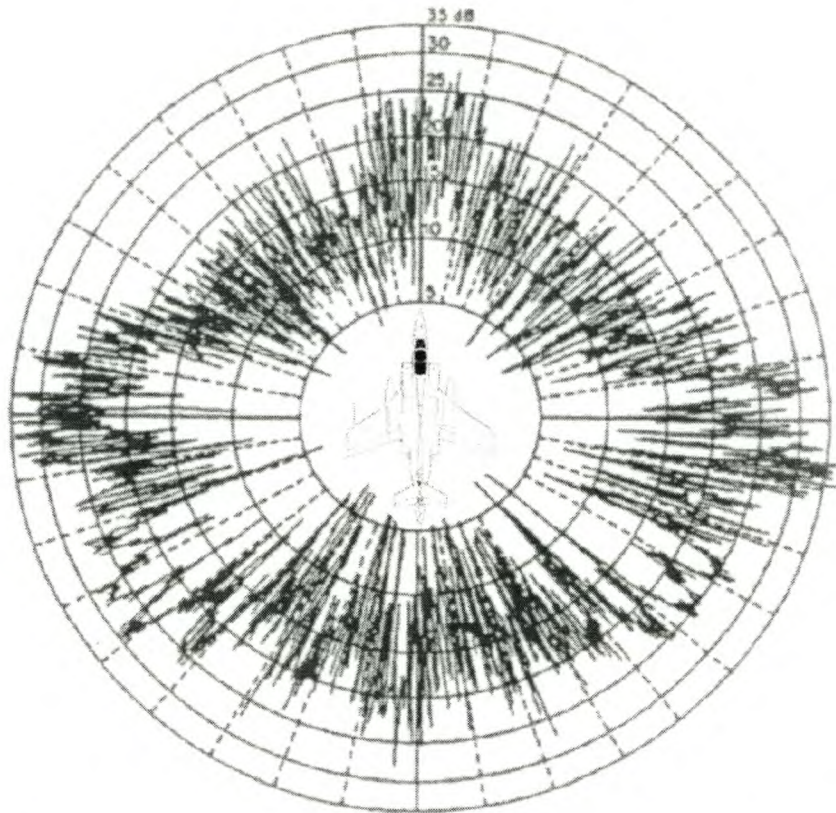


Figure 1.1: Typical RCS polar plot for a non-stealthy aircraft [2]

determine threat sectors. The most critical region is normally the front angular sector, typically $\pm 45^\circ$ in azimuth and $\pm 15^\circ$ in elevation (figure 1.2). Side and rear sectors are less important [4, p.279]. It has to be remembered that both ground-based and airborne radar constitutes a threat.

When designing a new aircraft, shaping of the external geometry would therefore be the primary technique to reduce RCS. The main guidelines for shaping an aircraft for low RCS can be summarised as follows [1, p.1518], [4, pp.292-4]:

1. A planform shape with a minimum of specular returns should be chosen; surface and edge returns should be placed well away from threat sectors.
2. Use long swept lines for narrow beamwidth spikes, and sloped, shallow surfaces viewed at shallow angles to reflect energy well away from receiver (figure 1.3).
3. Leading edges should be swept, and planform body lines should not be viewed perpendicularly in the threat sector.
4. Rounded leading edges are sources of specular reflection and should be avoided.
5. Unavoidable body lines should be aligned to place their specular spikes into a common direction

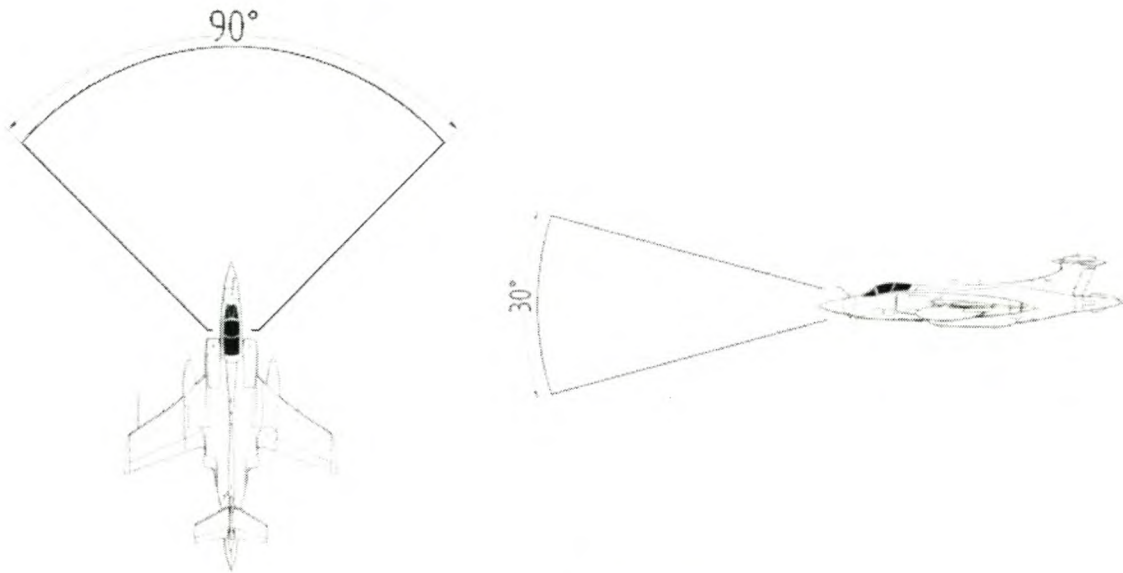


Figure 1.2: Threat sectors

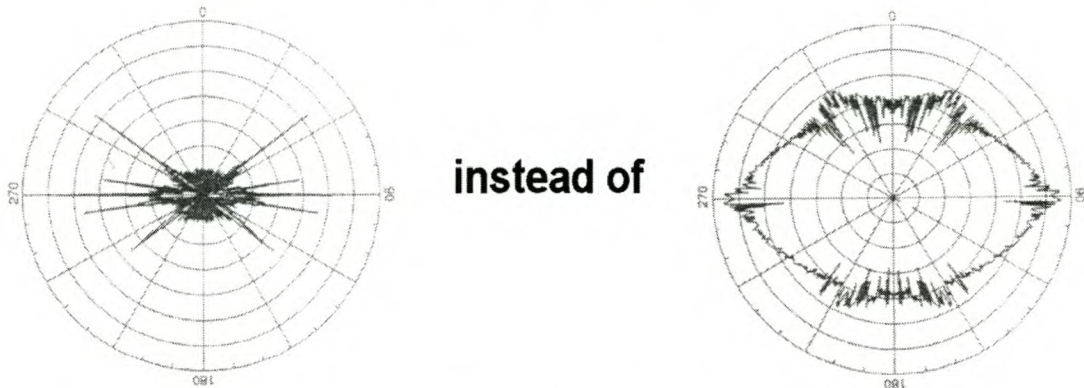


Figure 1.3: RCS polar of stealth aircraft versus “normal” aircraft [4]

6. Minimise or eliminate surface discontinuities, by using smooth, blended surfaces, antennas and sensors; minimise surface roughness.

Engines and air inlets are large contributors to the overall RCS of an aircraft [1, p.1518], [2, pp.1356-7]. This contribution has to be minimised on a stealth aircraft. Whilst conforming to the guidelines already mentioned, the following guidelines apply to inlets and engines specifically:

7. Blend inlets and exhausts into the fuselage.
8. Engines should be buried in the airframe, with inlets and exhausts preferably located on the upper portion of the airframe, to be shielded from ground-based radar.
9. S-shaped inlet ducts, or screens over the inlets, should be used to shield the engine compressor face from incident radar energy.

Incorporation of these guidelines normally leads to geometries that reduce the aerodynamic performance of an inlet, as mentioned in section 1.1. For instance, aligning the inlet lips with the main edge directions usually leads to inlet sweep and rake angles larger than those on non-stealthy aircraft. This is shown in figure 1.4, along with examples of consequences of the shaping rules.

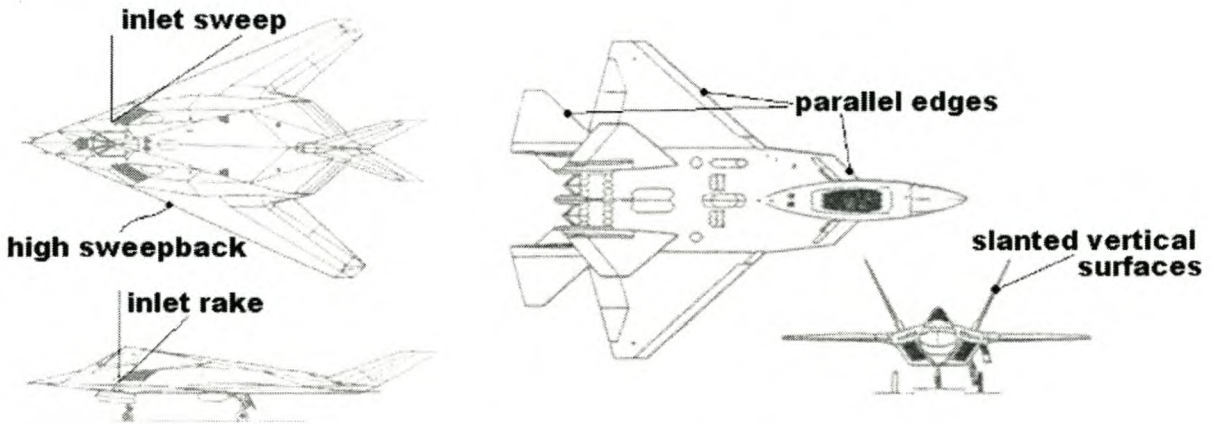


Figure 1.4: Consequences of shaping rules

1.3 Inlet aerodynamic considerations

The main goals of an air inlet is to ensure [5, Chapter 2]:

1. that the engine is properly supplied with air under all conditions of aircraft operation and
2. that the functioning of the airframe is not excessively impaired in the process.

Any inlet can be described in terms of a general aerodynamic duct, illustrated in figure 1.5, where the subscript ∞ refers to conditions in the free stream, c to the inlet capture plane and f to the engine face plane. The engine occupies the space between stations f and e .

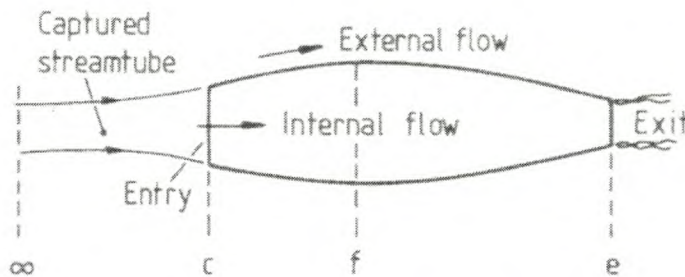


Figure 1.5: The aerodynamic duct [5, Chapter 2]

Because the engine requires air at moderately subsonic speeds (generally much lower than the aircraft flying speed), the duct leading from the to the engine face should act as a diffuser.

Any loss of total pressure in the duct lowers the effective thrust of the engine. Velocity and total pressure profiles at the engine face should be as uniform as possible; a large variation can lead to compressor stalling [6].

The efficiency of the diffusion process in the duct is measured by the ratio of total pressures at the engine face and the free stream, and is termed the *pressure recovery* of the inlet:

$$\eta = \frac{P_f}{P_\infty} \quad (1.1)$$

It is, however, sometimes convenient to describe the inlet performance in terms of the parameter $C_{\Delta P}$, defined as

$$C_{\Delta P} = \frac{\Delta P}{q_c} \quad (1.2)$$

where $\Delta P = P_\infty - P_f$ and q_c is the dynamic pressure at the inlet capture plane. If one assumes that no flow separation occurs on the approach to the inlet, or in the duct itself, then the loss in total pressure is due only to friction. This leads to the following approximate theory of friction loss [5, Chapter 2]:

$$C_{\Delta P} = IC_{Fd} + JC_{Fa} \cdot \mu^3 \quad (1.3)$$

In this expression C_{Fd} and C_{Fa} are the friction coefficients in the duct and on the approach, respectively. I is the *duct integral*, which is only a function of the duct geometry (φ is the local duct perimeter):

$$I = \int_{\ell_c}^{\ell_f} \left(\frac{A_c}{A} \right)^2 \frac{\varphi}{A} d\ell \quad (1.4)$$

J is the *corrected position ratio*, defined as

$$J = k \frac{S}{A_c} \quad (1.5)$$

where k is an empirical constant close to unity (reference [5] states that $k = 0.8$ is a good approximation for many practical cases), and S is the wetted area of the fuselage ahead of the inlet. μ is the ratio of the inlet capture area to the free stream area of the captured streamtube:

$$\mu = \frac{A_c}{A_\infty} \quad (1.6)$$

A_∞ can be determined if the engine mass flow requirements are known (see section A.7).

For $\mu > 1$ the free stream area is smaller than the capture area, and the flow decelerates ahead of the inlet. This leads to some *external diffusion*, which is 100% efficient when there is no interaction with the fuselage boundary layer. In an inlet which projects directly into the free stream, this reduces the amount of internal diffusion that is necessary. In turn, this alleviates the problem of turbulent mixing associated with flow separation in areas of adverse pressure

gradients inside the inlet duct, which is a major source of pressure loss in inlet aerodynamics. To minimise drag, however, a restriction is imposed on the size of the entry that can be used. This represents a major compromise in inlet design, namely between pressure recovery and drag [5, Chapters 1 and 2].

For subsonic inlets, rounded lips are preferable to sharp-edged lips. A rounded inlet lip provides a continuous area for the stagnation streamline to attach, as well as as a smooth path for the flow to accelerate into (or around) the nacelle. This is illustrated in figure 1.6.

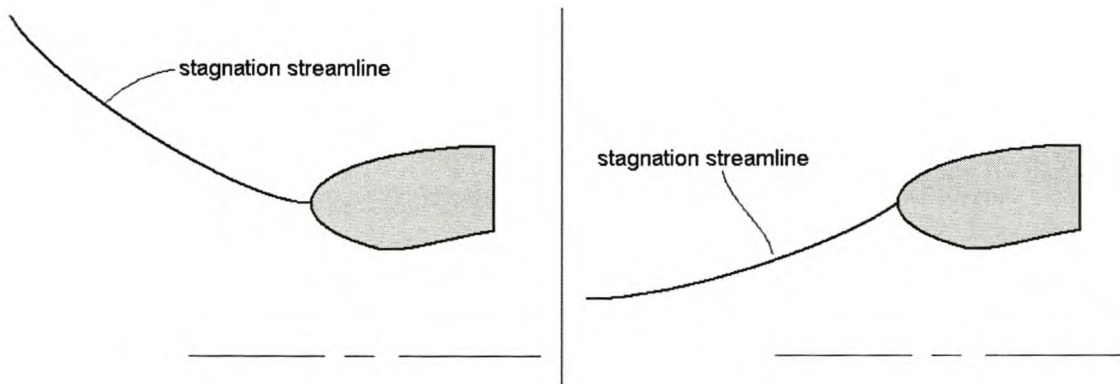


Figure 1.6: Blunt-lipped inlet, $\mu < 1$ (left), $\mu > 1$ (right)

Sharp edges are preferred from a stealth point of view (as mentioned in section 1.2) but only provide a single point for the stagnation streamline to attach (see figure 1.7). Because there is no smooth path for the flow to accelerate, separation at the inlet lip is very probable. In the case where $\mu < 1$, this separation zone is located inside the inlet, which would decrease the pressure recovery of the duct. If the separation zone is located on the outside of the duct, this adds to the drag of the aircraft. The same situation is generally caused by flow spillage, where air that initially enters the inlet actually flows out again.

Several other factors influence the pressure recovery of an inlet, including:

- Sweep and rake angles of the inlet.
- Flow separation ahead of the inlet, due to an adverse pressure gradient accompanying pre-entry retardation.
- Interaction with the fuselage boundary layer for overbody inlets. This can lead to increased pre-entry retardation, and aggravated separation ahead of the inlet [5].

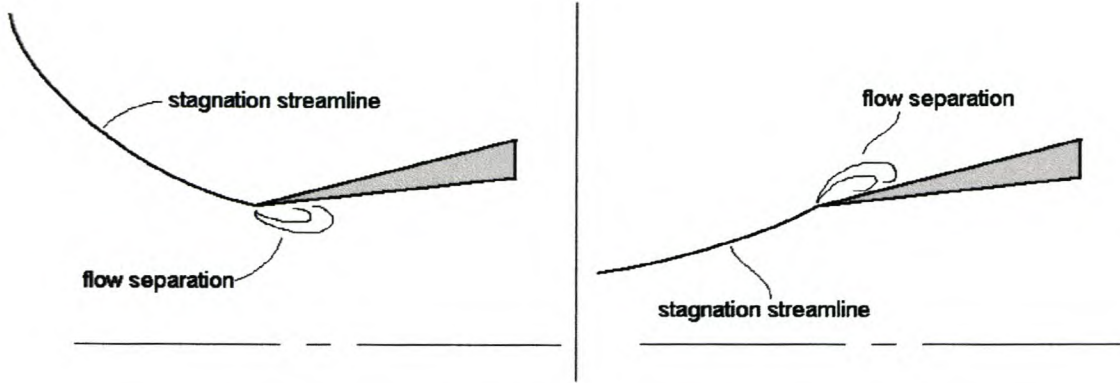


Figure 1.7: Sharp-lipped inlet, $\mu < 1$ (left), $\mu > 1$ (right)

1.4 Current developments

Some information has been gathered on UCAV projects currently under development in the USA, namely the Boeing X-45 and the Northrop Grumman X-47. Qualitative information on their inlets are presented.

1.4.1 Boeing X-45

This aircraft first flew in May 2002, and the primary role envisioned is suppression of enemy air defences ahead of the manned air combat force. The design has no vertical control surfaces and relies heavily on the shaping factors described in the previous section (see figure 1.8). Maximum speed is projected to be in the order of Mach 0.9 [7].

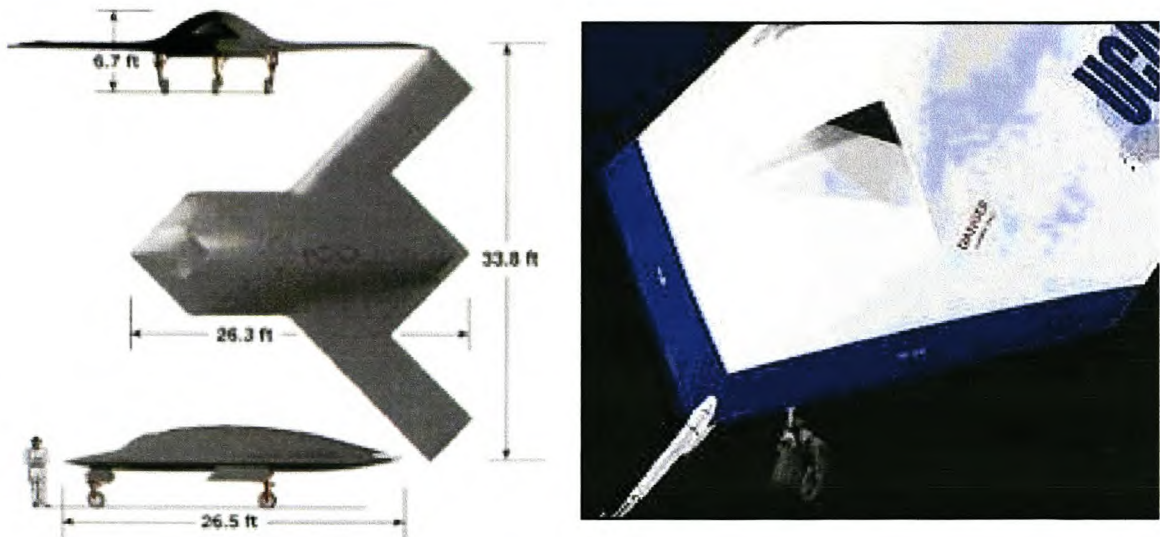


Figure 1.8: Boeing X-45, three view and inlet detail [7]

The inlet feeding the single turbofan seems to be a hybrid between two types of inlets, namely a scoop type (where the inlet projects into the airflow and leads the air to the engine through a curving duct; i.e. the inlet and engine are not co-linear) and a flush type (an inlet which does not project into the oncoming airflow). The inlets sidewalls are aligned parallel to the main sweepback angles. It seems reasonable to assume that the engine is buried deep in the airframe and fed through an S-shaped duct.

1.4.2 Northrop Grumman X-47

The X-47 is a multi-role UCAV being designed for the US Navy. It has a “kite-shaped” profile (which is inherently stealthy) with high leading edge sweepback and a forward-swept trailing edge (see figure 1.9).

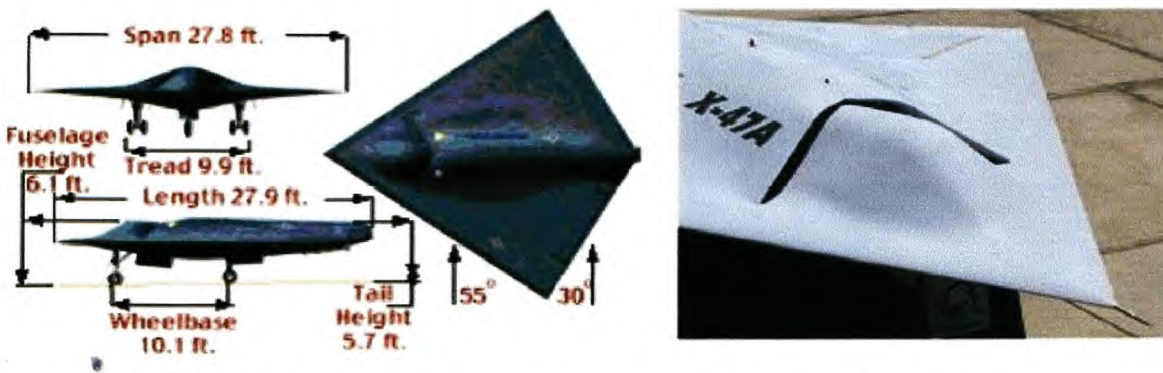


Figure 1.9: Northrop Grumman X-47, three view and inlet detail [7]

The bump-type inlet is one of the stealthiest inlets ever designed, according to Northrop Grumman. The bump shields the inlet lips from incident radar when viewed from an angle, and may serve to channel air into the inlet [8].

1.5 Thesis objectives

The main objective of this thesis is to investigate the aerodynamic properties of a mission-adaptive air inlet for a stealthy UCAV, using commercial Computational Fluid Dynamics (CFD) software. Since the particular CFD package (CFX 5.5, see Appendix B) has not been used in the department for this purpose before, the first major objective was to validate the software against similar flow scenarios with known solutions.

A first-order design for a generic stealthy inlet was developed, which formed the starting point to complete the subsequent milestones:

- CAD modelling of the inlet geometry, and transferring of the model to CFD software.

- Proper definition of the computational space and mathematical models in order to generate a model that is physically viable.
- Identification and extraction of the relevant variables that is needed to characterise the performance of the inlet.
- Synthesis and interpretation of the numerical results in order to comment on the aerodynamic viability of the design, and make to suggestions for improving the performance of the inlet.

1.6 First-order design of inlet

A typical external configuration for a stealthy UCAV was obtained from a company that develops UAVs (see Appendix A). This configuration, which called for a top-mountd inlet, was used as the base geometry for this thesis. The mission-adaptive criterion was satisfied by a variable-geometry bump in front of the inlet, to shield the inlet lips from incident radar energy. In low-threat situations, the bump would be lowered in order to interfere as little as possible with the flow into the inlet (figure 1.10) while it would be raised during high-threat stages of the aircraft's mission (figure 1.11).

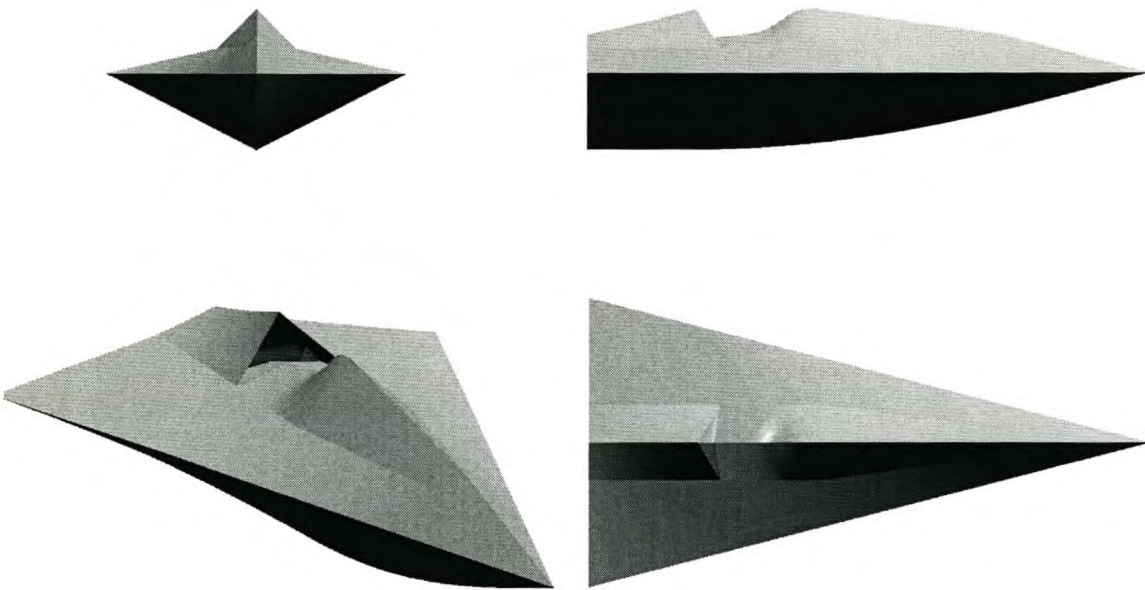


Figure 1.10: External inlet design, bump-down configuration

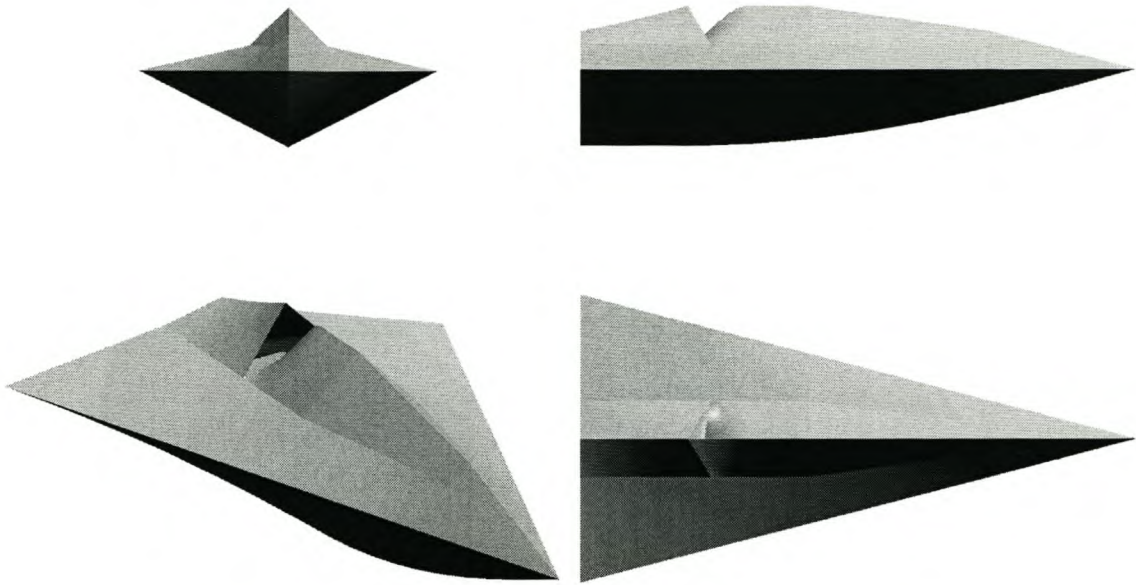


Figure 1.11: External inlet design, bump-up configuration

The duct leading from the external inlet to the engine is shown in figure 1.12. The S-shape is due to the fact that the engine is buried inside the airframe to hide the compressor face, while the change in cross section from roughly triangular to rectangular to circular is to assist in preventing radar energy that may still enter the duct from radiating back out again.

The design process for the inlet is explained in Appendix A.



Figure 1.12: Inlet duct internal shape

1.7 Thesis overview

The main body of the thesis is presented in the next four chapters, the broad outlines of which are as follows:

Chapter 2

Validation of the CFD package, by comparing numerical results for external flow scenarios with analytical solutions or experimental results.

Chapter 3

Validation of the CFD package, by comparing numerical results for internal flow scenarios with analytical solutions or experimental results.

Chapter 4

The first-order inlet design was subjected to a series of preliminary CFD simulations to determine the gross flow characteristics. Focus was on streamline profiles into the inlet, as well as velocity and total pressure profiles at the engine compressor face. The design was modified and this second-order design then constitutes the subject of all further investigations.

Chapter 5

Integration of all preliminary work into the CFD modelling of the second-order design. All details of the CFD models are discussed. An overview of the simulations that were run is given and the post-processing of the raw results is briefly discussed. The processed results are analysed in detail to determine the aerodynamic performance of the inlet. From this analysis, conclusions are drawn and recommendations made for further improvement on the design.

Conclusions and recommendations are presented in the final chapter.

Chapter 2

Validation of CFD package: external flow

2.1 Objectives

Before any CFD code is used in a design or analysis situation, the user has to be sure that it will produce results that are correct to within acceptable error tolerances. This validation is usually done by simulating scenarios for which known analytical or experimental results exist, and comparing the numerical and existing results. Only after a satisfactory correlation has been achieved can the code be trusted to give accurate results for similar problems.

The purpose of this chapter is to show that CFX 5.5 does indeed produce realistic results for the external flow around an object. Three cases were investigated, namely turbulent flow over a flat plate (section 2.2.1), axi-symmetric Rankine halfbody (section 2.2.2) and a sphere (section 2.2.3). Validation cases for laminar flow were not considered, because the operating conditions of the UCAV (as explained in Appendix A) ensures that the flow over it would be turbulent. These operating conditions also suggest that the fluid can be modelled as an ideal gas, and this was used for all subsequent simulations.

It was decided to use two-equation turbulence models in all the validation cases, since these offer good predictions of the characteristics and physics of most flows of industrial relevance. The $k - \varepsilon$ and Shear Stress Transport (SST) models were chosen because the first is the industry standard two-equation model, and the second is recommended for flows in adverse pressure gradients [18, Turbulence and Near-Wall Modelling]. Details of these models are discussed in sections B.4.1 and B.4.2, respectively.

For each of the validation cases, the boundary conditions that were applied are tabulated. The different types of boundary condition are treated in detail in section B.5.

In this and subsequent chapters, the error of the numerical results relative to the known results are sometimes mentioned. Unless stated otherwise, this error is computed as follows:

$$error_{\phi}(\%) = \left(\frac{\phi_{num} - \phi_{known}}{\phi_{known}} \right) \times 100 \quad (2.1)$$

where ϕ refers to the variable for which the error is computed.

The details of the numerical solution (total number of elements, number of iterations, size of false time steps, etc.) for each validation case are listed in Appendix C.

2.2 Validation results

2.2.1 Flat Plate

The flat plate represents a flow situation with zero pressure gradient. A theoretical expression for the skin friction coefficient C_f on a smooth flat plate in turbulent flow is given by

$$C_f = \frac{0.455}{\ln^2(0.06Re_x)} \quad (2.2)$$

White [9, Chapter 6] states that this expression is recommended as a more or less “exact” relation for flat plate turbulent skin friction.

To derive a theoretical expression for C_f the velocity profile in the boundary layer must be specified. The derivation of equation 2.2 employs Spalding’s Law of the Wall, which has been verified experimentally. Equation 2.2 is only valid for turbulent flow, while the real flow is of course initially laminar, with transition to turbulence occurring between approximately $2.5 \times 10^6 \leq Re_x \leq 4.8 \times 10^6$ [9, Chapter 5]. The turbulence models enforce turbulent flow from the leading edge, however, neglecting the initial laminar flow and transition region [10]. This is analogous to having a trip wire on the leading edge in an experimental investigation of the flow.

Simulations were done on both structured and unstructured volume meshes (see Appendix B for a discussion on meshing in CFX 5.5). The computational domain was identical for both cases and is shown in figure 2.1 (dimensions shown are in meters). The length of the plate was 2 m, with the leading edge 0.25 m downstream from the inflow boundary. It was centered in the direction normal to the flow. The boundary conditions are listed in table 2.1.

The meshes were refined until a satisfactory correlation with equation 2.2 were achieved, under the assumption that further mesh refinement would result in a correlation which was at least as good as is presented in this section. Figures 2.3 and 2.5 shows C_f versus Re_x for the structured and unstructured meshes, respectively. The numerical results were obtained by

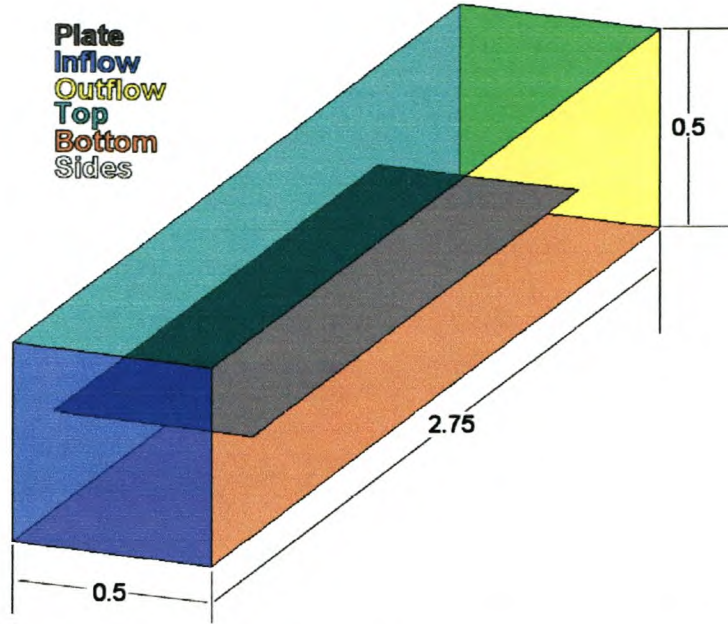


Figure 2.1: Computational domain for flat plate problem (dimensions in [m])

Boundary Name	Boundary type	Value
Plate	Wall	No slip
Inflow	Inlet (Normal speed in)	90 [m/s]
Outflow	Outlet (Relative static pressure)	0 [Pa]
Top	Opening (Relative static pressure)	0 [Pa]
Bottom	Opening (Relative static pressure)	0 [Pa]
Sides	Symmetry	

Table 2.1: Boundary conditions for flat plate problem

calculating the average C_f across the width of the plate, at a number of stations along the length. Graph legends in these two figures are in the form of (*advection scheme, turbulence model*), and is explained in table 2.2.

Symbol	Meaning
1st	UDS (first-order) advection
2nd	Full second-order advection
2ndhr	second-order high resolution advection
$k - \varepsilon$	$k - \varepsilon$ turbulence model
SST	Shear Stress Transport turbulence model

Table 2.2: Graph legend explanation

Detailed descriptions of the different turbulence models and advection schemes are given in Sections B.4 and B.6.

Structured mesh results

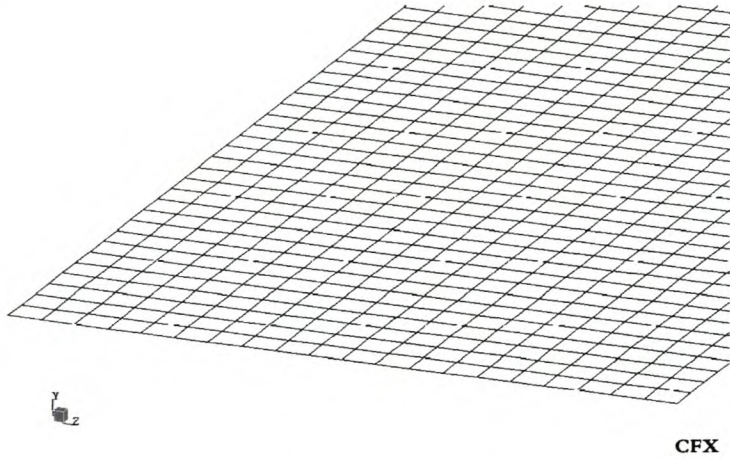


Figure 2.2: Flat plate: structured surface mesh

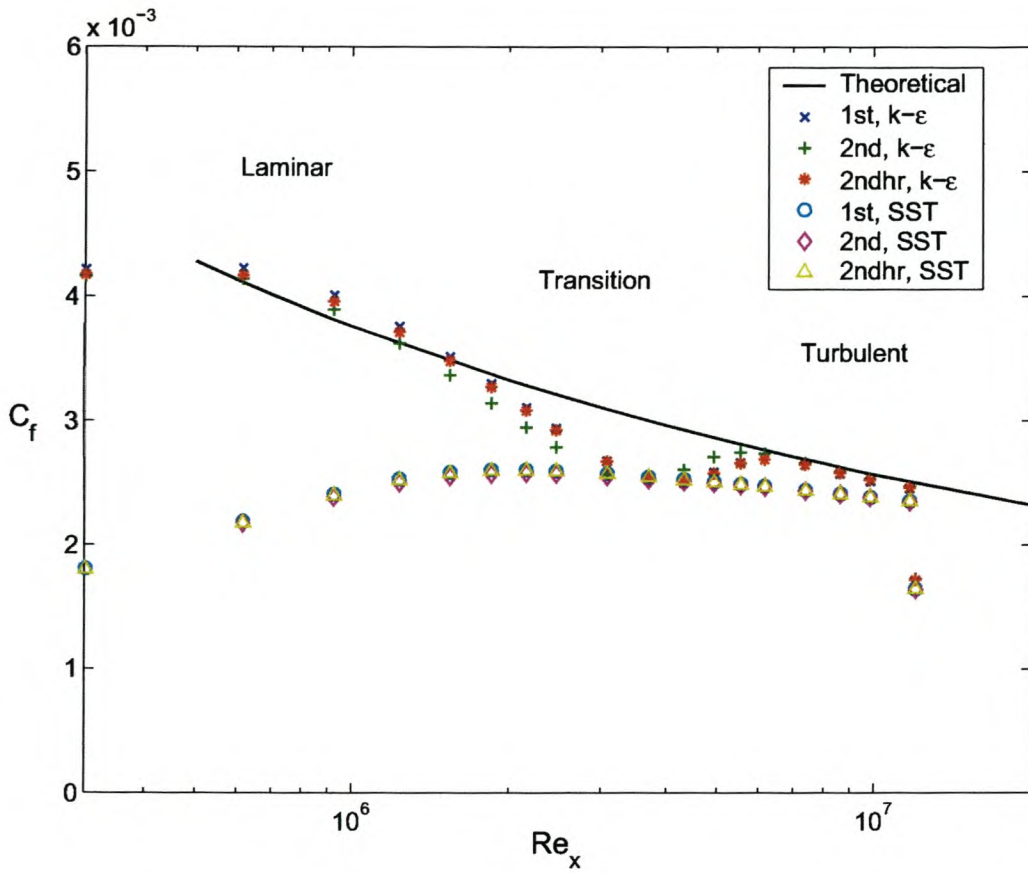


Figure 2.3: Turbulent flat plate flow: structured grid results

The structured mesh on the plate is shown in figure 2.2. Each element measures 25×25 mm, while the spacing of the volume mesh normal to the plate was 5 mm for the first 50 mm and

then 10 mm from there on. This equates to an average y^+ value of approximately 1000 which is admittedly very high. Since the CFX 5.5 is not optimised for the generation of structured meshes (see section B.3), further refinement was, however, very difficult. The reader can refer to section C.1.1 for specific details of the numerical simulation.

Looking at figure 2.3, it can be seen that, for a particular turbulence model, there is very little variation between the results from the UDS and the second-order schemes. This is to be expected, since there is very little flow oblique to the grid, and therefore very little numerical diffusion from the UDS scheme (see section B.6). As stated earlier in this section, the transition region spans approximately $2.5 \times 10^6 \leq Re_x \leq 4.8 \times 10^6$, with laminar and turbulent regions at lower and higher values of Re_x , respectively.

The $k - \varepsilon$ results are in good agreement with equation 2.2 in the fully-turbulent region of flow, with a average error of approximately -2.5%. A “dip” occurs in the results, coinciding with the theoretical range where transition can occur. It may be due to the wall functions not behaving accurately, but this is only speculation. The generally poor results produced by the SST model is probably due to insufficient mesh resolution in the near-wall region (see section B.4.2 for an explanation). It underpredicts the friction coefficient in the fully turbulent region by an average of 9% which might also be attributed to the transport of turbulent shear stress, leading to an underprediction of the shear stress at the wall. This behaviour is discussed thoroughly in section B.4.

All the results show a sudden divergence in the friction coefficient at the trailing edge of the plate ($Re_x \approx 1.2 \times 10^7$). This is most probably a numerical error, caused by the sudden change in boundary conditions, and illustrates that boundary conditions should (if possible) not be applied too close to areas where accurate results are required.

Unstructured mesh results

The unstructured surface mesh for the plate is shown in figure 2.4. The average side length of the elements was 40 mm, while the leading and trailing edges were refined to 10 mm. The inflation layer (see section B.3) consisted of 10 layers up to a height of 40 mm, with a target y^+ value of 11 (as discussed in section B.3). The average edge length of the tetrahedral volume mesh was also 40 mm. Further details of the numerical simulation can be obtained in section C.1.2.

The results in figure 2.5 seem to be dependent on the advection scheme, rather than on the turbulence model, as was the case for the structured mesh. Also, unlike the the previous results, the numerical results follow the theoretical turbulent flow values even in the theoretically laminar and transition regions. This illustrates the “forced turbulence” mentioned at the start

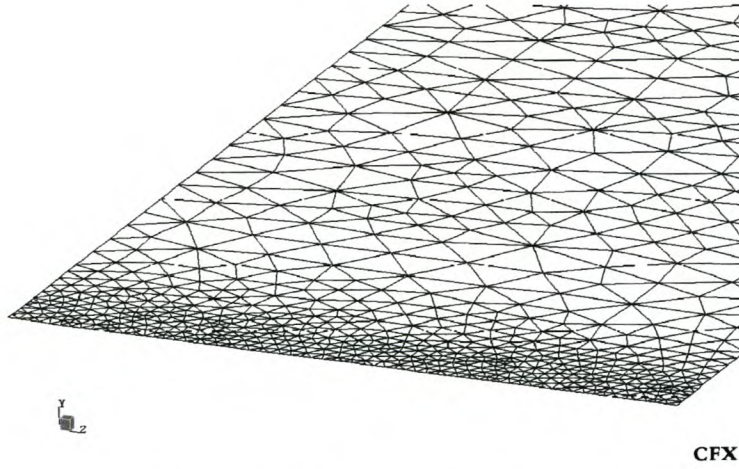


Figure 2.4: Flat plate: unstructured surface mesh

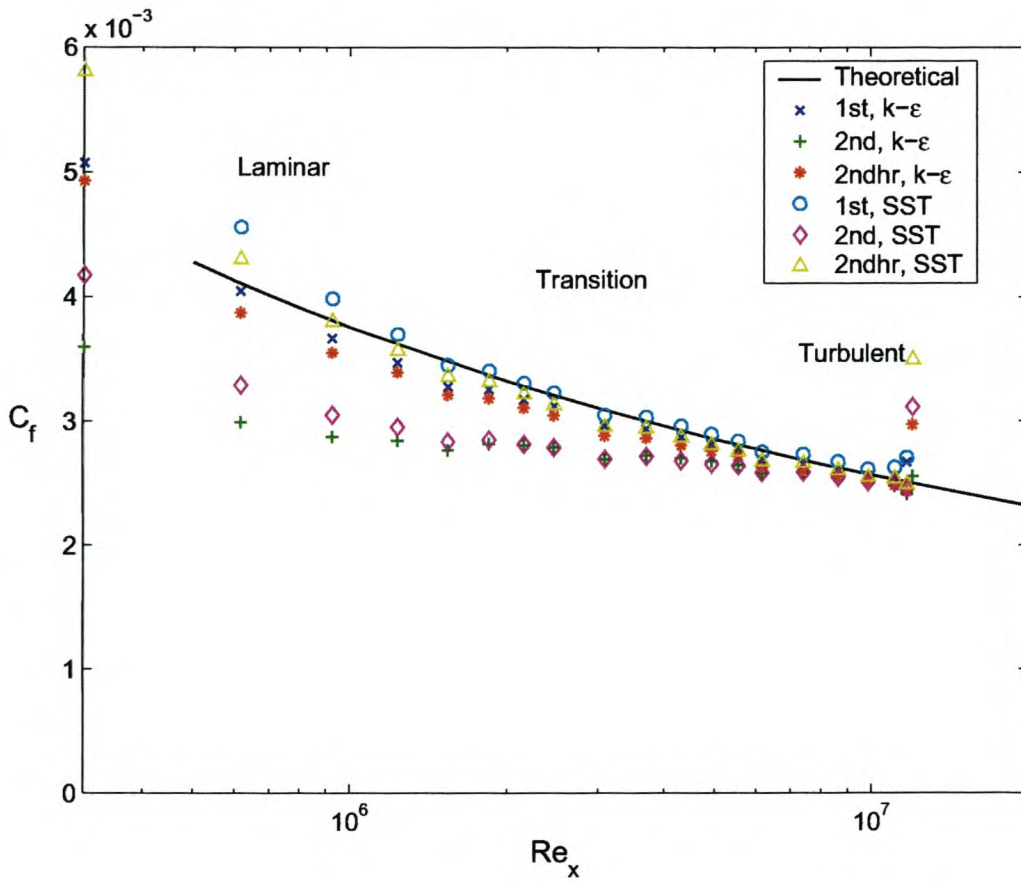


Figure 2.5: Turbulent flat plate flow: unstructured grid results

of this section.

The UDS results are surprisingly accurate, which is probably due to the inflated volume mesh in the boundary layer. This would once again limit the amount of numerical diffusion,

especially for this geometry where the flow is only in one direction. The best correlation is obtained using the High Resolution advection scheme together with the SST turbulence model, with an average error of -1.3% in the fully turbulent region.

Full second-order results underpredict the friction-coefficient by about 4% in the fully turbulent region, for both turbulence models. Seeing that the geometry does not induce high variable gradients, numerical dispersion is probably not the cause. No further explanation is offered, however.

The “dip” in the $k - \varepsilon$ results on the structured mesh is not present on the unstructured mesh. This suggests that the better near-wall resolution of the unstructured mesh significantly improves the performance of both turbulence models.

As on the structured mesh, there is a divergence of the friction coefficient at the trailing edge of the plate, due to the sudden change in boundary condition. The sudden increase in this case is best explained by considering figure 2.6, which shows the computed velocity in the trailing edge region, superimposed on part of the volume mesh:

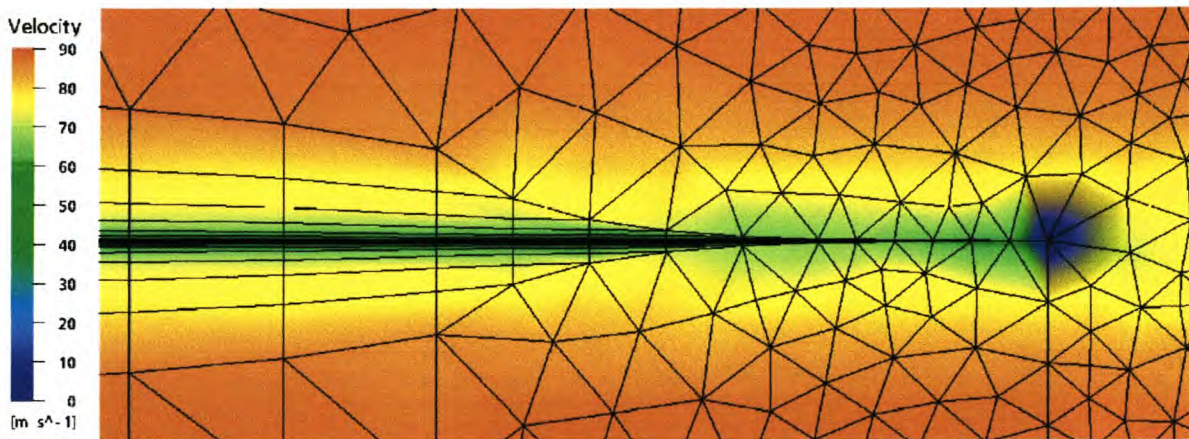


Figure 2.6: Flat plate trailing edge region: Volume mesh and velocity contour

The inflated mesh is clearly visible, and it can be seen that the number of layers decrease as the trailing edge is approached. Right at the edge there is no inflation layer, and the wall boundary condition is applied at the centroid of each surrounding volume mesh element, which is clearly visible when the velocity contour in the immediate vicinity of the trailing edge is considered. This causes an overprediction of the velocity gradient (and hence the friction factor) right at the trailing edge.

In general, the results presented in this section confirm the reliability of the code for fully turbulent external flow with no pressure gradient.

2.2.2 Axi-symmetric Rankine halfbody

The Rankine halfbody is defined in potential flow by the superposition of a point source in a uniform stream. The stagnation streamline forms the boundary of the body, as illustrated in figure 2.7. Note that this figure actually shows a two-dimensional Rankine halfbody, for which the dividing streamline has a slightly different shape than the axi-symmetric version.

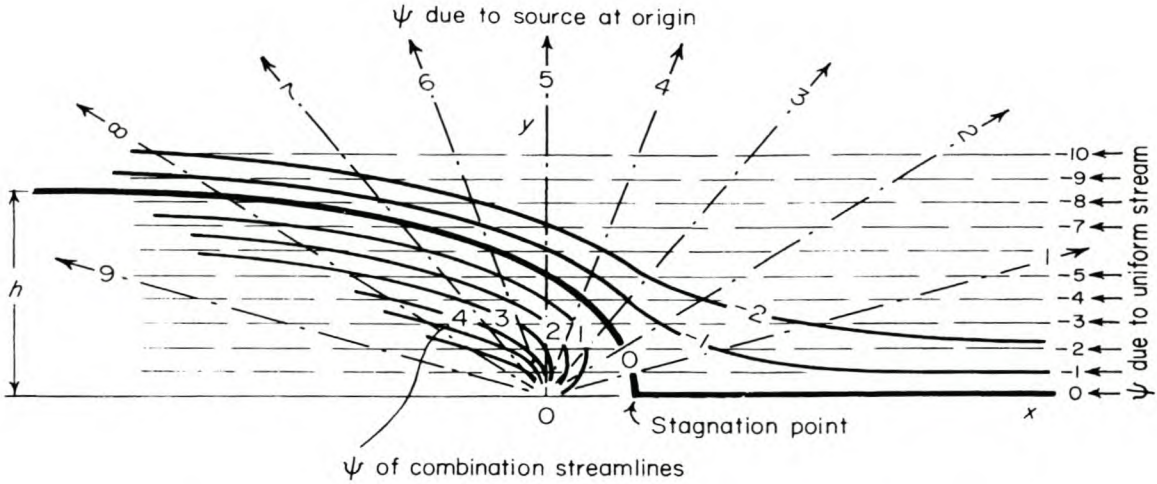


Figure 2.7: Rankine halfbody definition [11, Chapter 3]

From incompressible potential flow theory, the theoretical pressure distribution on an axi-symmetric Rankine halfbody is given by

$$C_p = 1 - \sin^2 \varphi - \frac{1}{4}(1 + \cos \varphi)^2 \quad (2.3)$$

where C_p is defined as

$$C_p = \frac{p - p_\infty}{\frac{1}{2}\rho V_\infty^2} \quad (2.4)$$

and φ is measured from the symmetry-axis, clockwise around point "0" in figure 2.7.

The Rankine halfbody is a useful validation case to test the performance of the code in accelerating flow, without boundary layer separation. This geometry is also similar in shape to the centerbody of a gas turbine engine. The computational domain is shown in figure 2.8, and the boundary conditions are listed in table 2.3. The maximum diameter (D) of the Rankine halfbody was 0.1 m and its length was 0.3 m. It was centered in the domain, with the rear surface coincident with the outflow plane. The details of the simulation are presented in Appendix C.2.

Having shown that the solver gives realistic results for external flow on structured meshes (figure 2.3), the axi-symmetric Rankine halfbody was simulated on an unstructured mesh

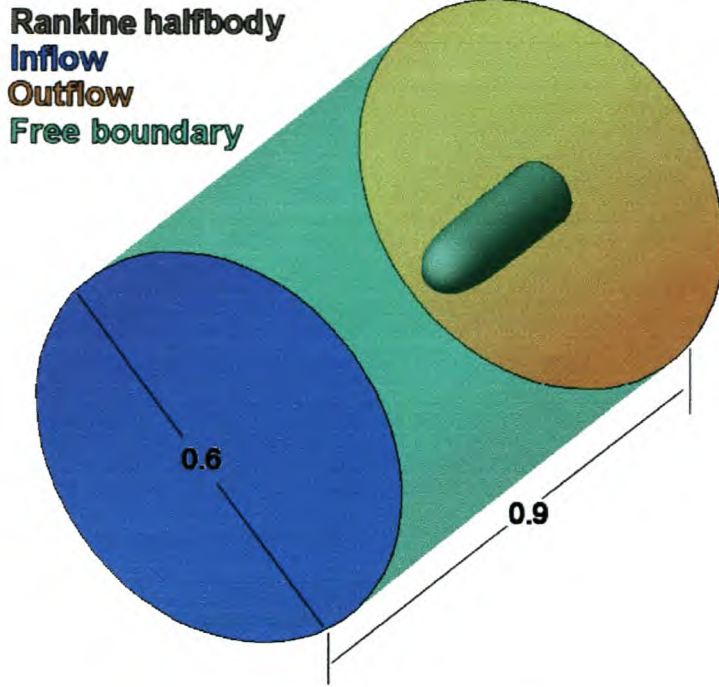


Figure 2.8: Computational domain for axi-symmetric Rankine halfbody (dimensions in [m])

Boundary Name	Boundary type	Value
Rankine halfbody	Wall	No slip
Inflow	Inlet (Normal speed in)	90 [m/s]
Outflow	Outlet (Relative static pressure)	0 [Pa]
Free boundary	Opening (Relative static pressure)	0 [Pa]

Table 2.3: Boundary conditions for Rankine halfbody problem

only. The mesh was again refined until the results agreed satisfactorily with equation 2.3. The final surface mesh on the body itself is shown in figure 2.9. The average edge length of the triangular elements is 15 mm, while the highly curved region near the nose is meshed with an average edge length of 5 mm. The inflation layer consists of 10 layers, varying in height between 5 and 15 mm, while the average edge length of the volume mesh is 20 mm.

Figure 2.10 shows the comparison between the theoretical and numerically computed pressure coefficients, with the shape of the body superimposed for clarity. These were calculated by calculating the average C_p around the body at a number of streamwise locations.

As with the flat plate simulation on the unstructured grid, the advection scheme that was used proved to be the deciding factor in the accuracy of the results. For both turbulence models, the UDS scheme underpredicts the acceleration around the nose of the body ($0 \leq x/D \leq 0.7$), and hence the associated values for C_p are too high. All second-order simulations returned very



Figure 2.9: Rankine halfbody: surface mesh

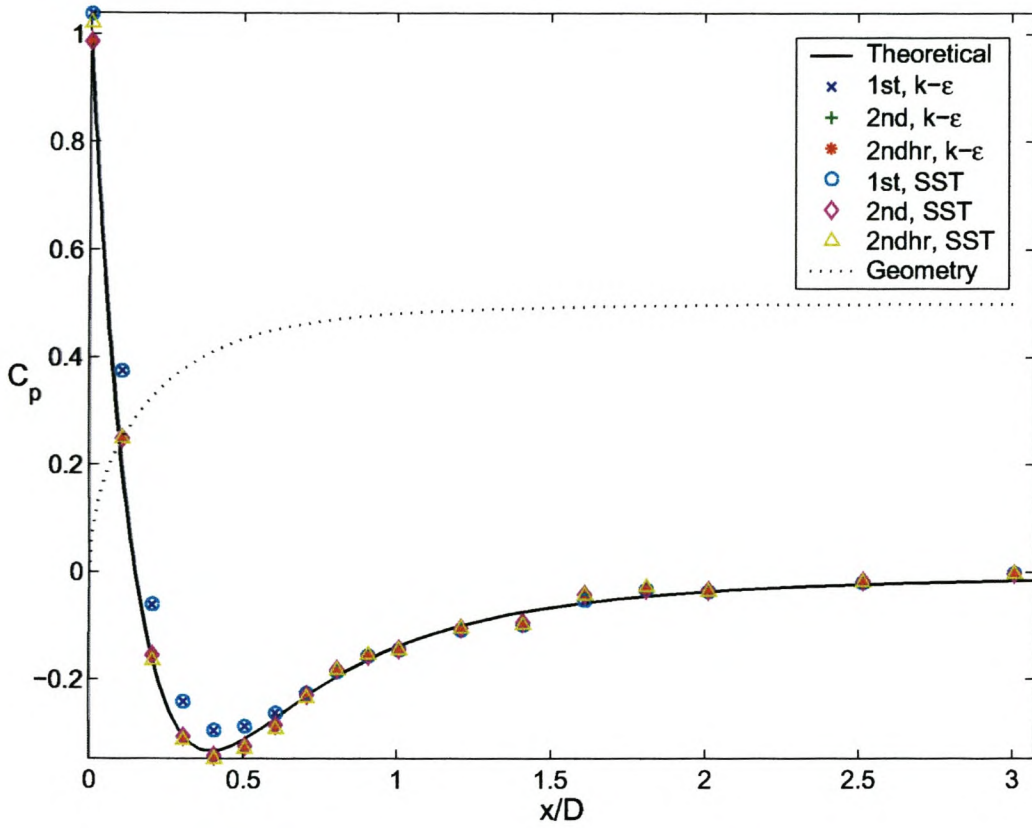


Figure 2.10: Rankine halfbody pressure distribution

good results, with only a slight oscillation around the theoretical results between $0.4 \leq x/D \leq 2$.

In incompressible flow, the stagnation pressure coefficient should be unity. For these simulations, however, $M_\infty = 0.26$, which means the flow was subsonic, not incompressible. When an ideal gas is used, CFX 5.5 always treats the density as a variable.

For isentropic compressible flow of a ideal gas, it can be shown that the stagnation pressure coefficient is given by the following equation, which yields a value for $C_{p,0}$ of 1.018 at $M_\infty = 0.26$:

$$C_{p,0} = \frac{\left(1 + \frac{\gamma-1}{2} M_\infty^2\right)^{\frac{\gamma}{\gamma-1}} - 1}{\frac{1}{2} \gamma M_\infty^2} \quad (2.5)$$

The values of $C_{p,0}$, obtained from the different combinations of advection schemes and turbulence models, are given in table 2.4.

Advection scheme, turbulence model	$C_{p,0}$
1st, $k - \varepsilon$	1.039
2nd, $k - \varepsilon$	0.988
2ndhr, $k - \varepsilon$	0.988
1st, SST	1.038
2nd, SST	0.987
2ndhr, SST	1.021

Table 2.4: Rankine halfbody: stagnation pressure coefficients

From figure 2.10 and table 2.4, it can therefore be concluded that the combination of the High Resolution advection scheme and the SST turbulence model delivered the “best” results for this specific validation case.

2.2.3 Sphere

Turbulent flow over a sphere was chosen as validation case because it represents the flow over a three-dimensional body with boundary layer separation. It is also geometrically similar to the back of the bump on the generic UCAV design.

In potential flow, the sphere is defined by the superposition of a point doublet and a uniform stream, and the pressure distribution is given by

$$C_p = 1 - \frac{9}{4} \sin^2 \varphi \quad (2.6)$$

where C_p is defined again by equation 2.4 and φ is measured from the front stagnation point around the center of the sphere.

Due to the inviscid, irrotational assumption for potential flow, equation 2.6 does not include the effects of boundary layer separation. This is obviously not a representation of the real situation. The main purpose of this validation case was therefore to establish how accurately CFX 5.5 can predict boundary layer separation in external flow. Some sources report that the turbulent boundary layer on a sphere separates at about $\varphi = 120^\circ$ [12, Chapter 7], while the experimental results reproduced in figure 2.13 show separation at about $\varphi = 140^\circ$ [13, Chapter 9].

The computational domain is shown in figure 2.11 and the boundary conditions are listed in table 2.5. The diameter of the sphere was 0.4 m, and it was positioned exactly in the center of the computational domain. Refer to section C.3 for the details of the simulation.

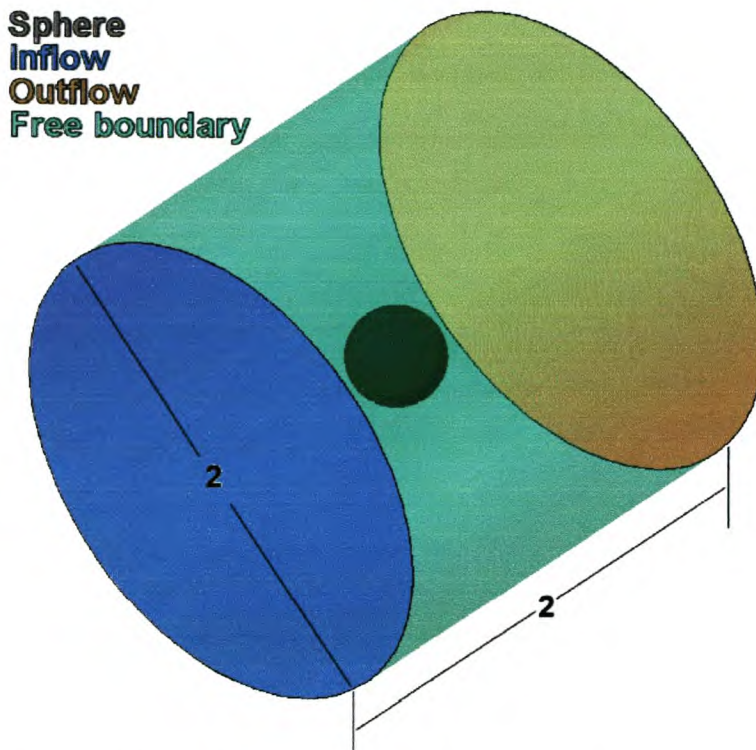


Figure 2.11: Computational domain for sphere (dimensions in [m])

Boundary Name	Boundary type	Value
Sphere	Wall	No slip
Inflow	Inlet (Normal speed in)	70 [m/s]
Outflow	Outlet (Relative static pressure)	0 [Pa]
Free boundary	Opening (Relative static pressure)	0 [Pa]

Table 2.5: Boundary conditions for sphere problem

As for the Rankine halfbody, a number of progressively refined unstructured grids were gen-

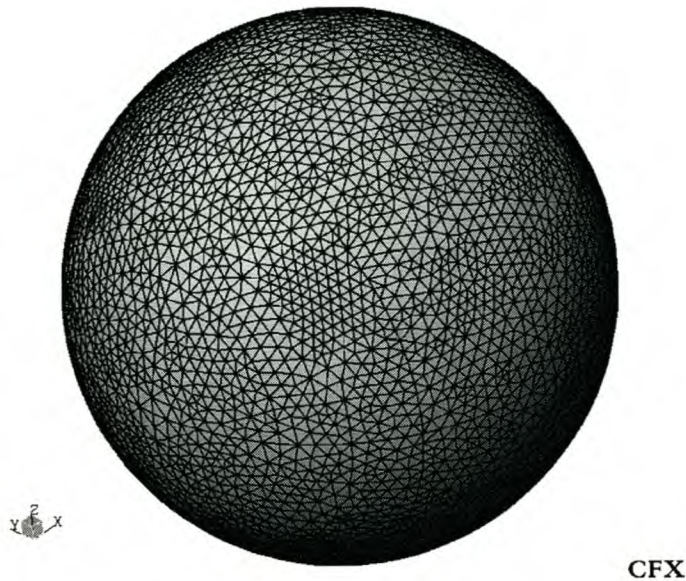


Figure 2.12: Sphere: surface mesh

crated, on which the flow was simulated until a satisfactory correlation with the experimental results were obtained. The final surface mesh on the sphere is shown in figure 2.12. The average edge length of the triangular elements was 10 mm. The inflation layer consisted of 10 layers, up to a height of 10 mm, while the average edge length of the volume mesh was 66 mm.

The comparison between theoretical, experimental and numerically computed pressure coefficients are shown in figure 2.13. The numerical values were obtained by computing the average C_p at constant values of φ around the sphere. It can be seen that, for both turbulence models, the values for C_p obtained using the UDS advection scheme seem to “lag” behind the experimental results by a constant value for φ . This is again due to an underprediction of the acceleration around the curvature of the sphere (see also section 2.2.2). The second-order advection schemes fare much better: both the full second-order and high resolution schemes follow the potential flow solution closely, up to $\varphi \approx 80^\circ$. This is not surprising, since the potential flow equations originate from the Navier-Stokes equations and hence would yield similar results in an accelerating flow. Where the experimental results “cross” the potential flow solution, the numerical results follow the experiments. This would be the influence of the adverse pressure gradient, although the numerically computed pressure gradient seem to be initially more adverse than in experiments, leading to earlier separation ($\varphi \approx 130^\circ$ for the $k - \varepsilon$ model, and $\varphi \approx 126^\circ$ for the SST model). This confirms the increased sensitivity of the SST model to adverse pressure gradients (see section B.4.2). Overall, the combination of second-order high resolution advection and $k - \varepsilon$ turbulence model correlated the best with the experimental results.

For the entrance velocity of 70 m/s, $C_{p,0}$ from equation 2.5 is 1.011. The numerically computed

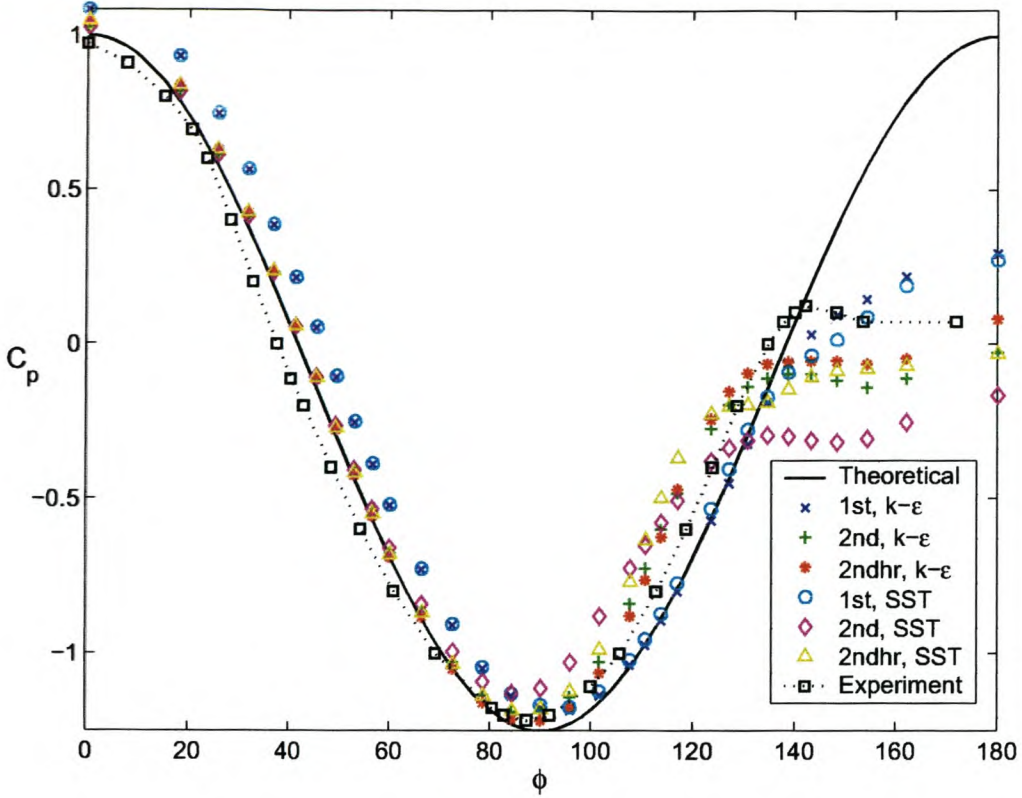


Figure 2.13: Pressure distribution for turbulent flow over a sphere

stagnation pressure coefficients are given in table 2.6, and it can be seen that all these values are too high. The values of C_p are also too high between $0^\circ \leq \varphi \leq 20^\circ$.

Advection scheme, turbulence model	$C_{p,0}$
1st, $k - \varepsilon$	1.083
2nd, $k - \varepsilon$	1.023
2ndhr, $k - \varepsilon$	1.047
1st, SST	1.083
2nd, SST	1.026
2ndhr, SST	1.047

Table 2.6: Sphere: stagnation pressure coefficients

The inaccuracies discussed in the previous paragraph seem to indicate that the mesh in the region near the stagnation point was not fine enough. The main goal for this validation case, namely to determine the reliability of the code in an adverse pressure gradient was achieved, however, since the separation point was predicted between the values given in references [12] and [13].

2.3 Closure

The following conclusions were drawn from the validation cases in this chapter:

1. The code produces realistic results on both structured and unstructured meshes.
2. For flows in zero and favourable pressure gradients, numerical results compare well with theoretical predictions.
3. In a very strong adverse pressure gradient, the numerically computed point of separation is earlier than experiments suggest.
4. There is little difference between the results from the $k - \varepsilon$ and SST turbulence models in zero and favourable pressure gradients, while the SST model displays its increased sensitivity to predict flow separation in adverse pressure gradients, when compared to other two-equation turbulence models.
5. The high resolution advection scheme generally returned the best results. Though UDS results do not generally compare well with the previously known results, they are useful in defining initial conditions for the second order schemes.
6. Regions with high variable gradients should be identified and care should be taken to ensure that the mesh is sufficiently fine in these areas.

Chapter 3

Validation of CFD package: internal flow

3.1 Objectives

For a gas turbine engine, the duct leading from the external part of the inlet to the engine face is one of the most critical components of the inlet system. This is particularly true for the conceptual UCAV presented in section 1.6. The sharp S-bend, combined with drastic section changes and adverse pressure gradient due to the diffusing rear section of the duct (refer again to figure 1.12), suggest that there might be a large loss in total pressure. Flow separation inside the duct is also a possibility and the associated total pressure loss would further reduce the performance of the engine. For the numerical simulation of the UCAV inlet to be useful, it is therefore crucial that the CFD code accurately predicts the pressures inside the duct, as well as the velocity and total pressure profiles at the engine face.

In order to ensure the reliability of the code in these situations, a number of validation cases for internal flow were simulated. Firstly, flow through a circular pipe was solved and compared to the analytical solution (section 3.2.1). Next, focus switched to flows in adverse pressure gradients, and the prediction of boundary layer separation. Numerical results of flow through a two-dimensional diffuser (section 3.2.2) and an S-bend air inlet (section 3.2.3) were compared to experimental results. As for the external flow validation cases, only turbulent flow was considered.

The details of the numerical solution for the validation cases of this chapter are listed in Appendix C.

3.2 Validation results

3.2.1 Circular pipe

Flow through a circular pipe is perhaps the most basic internal flow problem. As for the flat plate in external flow (section 2.2.1), this geometry was first simulated on a structured grid before switching to an unstructured grid.

A useful parameter for comparison is the Darcy friction factor f , defined by ([9, Chapter 6])

$$f = \frac{4 \cdot \tau_w}{\frac{1}{2} \rho U_b^2} \quad (3.1)$$

and related to pipe flow by

$$\frac{\Delta p}{\rho g} = f \frac{L V^2}{d 2g} \quad (3.2)$$

For fully turbulent flow, f is approximated by [12, Chapter 6]

$$\frac{1}{f^{1/2}} = 2.0 \log \left(Re_d f^{1/2} \right) - 0.8 \quad (3.3)$$

The pipe has to be long enough to allow the flow to develop fully. The development length (L_e) for turbulent flow is given by [12, Chapter 6]

$$\frac{L_e}{d} \approx 4.4 Re_d^{1/6} \quad (3.4)$$

The parameters for the pipe flow problem are listed in table 3.1:

Parameter	Value	Comments
L	15 m	
d	0.196 m	
Re_d	472000	
f_{th}	0.0133	Computed from equation 3.3
$L_{e_{th}}/d$	38.8	Computed from equation 3.4

Table 3.1: Pipe flow problem: theoretical parameters

The computational domain is shown in figure 3.1 (the exit plane is not shown in this figure). Boundary conditions are listed in table 3.2. For the simulations on the structured mesh, a 15° wedge was simulated, with symmetry enforced on the radial boundaries. The same problem formulation was initially tried on the unstructured mesh as well, but poor results suggested that the full geometry rather be simulated when this mesh topology is used.

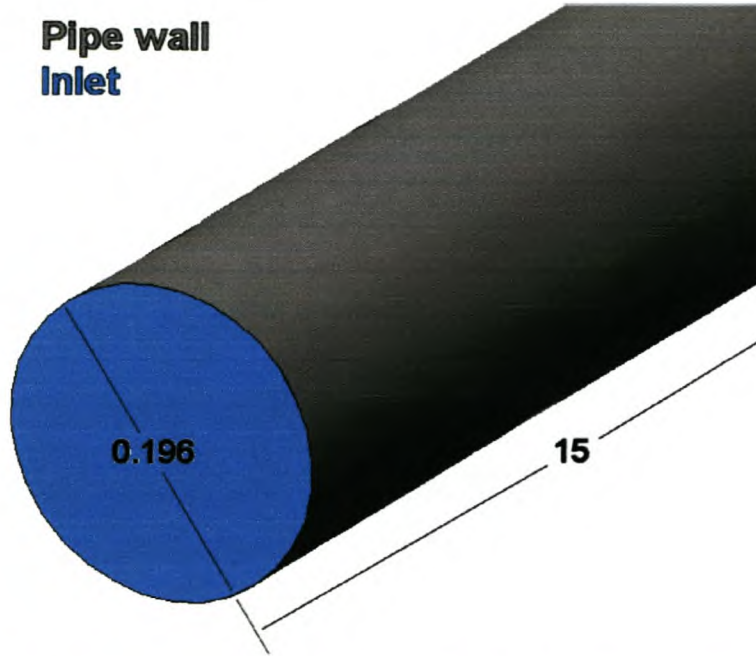


Figure 3.1: Computational domain for pipe flow problem (dimensions in [m])

Boundary Name	Boundary type	Value
Pipe wall	Wall	No slip
Inlet	Inlet (Mass Flow)	1.3 [kg/s]
Exit	Outlet (Relative static pressure)	0 [Pa]

Table 3.2: Boundary conditions for pipe flow problem

For the numerical simulations, the average friction factor around the perimeter of the pipe was calculated at a number of streamwise stations, and compared to the theoretical value. The results presented in this section are the percentage error f_{num} relative to f_{th} .

Structured mesh results

The mesh on the inlet plane and pipe surface is shown in figure 3.2. In the radial direction the mesh consisted of 16 elements up to a radius of 78 mm, with 10 elements in the 20 mm adjacent to the wall. In the axial direction, there were 450 elements. Details of the numerical solution are given in section C.4.1.

Referring to figure 3.3, it can be seen that as for the flat plate results on the structured mesh, the results are dependent on the turbulence model, rather than the advection scheme. The good agreement of the UDS advection scheme with the second-order schemes is once again to be expected since there would be virtually no flow oblique to the grid.

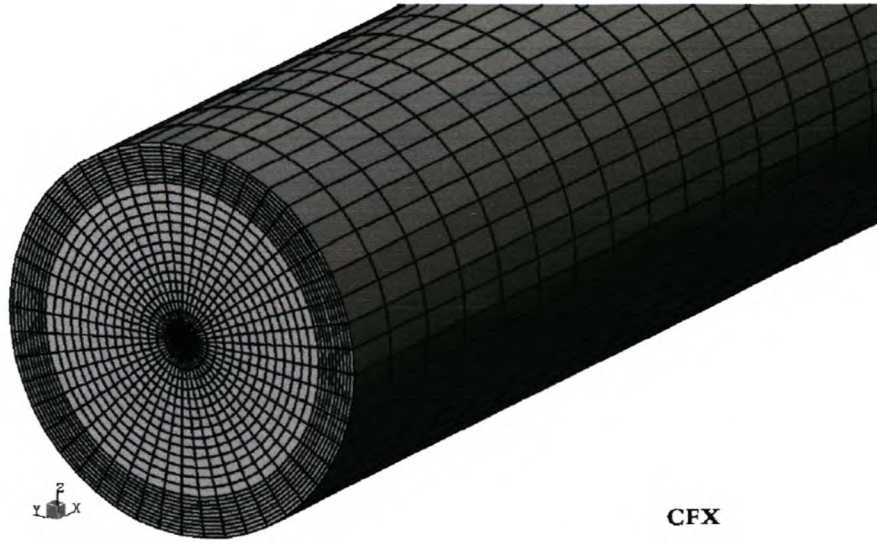


Figure 3.2: Pipe: structured surface mesh

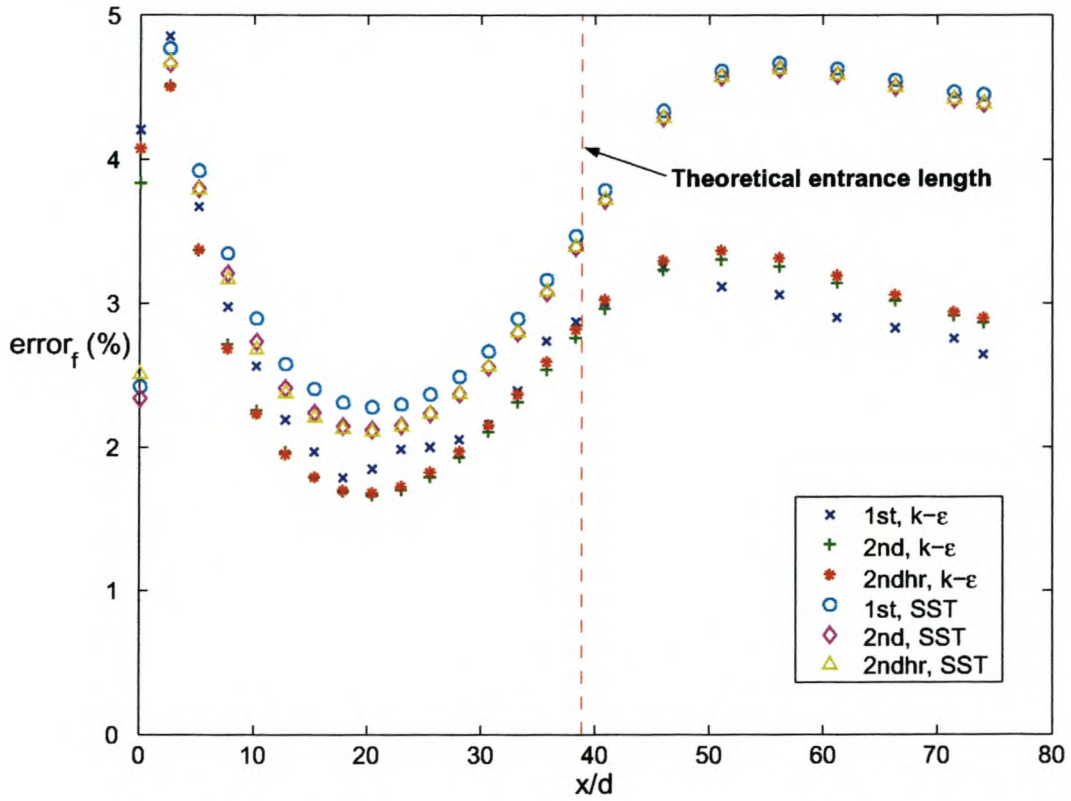


Figure 3.3: Turbulent pipe flow: structured grid results

One surprising result is that the SST turbulence model returns a value for f that is higher than that predicted by the $k - \epsilon$ model. This is contradictory to what is expected from this model (see section B.4.2). One possible explanation is that the boundary layer is not sufficiently resolved for this model to return sufficiently accurate results. In the fully developed region,

the first grid point is located at $y^+ \approx 196$, which lies well into the logarithmic region of the boundary layer [9, Chapter 6].

The error stabilises at $x/d \approx 45$ for the $k - \varepsilon$ model, and at $x/d \approx 50$ for the SST model, suggesting an overprediction of the entrance length.

Despite these problems, the average error in the fully developed region is only 3.1% for the $k - \varepsilon$ model and 4.3% for the SST model. This was deemed accurate enough for validation purposes.

Unstructured mesh results

The unstructured mesh on the inlet plane and pipe wall is shown in figure 3.4. The average edge length of the surface elements, as well as the tetrahedral volume elements were 21 mm. The inflation layer consisted of 10 layers up to a height of 21 mm. The details of the numerical simulation are listed in section C.4.2.

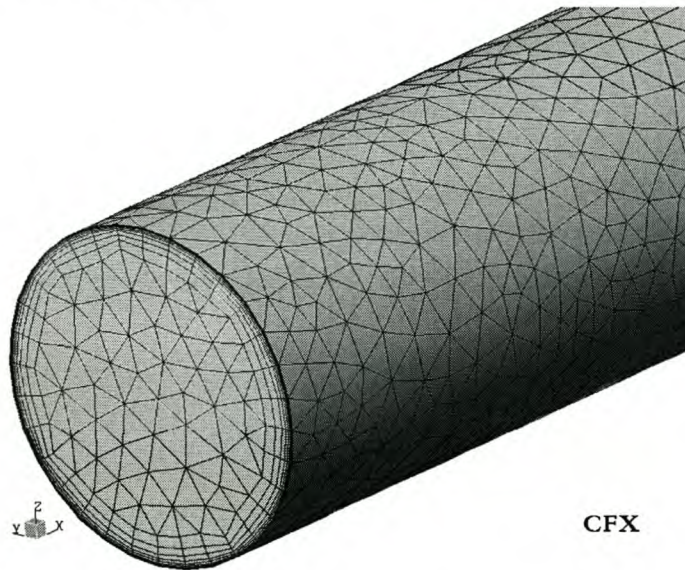


Figure 3.4: Pipe: unstructured surface mesh

The friction factor errors computed on the unstructured mesh are shown in figure 3.5. The decreased accuracy of the UDS advection scheme on the unstructured mesh is readily apparent, due to the control volumes not being aligned with the flow direction. It severely underpredicts the entrance length and overpredicts the friction factors when compared to the second-order results for the respective turbulence models. Both second-order schemes returned average errors within acceptable tolerances. The full second-order scheme, combined with the SST turbulence model returned an average error of 4.0%, while the high resolution scheme in combination with the $k - \varepsilon$ model was 2.6% off target.

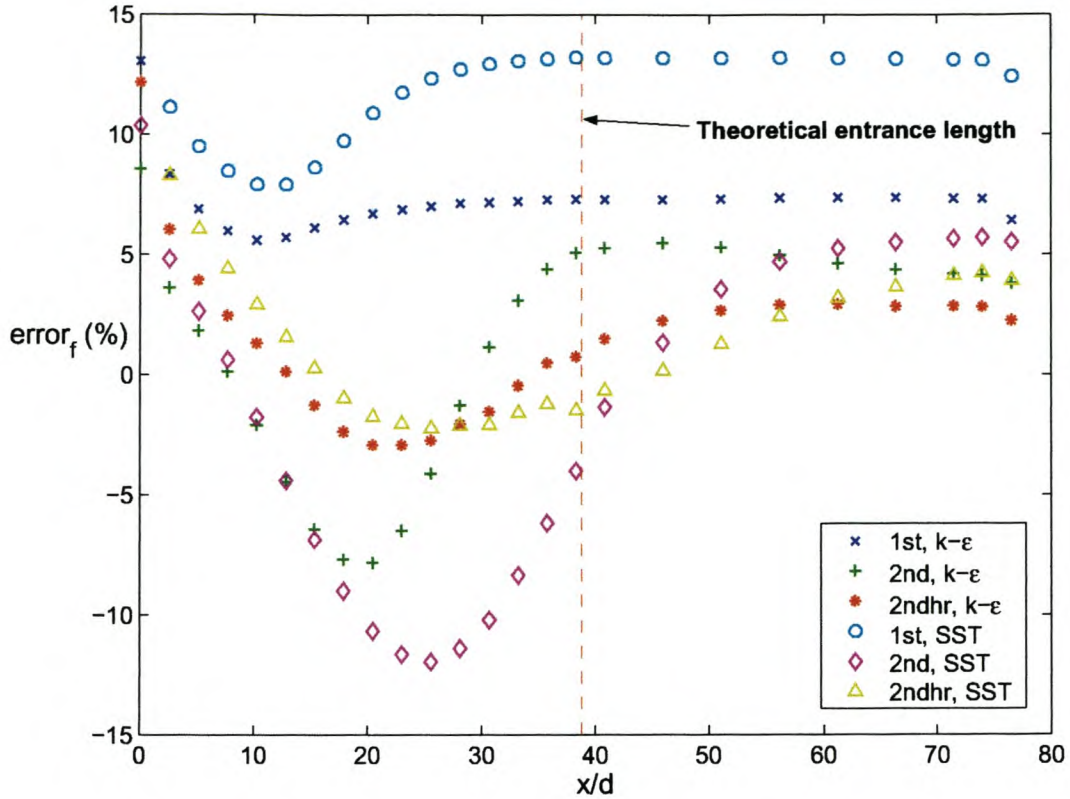


Figure 3.5: Turbulent pipe flow: unstructured grid results

The results for both turbulence models are considered to be within acceptable tolerances for the purpose of validation of the solver.

3.2.2 Two-dimensional diffuser

The asymmetric plane diffuser shown in figure 3.6 was a test case for the 8th Workshop on Refined Turbulence Modelling that was held in in Espoo, Finland, during June 1999 [14].

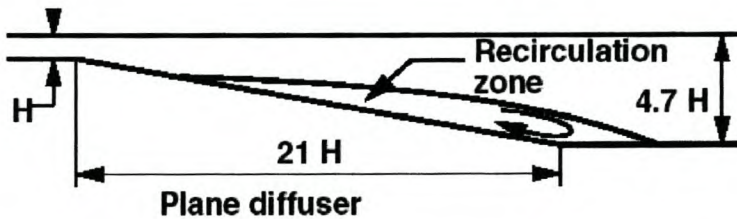


Figure 3.6: Two-dimensional diffuser geometry

The inlet conditions are fully-developed channel flow at $Re_H=20000$, based on centerline velocity at the inlet. Experimental results (including the entrance velocity profile) were obtained from the proceedings of the workshop.

For the purpose of this simulation, the value of H was taken as 0.015 m. The computational domain is illustrated in figure 3.7, and the boundary conditions, as specified for this problem, are given in table 3.3. In light of the previous validation cases, the high-resolution advection scheme was used for all simulations reported on in this section. The details of the numerical simulation are given in section C.5.

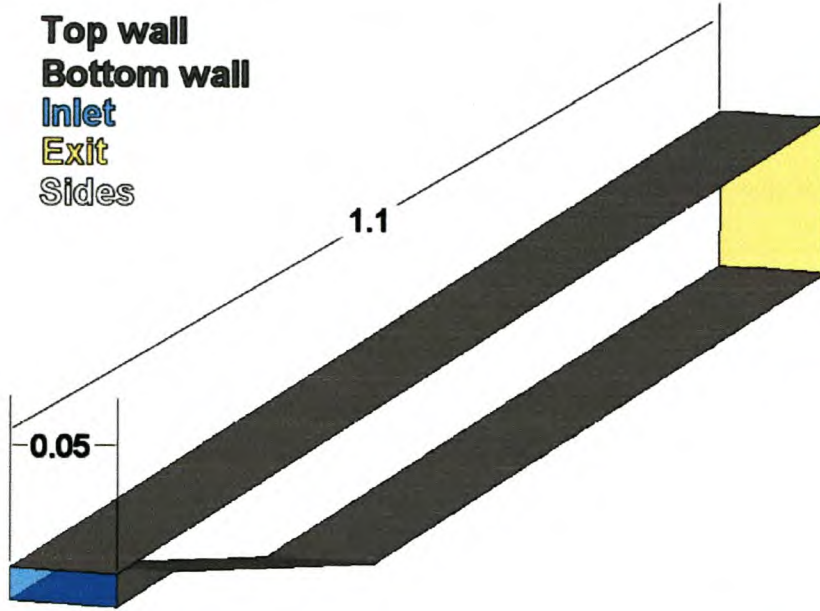


Figure 3.7: Computational domain for two-dimensional diffuser

Boundary Name	Boundary type	Value
Top wall	Wall	No slip
Bottom wall	Wall	No slip
Inlet	Inlet (Normal velocity)	Specified velocity profile
Exit	Outlet (Relative static pressure)	0 [Pa]
Sides	Symmetry	

Table 3.3: Boundary conditions for pipe flow problem

Having shown in section 3.2.1 that the solver calculates internal flow correctly on unstructured meshes, this problem was only simulated on an unstructured mesh. The surface mesh on the inlet, as well as on the upstream regions of the bottom wall and side is shown in figure 3.8.

The average edge length of elements in the inlet region was 1.5 mm, and 5 mm on the other bounding surfaces. The volume mesh average edge length was 7mm. The inflation layer on both walls consisted of 10 layers, increasing from a thickness of roughly 3 mm in the inlet region to about 15 mm downstream.

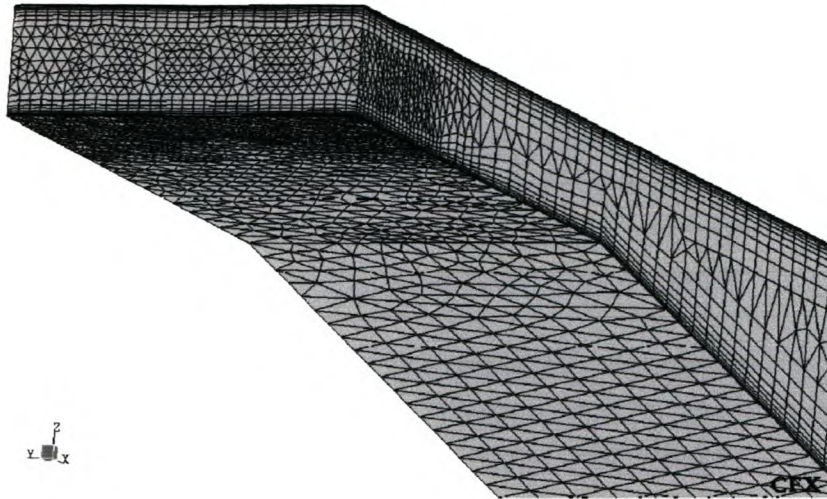


Figure 3.8: 2D diffuser: unstructured surface mesh

Figure 3.9 shows the experimental and numerically computed velocity profiles in the diffuser at streamwise stations $x/H = -5.87$, $x/H = 5.98$, $x/H = 20.32$ and $x/H = 27.09$.

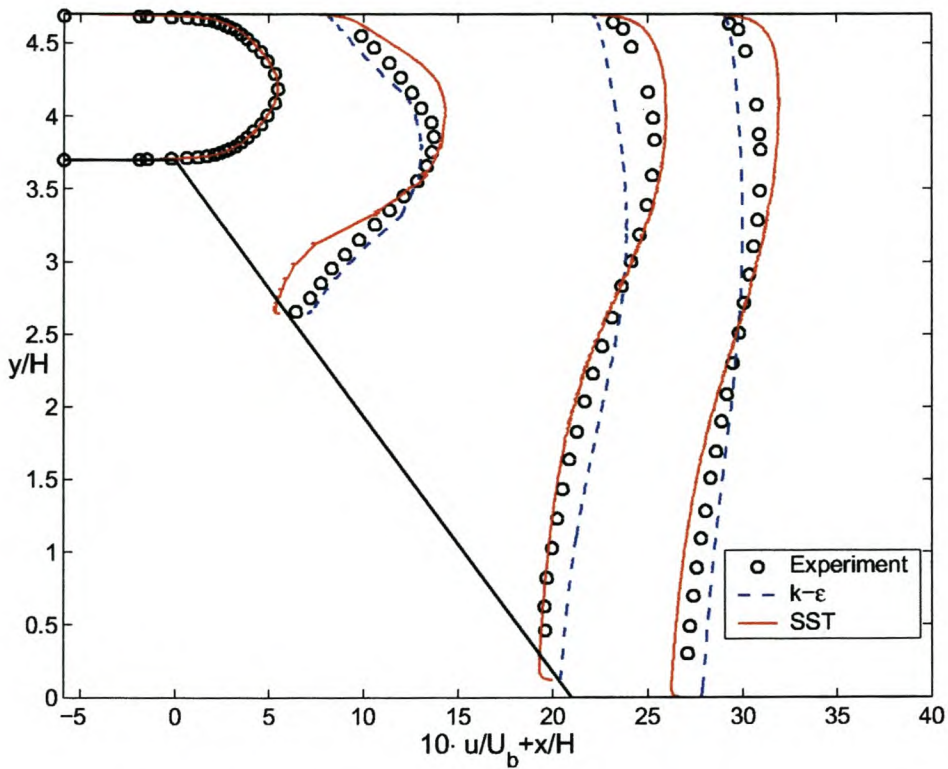


Figure 3.9: Velocity profiles in two dimensional diffuser

It is readily apparent that the SST turbulence model predicts the boundary layer separation successfully. It might be said that the model is somewhat too sensitive to the adverse pressure

gradient, since the separation point is predicted earlier than experiments suggest ($x/H = 1.2$ versus $x/H = 5.98$), and the reattachment point is also predicted further downstream ($x/H = 35.3$ versus $x/H = 27.09$).

The $k - \epsilon$ predicts no boundary layer separation, which is consistent with the overprediction of turbulent shear stress in the boundary layer (section B.4.1).

The pressure distribution along the bottom wall of the diffuser is shown in figure 3.10.

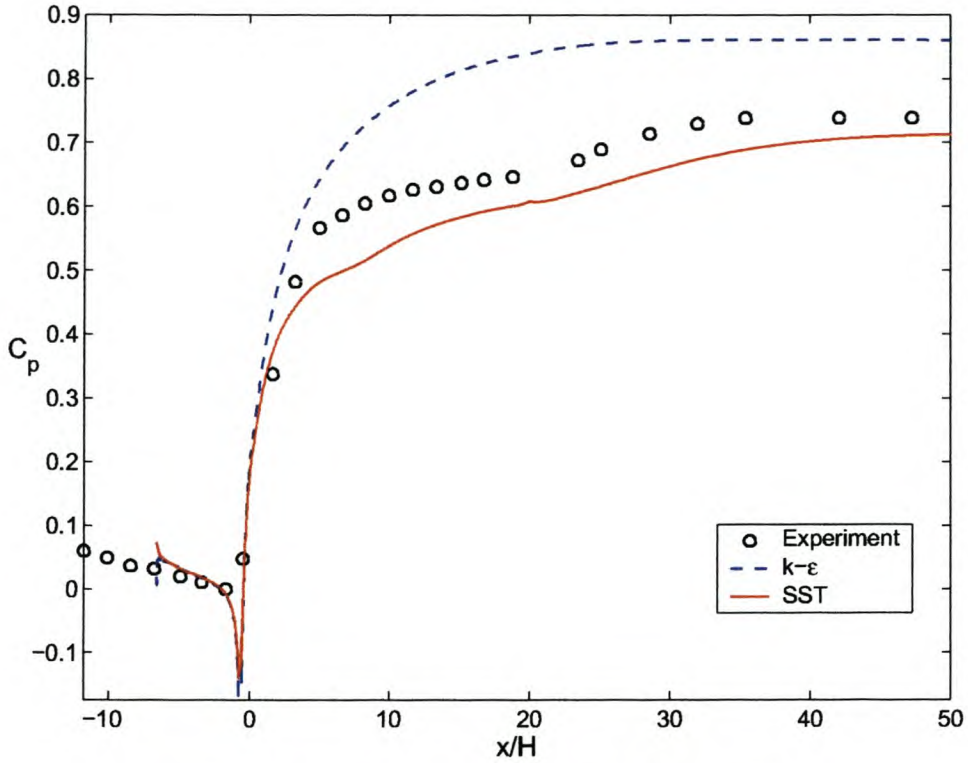


Figure 3.10: Pressure coefficient on bottom wall of diffuser

The values for C_p obtained from the SST model are lower than the experiments, due the larger degree of separation that is predicted. This leads to higher velocities close to the wall (as can be seen in figure 3.9). The SST results approach the experimental values as one moves downstream.

The $k - \epsilon$ model predicts values for C_p that are higher than the experimental values, because it does not capture the boundary layer separation and the associated drop in static pressure.

This validation case showed that the code successfully predicts boundary layer separation in internal flow, if the correct turbulence model is employed. The SST model is somewhat over-sensitive to flow separation in adverse pressure gradients. In a design situation this is not necessarily bad, because potential problem areas can then be easily identified and rectified.

3.2.3 RAE inlet model 2129

The RAE inlet model 2129 (M2129) consists of a circular inlet followed by an S-bend diffuser, as shown in figure 3.11. It is a side-mounted inlet with a horizontal symmetry plane.

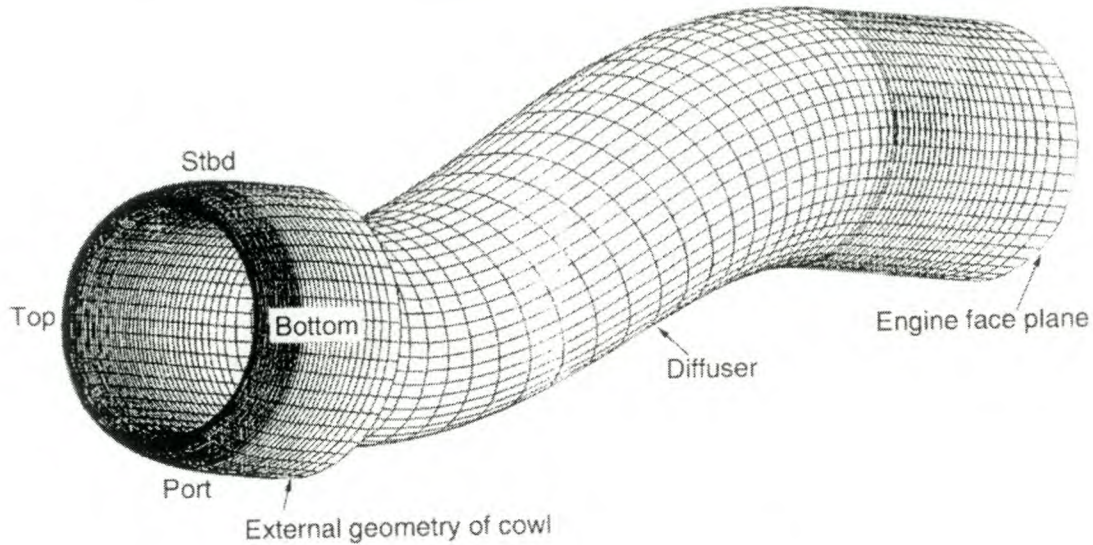


Figure 3.11: M2129 air inlet geometry [5, Chapter 4]

This inlet was a test case for the AGARD Fluid Dynamics Panel, Working Group 13 [15], as validation case for a number of CFD codes. In order to avoid having to specify complex entrance conditions for the internal flow problem, the complete flow from free-stream into the inlet were calculated. As specified in reference [15], two test cases were simulated: one with low mass flow and one with high mass flow through the duct. In both cases the free-stream Mach number was 0.21.

For the conditions explained in the previous paragraph, the flow accelerates into the inlet from a stagnation point on the outer cowl surface. Further acceleration occurs around the first bend on the starboard side of the inlet, where separation occurs. The faster moving core stream, under the influence of centrifugal and pressure forces, is moved towards the port side of the bend, where an adverse pressure gradient is encountered. The flow near the wall cannot pass through this adverse pressure gradient, and instead moves around the outside curve of the wall towards the lower static pressures on the starboard side. This movement, combined with the core flow moving towards the port side causes two cells of contra-rotating secondary flow [16].

The computational domain is shown in figure 3.12 and the boundary conditions are listed in table 3.4. An IGES file of the inlet geometry was supplied by Menzies [17]. The surface mesh on the cowl of the inlet, and on the first part of the diffuser is shown in figure 3.13. On both external and internal regions of the cowl the mean edge length was 20 mm, increasing to 40

mm downstream. There were 10 layers of mesh inflation with a thickness of 40 mm on the entrance and 80 mm downstream. The tetrahedral volume mesh had a mean edge length of 70 mm. For all simulations reported on in this section, the high-resolution advection scheme was used. Details of the simulations are given in section C.6.

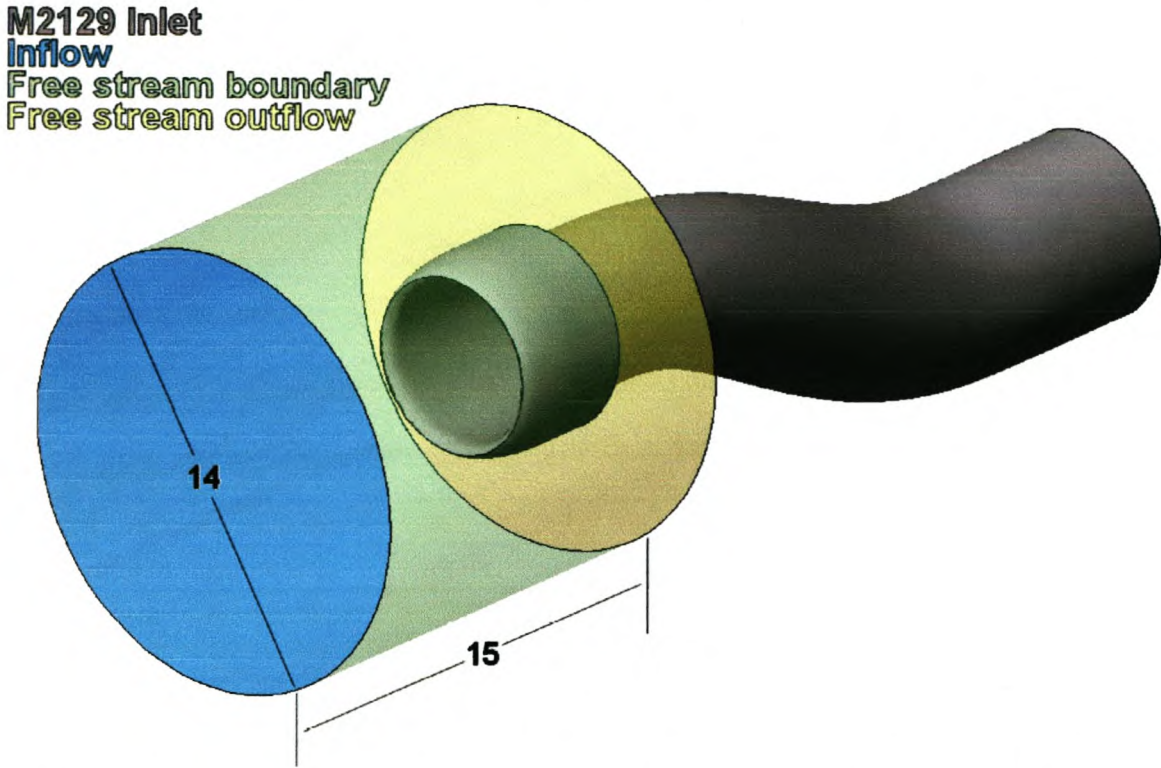


Figure 3.12: Computational domain for M2129 inlet simulation (dimensions in [m])

Boundary Name	Boundary type	Value
M2129 inlet	Wall	No slip
Inflow	Inlet	$M_\infty = 0.21$
Free stream boundary	Opening (Relative static pressure)	0 [Pa]
Free stream outflow	Opening (Relative static pressure)	0 [Pa]
Engine demand (not shown)	Opening (Relative static pressure)	As specified in text

Table 3.4: Boundary conditions for M2129 inlet simulation

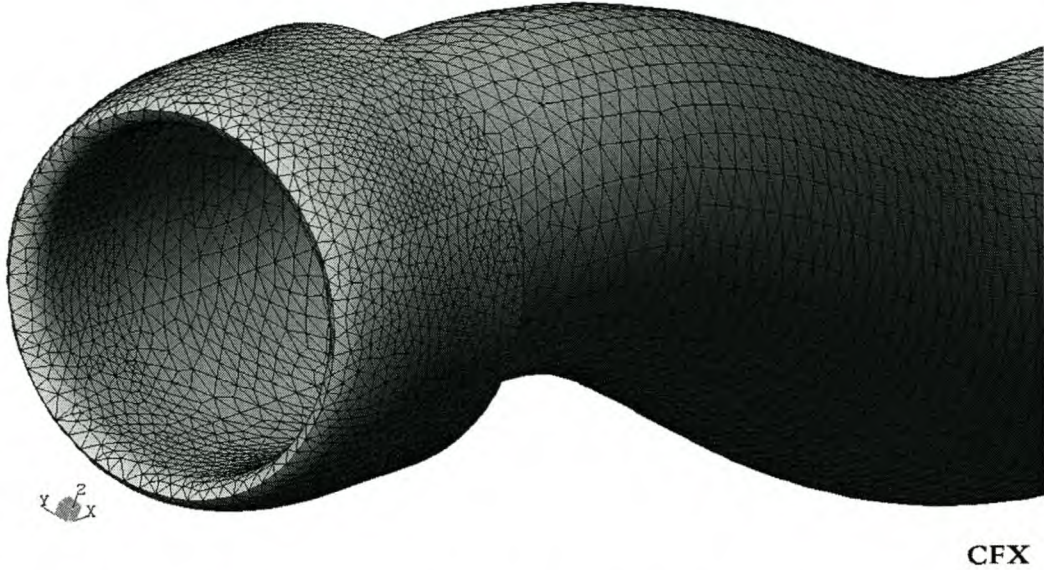


Figure 3.13: Surface mesh for M2129 inlet simulation

Low mass flow case

The experimental mean static pressure at the engine face of $0.922 \cdot p_\infty$ was used as the value at the engine face boundary [15, p.143]. The static pressures on the starboard side of the duct (where the influence of the separation and secondary flow is the most pronounced) is shown in figure 3.14, with the symmetry plane geometry superimposed for clarity. Note that in this section, the pressure coefficient is defined as

$$C_p = \frac{P_{wall}}{P_\infty} \quad (3.5)$$

The numerical results follow the experimental results closely, although predicting higher accelerations (and hence lower pressures) into the duct and around the first bend. The secondary flow can be seen as a “dip” in the pressure plot, downstream of the first bend. Both turbulent models predict significant secondary flow, with the SST model again predicting earlier separation than the $k - \varepsilon$ model. The recovery of static pressure downstream of the second bend is underpredicted by both models. The pressure recovery of the inlet (η as defined in equation 1.1) for the low mass flow case is presented in table 3.5. As expected from figure 3.14, the numerically computed pressure recovery values are lower than the experimental value.

	Experiment	$k - \varepsilon$	SST
η	0.990	0.962	0.959

Table 3.5: Pressure recovery, low mass flow case

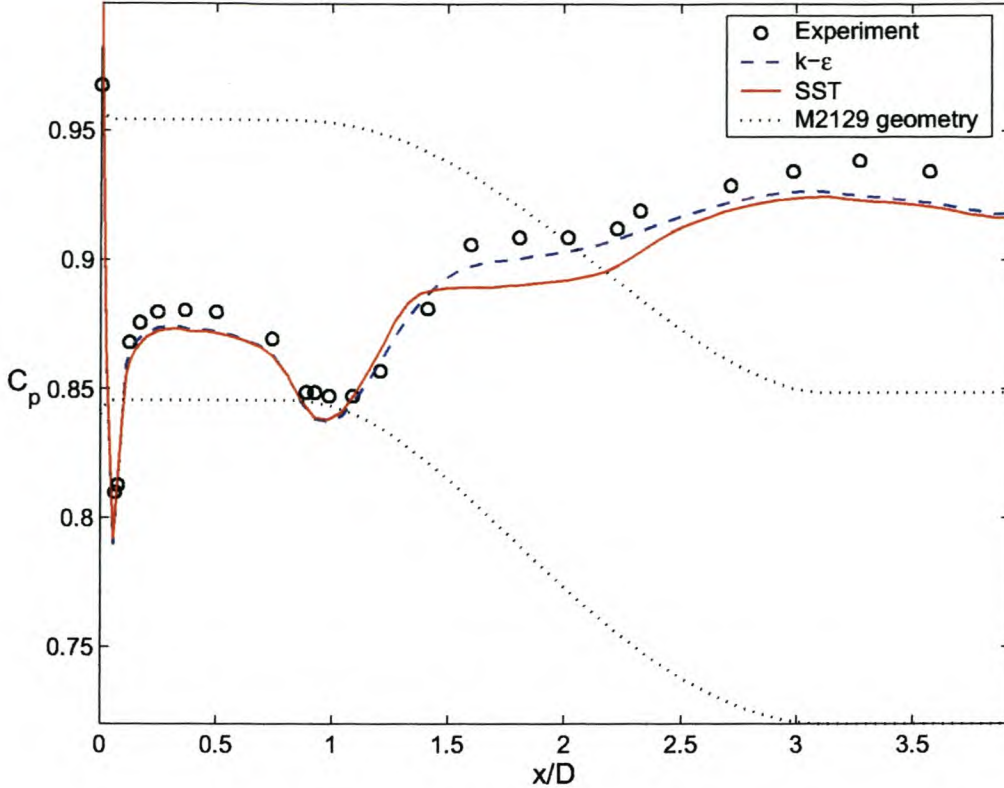


Figure 3.14: Pressure distribution on starboard side of M2129 inlet, low mass flow case

High mass flow case

The experimental mean static pressure at the engine face for the high mass flow case is $0.725 \cdot p_\infty$ [15, p.143]. With this value applied at the engine face boundary, the static pressures on the starboard side, as shown in figure 3.15, were obtained.

Reference [15] states that values of C_p below 0.52 indicate supersonic flow. The experimental results show a very high acceleration into the inlet, with supersonic flow up to $x/D \approx 0.45$. In the rear part of the constant diameter section the flow is subsonic again, but accelerates to supersonic speed around the first bend. At $x/D \approx 1.2$ the adverse pressure gradient in the diffusing section induces separation, where the local velocity is again subsonic.

Although the numerical results show high acceleration into the inlet, the local velocity just inside the duct is not as high as in the experiments, nor does the region of supersonic flow extend as far into the constant area section. Instead, the flow decelerates rapidly to subsonic speeds, and then accelerates (more smoothly than in the experiments) around the first bend. The $k - \epsilon$ model predicts this acceleration, as well as the separation and secondary flow downstream of the first bend very well. The SST model predicts a lower acceleration, coupled with stronger separation and secondary flow, as evidenced by the more pronounced dip in the pressure plot between $\frac{x}{D} \approx 1.2$ and $\frac{x}{D} \approx 1.6$. As for the low mass flow case, the recovery

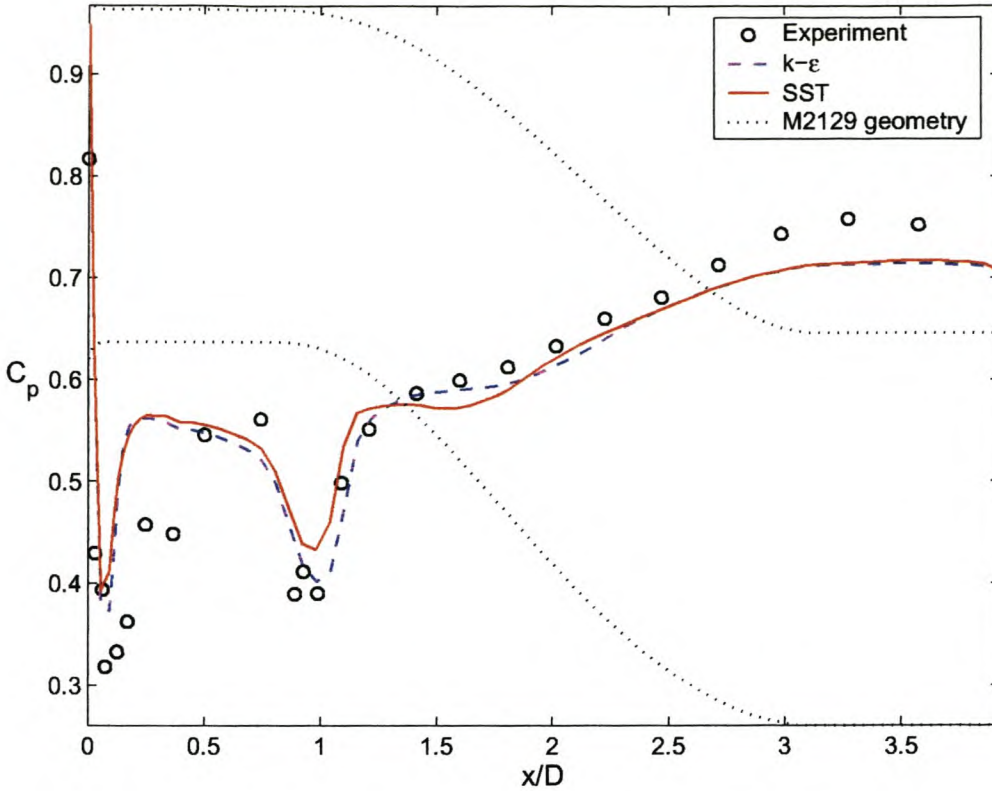


Figure 3.15: Pressure distribution on starboard side of M2129 inlet, high mass flow case

of dynamic pressure to static pressure in the rear part of the duct is lower than in the experiments. This is reflected in table 3.6.

	Experiment	$k - \varepsilon$	SST
η	0.928	0.830	0.830

Table 3.6: Pressure recovery, high mass flow case

In the high mass flow case especially, refinement of the mesh in the initial constant area section might lead to a better agreement with the experimental results in that region. Despite the differences between the experimental and numerical results, the correlation between them in both the low and high mass flow cases are satisfactory for the purpose of code validation.

3.3 Closure

The validation cases in this chapter dealt with internal flow problems ranging from simple to complex geometries, including adverse pressure gradients and flow separation. The numerical results obtained in all cases show a satisfactory agreement with the various previously known results. This allows us to draw the conclusion that quantitative results obtained on an “un-

known” geometry can be trusted to be indicative of the “real” flow situation. Coupled with the external flow validation in chapter 2 the implication is therefore that this code can be a useful tool in the design stage of a project. Frequently however, in this and the previous chapter, results from a particular simulation were accepted when they were deemed to be close enough to the known values. On a “new” geometry, one does not have the luxury of previously known results for comparison. It is therefore much more important to correctly set up the mesh to ensure grid independence in the critical regions of the problem.

Chapter 4

CFD modelling of first-order design; redesign

4.1 Background

The first-order design for the mission-adaptive air inlet, as presented in section 1.6, was subjected to a series of preliminary CFD simulations. The focus was on getting results in as short a time as possible. These results were evaluated qualitatively to identify weaknesses in the design.

In this chapter, selected results from these simulation are presented and examined. This leads to a set of criteria for the adaptation of the design to correct unfavourable flow characteristics. Finally, a redesign is presented.

4.2 Numerical simulation

4.2.1 CFD models

The internal and external geometries of the UCAV, as presented in section 1.6, were combined in the CFD pre-processor, to obtain the final geometry for which the flow was solved. This combined geometry is shown in Figure 4.1.

To solve the whole flight regime of the UCAV would have involved a prohibitive number of CFD simulations. It was therefore decided to simulate only the flight conditions most likely to be experienced. Referring to table A.1, it is clear the most time is spent flying straight and level. In light of this, only flight at zero angle of attack was considered. The flow was assumed to be steady. The full set of simulations that was run is listed in Table 4.1.

Simulations were not run for the “bump up” configurations at speeds below $M_\infty = 0.5$. The reason is that the bump would only be raised in situations of high radar threat (during the

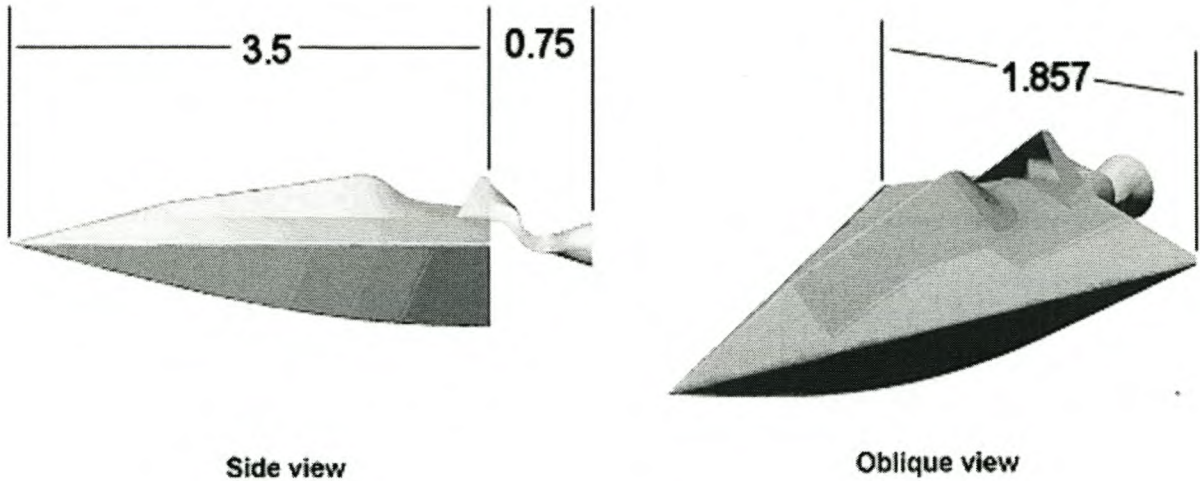


Figure 4.1: Combined geometry (dimensions in [m])

Free stream Mach number	Bump down	Bump up
0.2	X	
0.3	X	
0.4	X	
0.5	X	X
0.6	X	X
0.7	X	X
0.8	X	X
0.9	X	X

Table 4.1: Simulations run on first-order design

mission phase), and according to Table A.1 flight Mach numbers from 0.5 to 0.9 are expected during this phase of flight.

The boundaries of the computational domain are shown in figure 4.2, and explained in table 4.2. Note that “Free stream boundaries” refers to all four boundaries perpendicular to the Inflow boundary. The engine demand boundary is not shown in figure 4.2 but is located at the rear end of the duct.

Boundary Name	Boundary type	Value
UCAV geometry	Wall	No slip
Inflow	Inlet	As specified in table 4.3
Free stream outflow	Outlet (Relative static pressure)	0 [Pa]
Free stream boundaries	Opening (Relative static pressure)	0 [Pa]
Engine demand (not shown)	Outlet (Mass flow rate)	As specified in table 4.3

Table 4.2: Boundary conditions for simulation of first-order design

UCAV geometry
 freestream inflow
 freestream outflow
 freestream
 boundaries

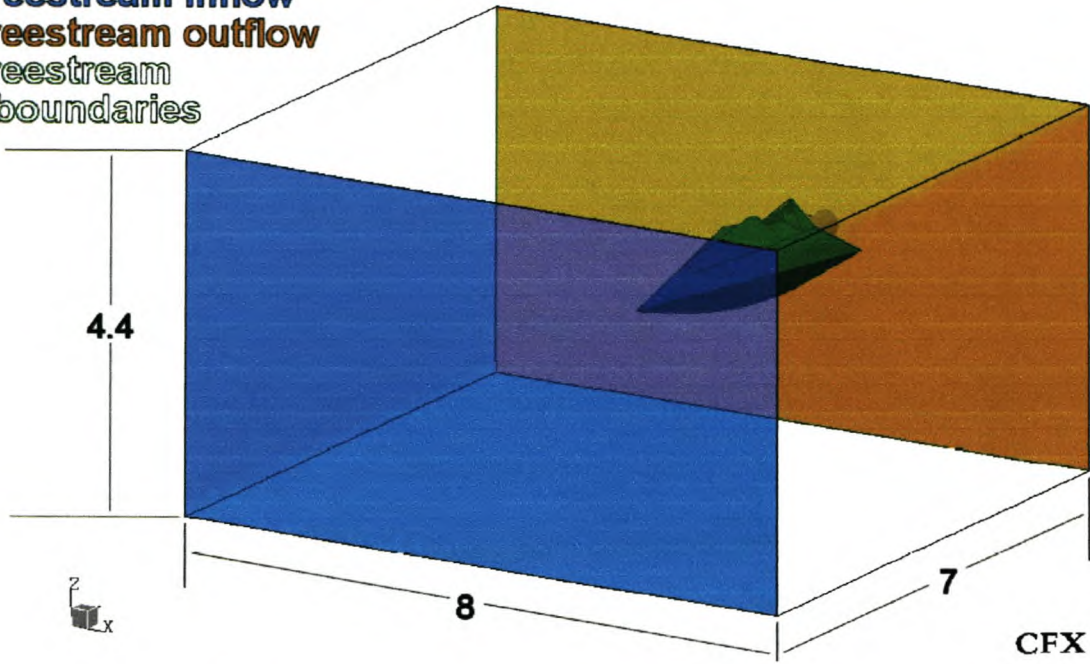


Figure 4.2: Computational domain for simulation of first-order design (dimensions in [m])

Table 4.3 lists values at the inflow and engine demand boundaries at the different free stream Mach numbers. In all cases the free stream static pressure and temperature were 101325 Pa and 288.16 K respectively.

M_∞	V_∞ m/s	\dot{m}_{engine} kg/s
0.2	68.07	6.11
0.3	102.10	6.31
0.4	136.13	6.51
0.5	170.16	6.85
0.6	204.20	7.18
0.7	238.23	7.64
0.8	272.26	8.18
0.9	306.30	8.82

Table 4.3: Inflow and engine demand boundary condition values

The engine mass flow values in table 4.3 were obtained from the program discussed in section A.4. Although the maximum mass flow through the engine is 6.5 [kg/s], the program can compute theoretical values in excess of this maximum.

It can be shown (see section A.4) that the free stream area of the captured streamtube (see figure A.4) is only a function of free stream Mach number, and not of flight altitude. For a

fixed inlet capture area A_c , the inverse flow ratio μ (see section 1.3) would therefore also be a function of free stream Mach number only. As mentioned in section 1.3, the inlet pressure recovery is solely dependent on the value of μ . Therefore, the performance of the inlet is only a function of free stream Mach number, and because the flow at a particular Mach number is similar for all altitudes, (since μ stays constant regardless of altitude) flight at only *one* altitude needs to be simulated.

It has to be emphasised that in reality, flight speeds at sea level in excess of $M_\infty > 0.4$ would be impossible since it would require mass flow through the engine that is higher than the allowable maximum (see figure A.3). For the sake of simulation these higher mass flow rates and flight speeds are acceptable though, because of the flow similarity discussed in the previous paragraph.

The surface mesh on the duct is shown in figure 4.3. The average edge length of elements on the duct was 10 mm, on the bump it was 20 mm and 30 mm on the rest of the UCAV geometry. To reduce the set-up time of the volume mesh, no mesh inflation was employed. The average edge length of the tetrahedral volume mesh in the free stream was 200 mm.

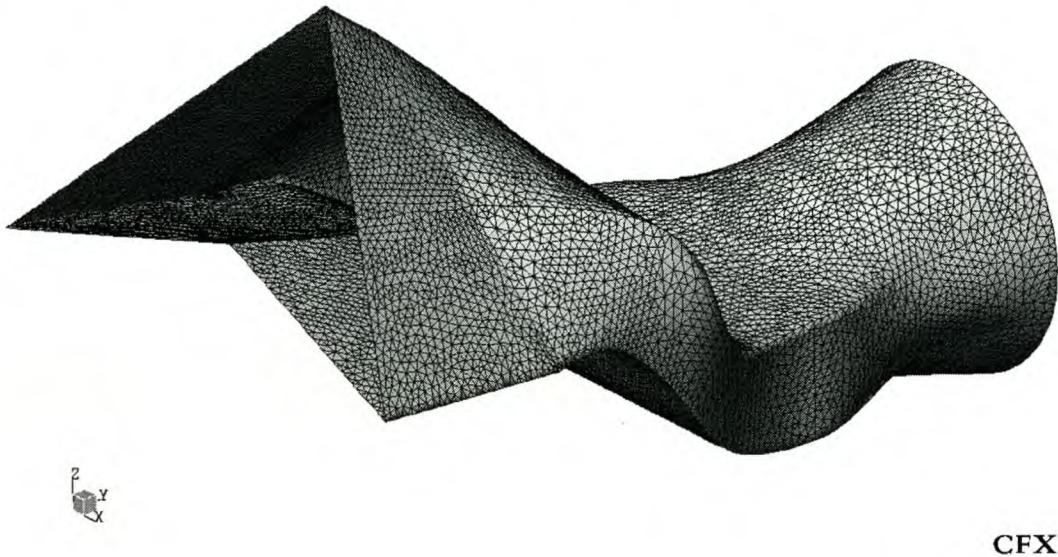


Figure 4.3: Surface mesh on duct for first-order design

These preliminary simulations were run using the $k - \epsilon$ turbulence model and the first-order (UDS) advection scheme. In light of the code validation reported on in chapters 2 and 3, the quantitative results obtained from the UDS scheme are generally not very accurate. Since the main goal of these simulations were to obtain a “picture” of the flow, the robustness of the UDS scheme, coupled with relatively short solution times, outweighed the loss in accuracy.

4.2.2 Simulation results

Because of the employment of the UDS advection scheme, and the absence of mesh inflation, it was recognised that quantitative results were not to be accepted as representative of the real situation. The results presented in this section should therefore be interpreted in terms of the trends they show, and not the values of the physical variables.

Bump-down configuration

The graphical results shown here are for $M_\infty = 0.6$, for which the numerical results were representative of the majority of simulations for the bump-down configuration.

Figure 4.4 is a side view of the bump / inlet region. Here, streamlines calculated in an upstream direction from the plane of the engine face show that the flow is turned sharply at the sloped internal rear wall of the inlet, and that the top portion of the inlet does not supply air to the engine. This is confirmed by a vector plot (on the symmetry plane of the geometry) of the flow entering the inlet (Figure 4.5), showing flow spilling over the front lip of the inlet.

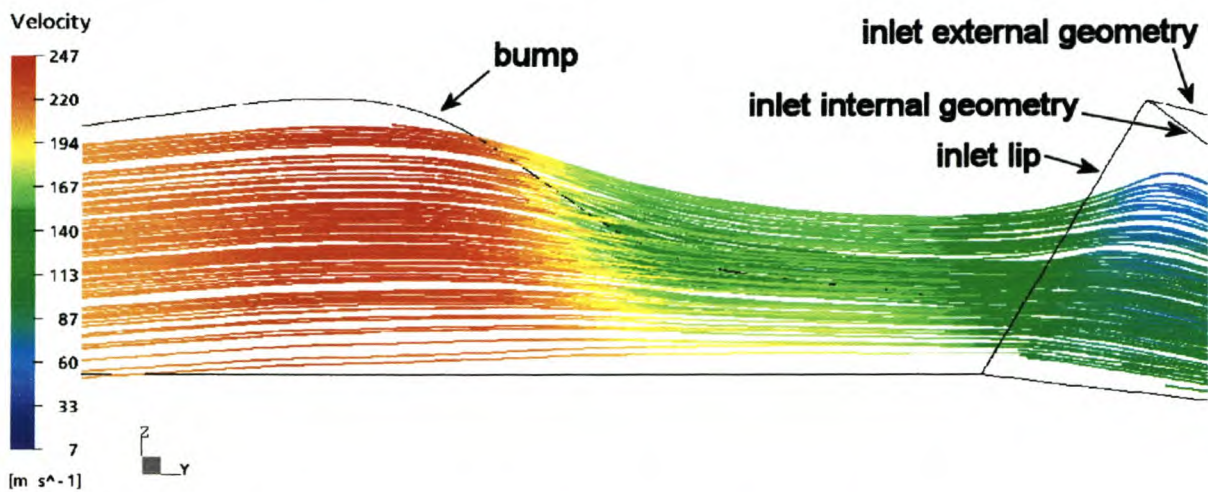


Figure 4.4: Inlet streamlines, bump down, $M_\infty=0.6$

Contour plots of velocity and total pressure at the engine face (Figure 4.6) shows substantially higher values for these variables at the bottom part of the duct exit than at the top. This is probably due to a more “straight through” path for the flow near the bottom of the duct. The contours are not perfectly symmetric about the YZ plane, but this can be attributed to the fact that the mesh on the engine face plane was also not perfectly symmetric, rather than the solution being asymmetric.

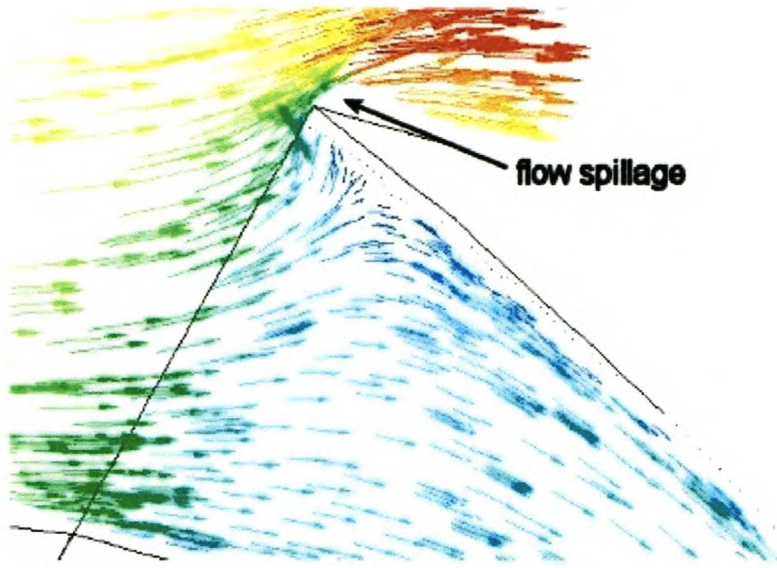


Figure 4.5: Inlet velocity vectors, bump down, $M_\infty=0.6$

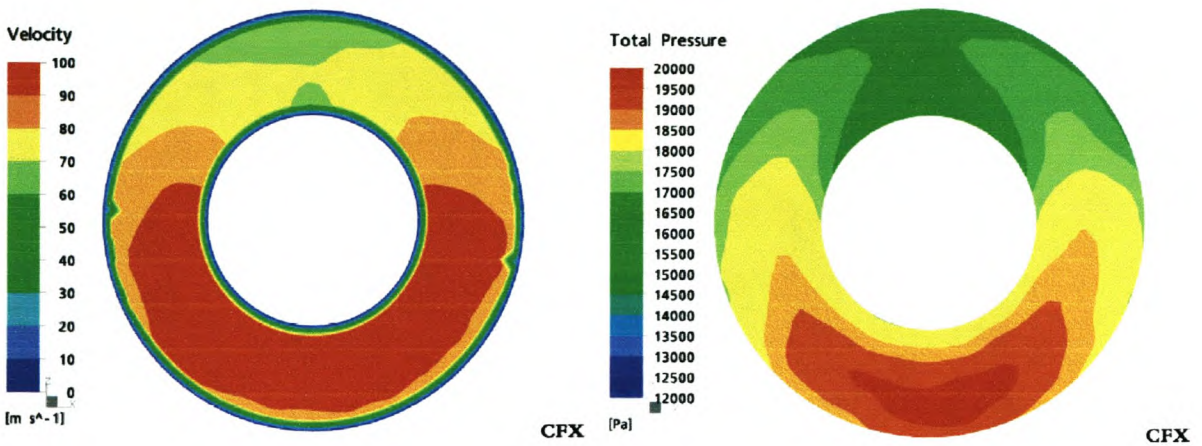


Figure 4.6: Velocity and total pressure contours at engine face (bump down, $M_\infty=0.6$)

Bump-up configuration

The inlet streamtube for this configuration is shown in figure 4.7. Compared to figure 4.4, there is a bigger area of high speed flow ahead of the inlet, which translates to more friction, and the associated loss in total pressure. There is also slightly less flow spillage over the front lip of the inlet.

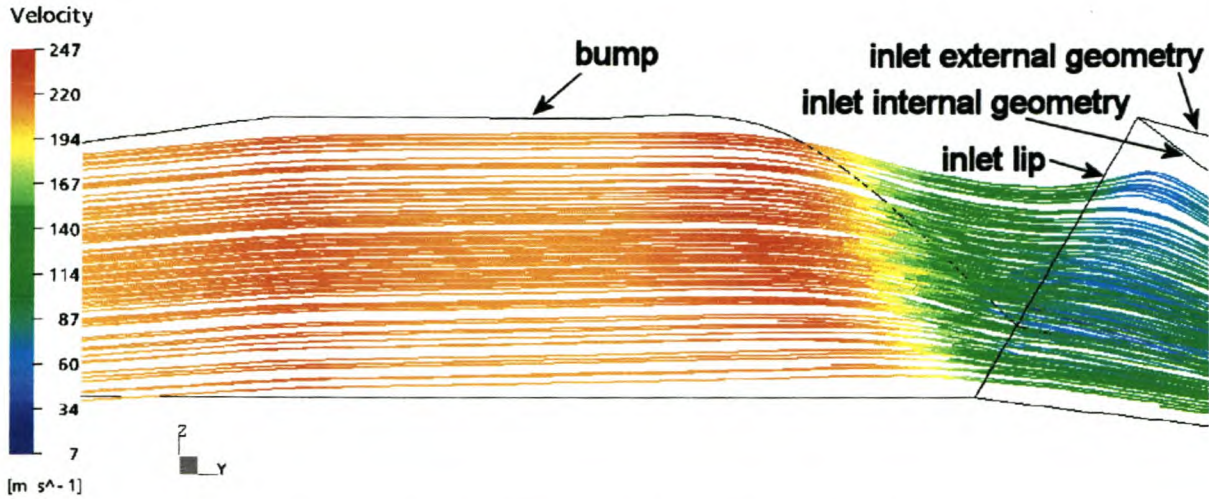


Figure 4.7: Inlet streamlines, bump up, $M_\infty=0.6$

Velocity and total pressure profiles at the engine face (figure 4.8) are slightly more distorted, when compared to the bump-down simulation at the same free stream Mach number. Comparing the magnitudes of the total pressure values at the engine face, it is clear that there is an additional loss in total pressure due to the raised bump, which can be attributed to the greater friction loss as mentioned in the previous paragraph. It is re-iterated that the specific values should not be taken as “correct”, but the trend is obvious.

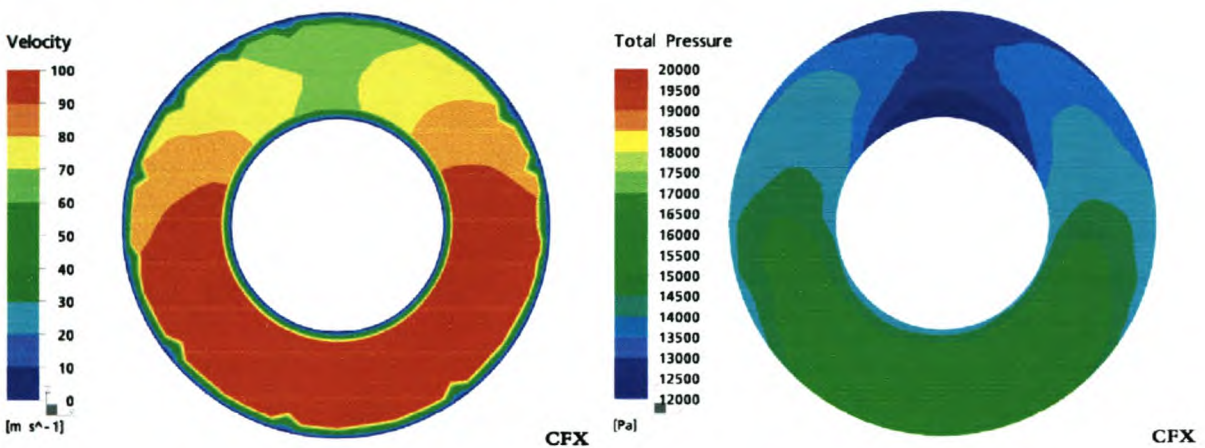


Figure 4.8: Velocity and total pressure contours at engine face (bump up, $M_\infty=0.6$)

In the “bump-up” configuration, some flow separation occurs at the back of the bump at free stream Mach numbers of 0.7 and higher, as shown in figure 4.9. Compared to the “bump-down” configuration, where the air flows smoothly around the bump without separation, this contributes to an even greater loss in total pressure at the engine face.

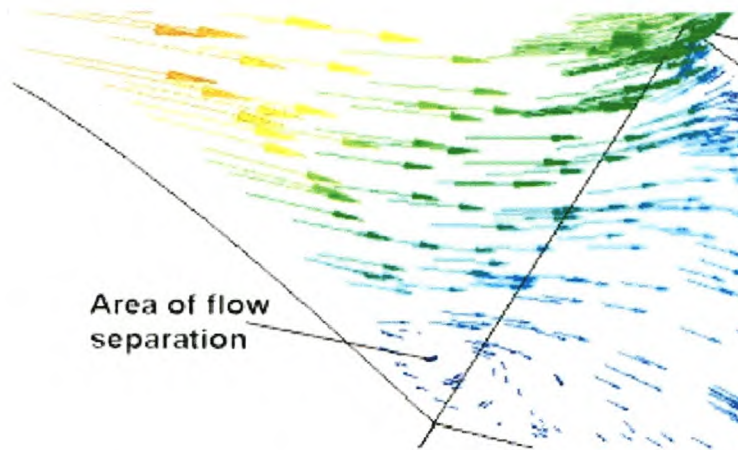


Figure 4.9: Flow separation, bump up, $M_\infty=0.8$)

4.2.3 Conclusions from simulation results

1. Significant spillage drag will result from the flow spilling over the inlet lip.
2. The high angle at which the flow impinges on the back wall of the inlet leads to considerable stagnation pressures in that region, resulting in an increase in internal drag of the inlet.
3. The variation of the velocity and total pressure profiles across the engine face will respectively result in the variation of the flow angle seen by the compressor blades and a lowering of the effective surge line of the compressor. Both of these factors can cause the compressor to stall [6, pp.278-80], [5, p. 270].
4. Separation of the external flow in the “bump-up” configuration has a detrimental effect on flow conditions in the duct.

These conclusions lead naturally to criteria for the redesign of the inlet and duct:

1. Spillage at the inlet lip must be eliminated or kept to a minimum.
2. Flow angle at the internal walls of the inlet must be minimised.
3. Flow separation in the “bump-up” configuration must be eliminated.

4.3 Redesign

4.3.1 Inlet entrance

To minimise the angle at which the flow impinges on the internal walls of the inlet, the geometry was adapted to have an inlet angle that is approximately the same as the local flow angle just in front of the inlet (Figure 4.10).

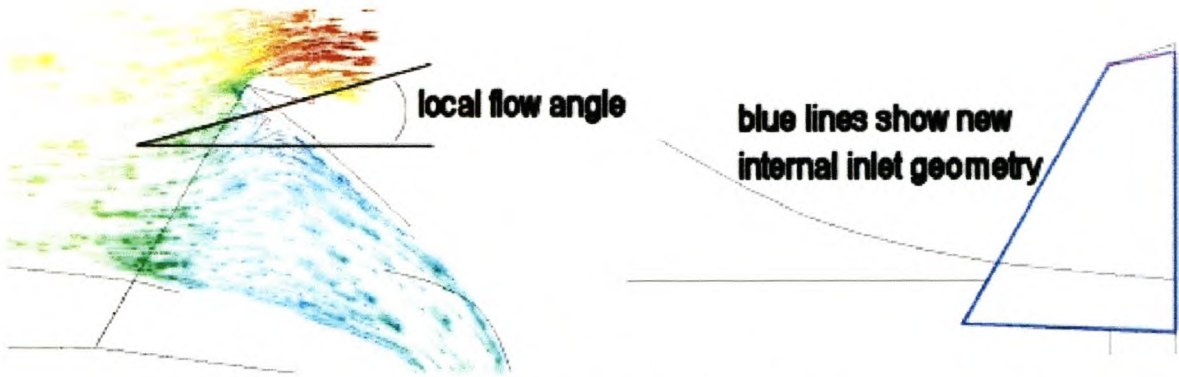


Figure 4.10: Comparison between local flow angle and new inlet geometry

Furthermore, the back of the inlet is shaped to change the flow direction into the duct more gradually, as shown in Figure 4.11.

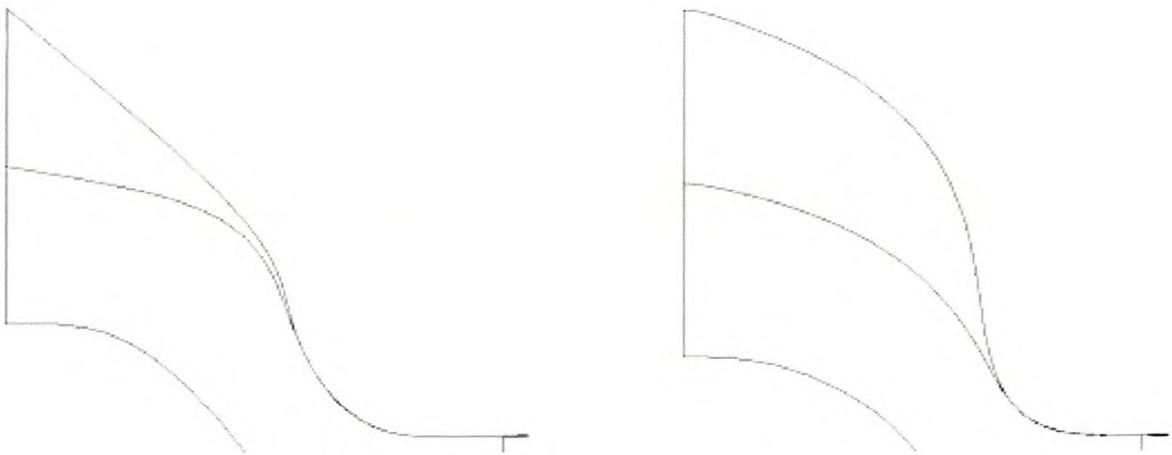


Figure 4.11: Comparison between first-order and new duct geometries

4.3.2 Bump geometry

To address the problem of flow separation at the back of the bump when it is raised, the shape was changed from a constant width profile (seen from the top) to a tapering profile, as shown

in Figure 4.12. The height, as seen from the side, was not changed.

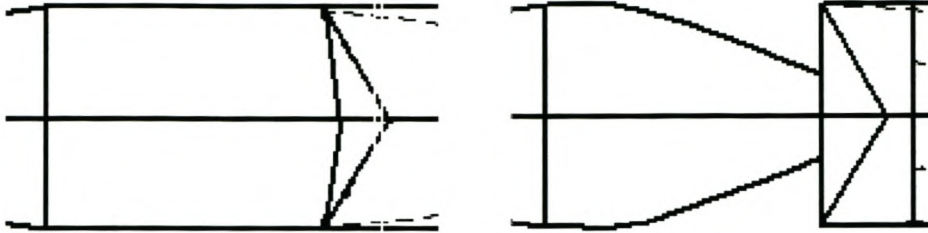


Figure 4.12: Comparison between first-order and new bump geometries

The argument for this change was that it should allow for smooth flow into the inlet in both “bump-down” and “bump-up” configurations, because the air would flow “around” rather than “over” the bump.

4.4 Closure

A number of detail changes were applied to the inlet and duct design, after a series of preliminary CFD simulations. These changes were due to qualitative observations of the flow behaviour.

Two deficiencies of these simulations were the absence of mesh inflation and the fact that only the UDS advection scheme were used.

Simulation of the modified design is the subject of the next chapter.

Chapter 5

CFD modelling of second-order design

5.1 Objectives

This chapter reports on the CFD simulation of the second-order design for the mission-adaptive UCAV inlet. These simulations were markedly different to those on the first-order design, both in terms of the modelling and the desired outcomes.

As opposed to the work discussed in chapter 4, the objective of which was to get an idea of the general flowfield around the UCAV and into the inlet, the main objective of this set of simulations was to quantitatively characterise the performance of the inlet. This is compared to a theoretical prediction of the inlet pressure recovery. The results are explained in terms of the predicted flowfield, and the chapter concludes with suggestions on how to increase the performance of the inlet.

5.2 CFD model

The validation of the software (chapters 2 and 3) showed that the quantitative results obtained from a particular simulation can be trusted if

1. the applied boundary conditions are consistent with the real flow situation,
2. the mesh adequately resolved the flowfield, and
3. the numerical model gives realistic results in regions of high variable gradients.

In the simulations of the first-order design, only the first of these conditions were satisfied. Because no mesh inflation was used, the boundary layer flow was not adequately resolved. Coupled with the fact that just the UDS advection scheme was employed, this disguised the effects of the strong adverse pressure gradient directly in front of the inlet, as will be shown in this chapter.

The computational domain is shown in figures 5.1 and 5.2, and the boundary conditions are given in table 5.1.

UCAV geometry

Inflow

Free stream outflow

Free stream boundaries

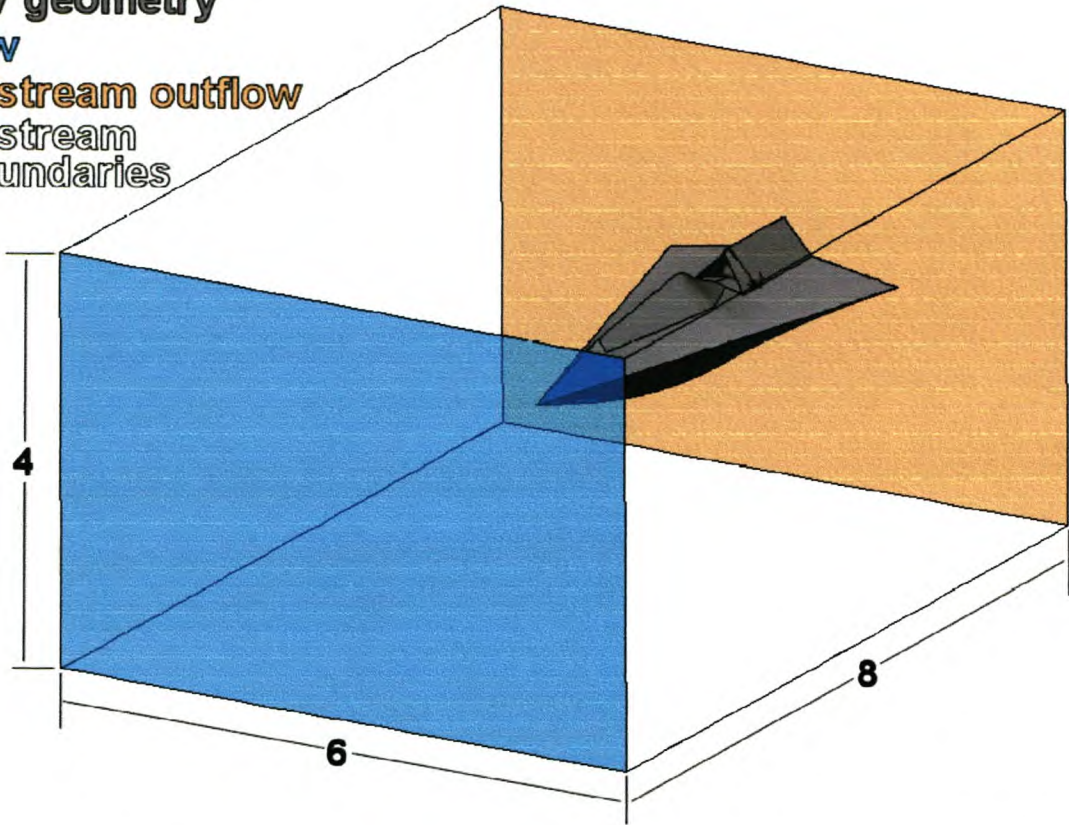


Figure 5.1: Computational domain for second-order design: external flow (dimensions in [m])

Boundary Name	Boundary type	Value
UCAV geometry	Wall	No slip
Inflow	Inlet	As specified in table 4.3
Free stream outflow	Opening (Relative static pressure)	0 [Pa]
Free stream boundaries	Opening (Relative static pressure)	0 [Pa]
Duct	Wall	No slip
Engine demand	Outlet (Mass flow rate)	As specified in table 4.3
Centerbody	Wall	No slip

Table 5.1: Boundary conditions for simulation of second-order design

The free stream speeds and engine mass flow values were identical to those used in the simulation of the first-order design (table 4.3). Free stream static pressure and temperature was set at 101325 Pa and 288.16 K respectively.

In the model of the first-order design, the free stream outflow boundary was located very close to the inlet entrance, and the engine demand boundary was coincident with the engine face

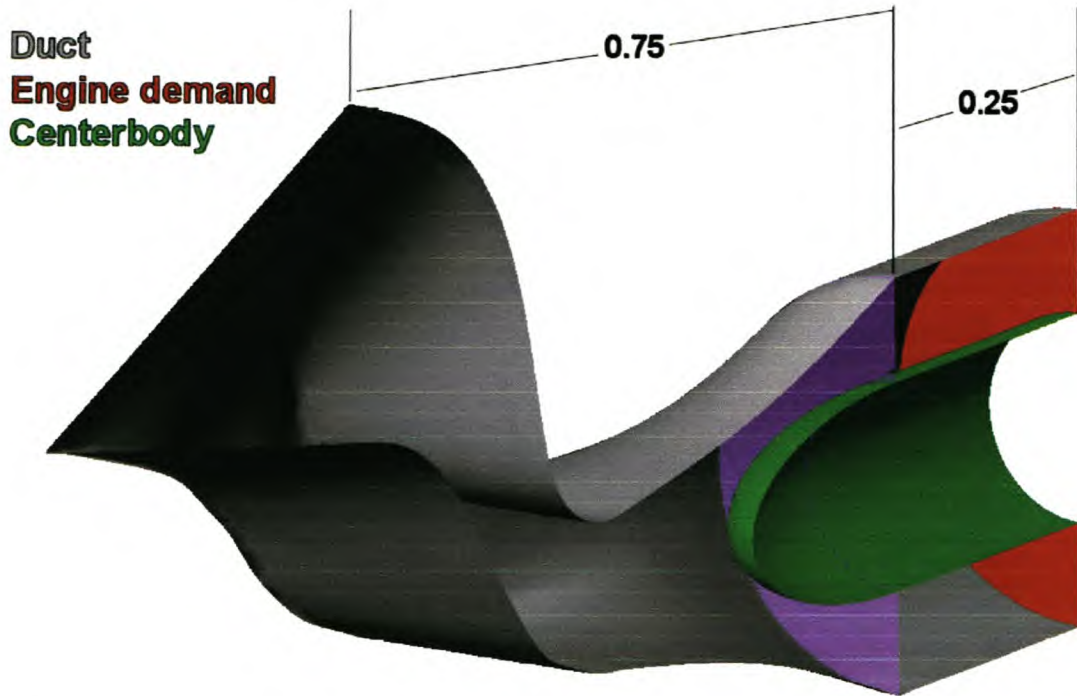


Figure 5.2: Computational domain for second-order design: internal flow (dimensions in [m])

plane in the “real” geometry. For the second-order design, the boundaries were moved away from these important regions of the flow. The free stream outflow was moved back by 1 metre, and a constant height “spine” was added to keep a smooth flow geometry. Also, the engine demand boundary was moved back by 0.25 m from the engine face plane (shown in purple in figure 5.2, to prevent the application of the mass flow boundary condition from interfering with the solution at the engine face plane.

The surface mesh on the external geometry is shown in figure 5.3, around the inlet entrance in figure 5.4, and on the duct in figure 5.5. Only the bump-down case is shown in figure 5.3, but the mesh on the bump-up case is similar.

The average edge lengths of the elements on the surfaces are given in table 5.2.

On each of the surfaces in table 5.2 there were 10 layers of mesh inflation, up to a height equal to 1.5 times the mean element edge length on that surface. The average edge length of the tetrahedral volume mesh was equal to that of surface mesh close to the body, increasing to 0.25 m in the free stream. This led to a total of approximately 660 000 elements in the volume mesh. This was at the limit of the computing power available. An even finer mesh was generated but the simulation would not run effectively because the entire mesh could not be loaded into the computer’s RAM.

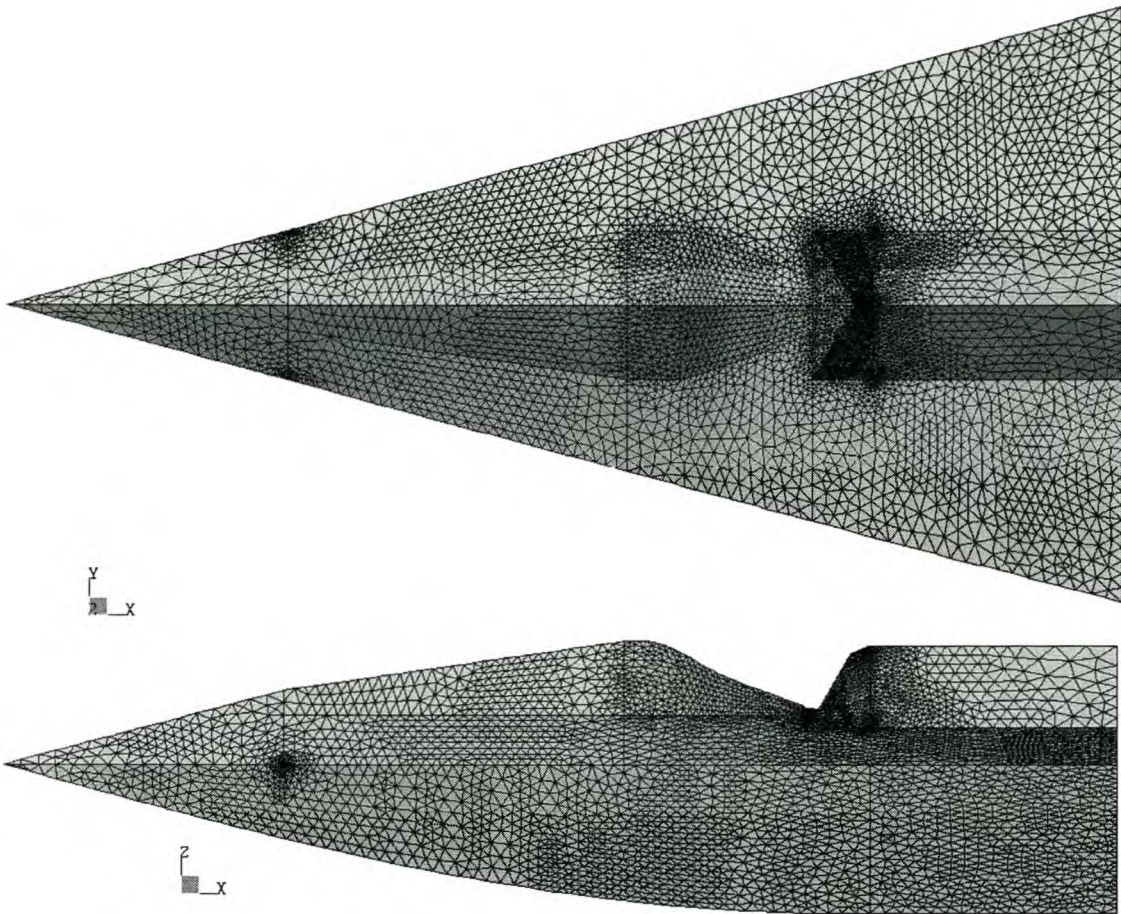


Figure 5.3: Surface mesh on external geometry: plan view (top), elevation (bottom)

Geometry	Average edge length
Wings	50 mm
Fuselage bottom	50 mm
Bump (front)	50 mm
Bump (rear)	30 mm
Inlet entrance (external flow)	20 mm
Inlet entrance (internal flow)	15 mm
Spine	50 mm
Duct	15 mm
Centerbody	10 mm

Table 5.2: Average edge lengths of surface elements

The code validation also brought to light that the results from simulations which used the UDS advection scheme were much less accurate than those which used the higher order schemes. In general the high resolution scheme produced results which were the most satisfactory, and was

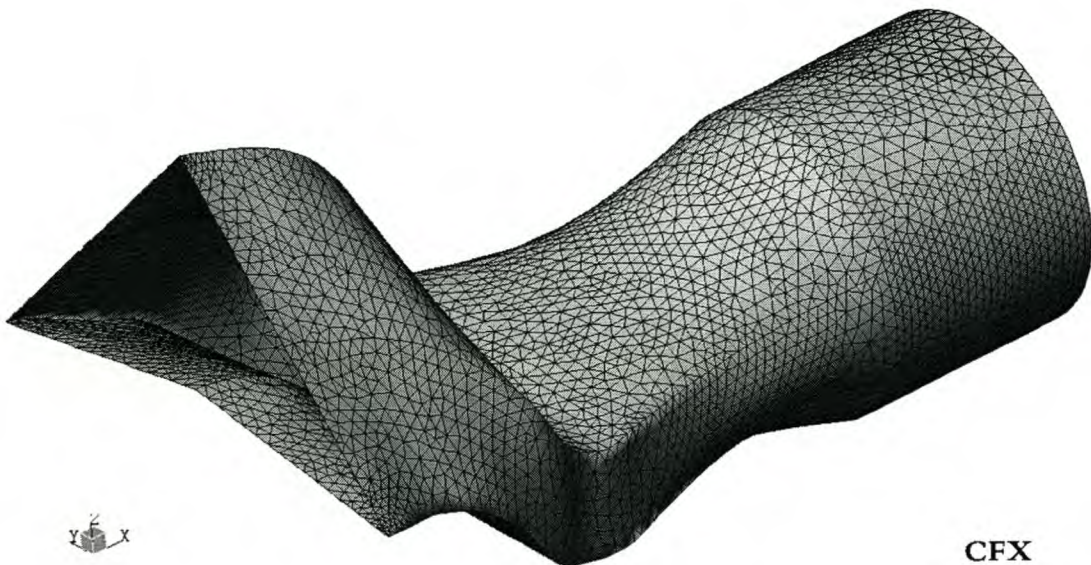
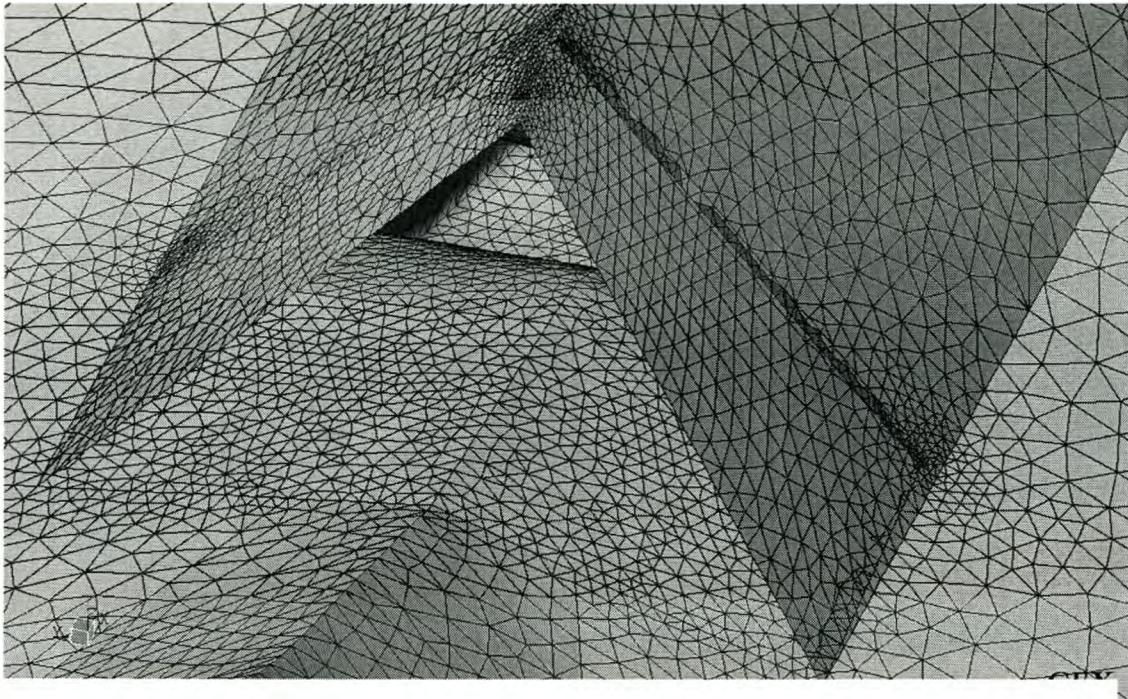


Figure 5.5: Surface mesh on duct

therefore chosen as advection scheme for the simulations of the second-order design. Similarly, it was decided to use the $k - \varepsilon$ turbulence model in preference to the SST model. It generally performed better in the validation cases, especially in the simulation of the M2129 S-duct diffuser (section 3.2.3), which is roughly similar in geometry and application to the UCAV inlet.

Higher order advection models are less robust than first-order models and therefore need well-defined initial conditions to remain stable in the first few iterations. Here the UDS scheme shows it worth in generating initial conditions for the higher order schemes. For the simulations discussed in this chapter, the constant pressure openings at the free stream boundaries (see figure 5.1 and table 5.1) were replaced by free-slip walls in the initial simulations employing the UDS scheme, after it was found that the simulations became unstable. This modification ensured a set of initial conditions that were sufficient to ensure that the high resolution simulations were stable, even when using the less robust boundary conditions.

The details of the numerical simulations are tabulated in section D.2.

5.3 Inlet performance

5.3.1 Theoretical prediction

As a baseline to compare the numerical results against, the theoretical performance of the inlet was determined using the theory of friction loss, as described in section 1.3. This measures the inlet performance as a value of $C_{\Delta P}$, defined in equation 1.2, and repeated here as equation 5.1 for convenience:

$$C_{\Delta P} = \frac{P_{\infty} - P_f}{q_c} \quad (5.1)$$

The inlet capture (c) and engine face planes (f) for the UCAV inlet are defined in figure 5.6.

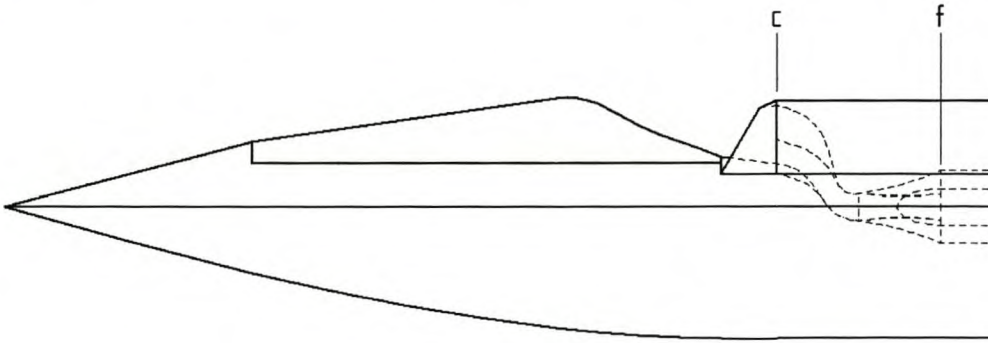


Figure 5.6: Location of inlet capture and engine face planes

The theory of friction loss states that $C_{\Delta P}$ can be computed from equation 1.3, which contains the duct integral I , given by equation 1.4. This integral was approximated by the summation

$$I \approx \sum_{\ell_c}^{\ell_f} \left(\frac{A_c}{A} \right)^2 \frac{\rho}{A} \delta \ell \quad (5.2)$$

in increments of $\delta \ell = 25$ mm from ℓ_c to ℓ_f . This gave a value for I of 28.4.

The inlet capture area is 0.0765 m^2 and the fuselage area wetted by the inlet streamtube is 2.105 m^2 . Using a value for k (which refers here to an empirical constant, *not* the turbulent kinetic energy) of 0.8 as suggested in reference [5], the corrected position ratio J of the inlet has a value of 22.0 for the bump-down case and 28.6 for the bump-up case.

C_{Fd} , C_{Fa} and μ varies with M_∞ , giving values for $C_{\Delta P}$ as shown in table 5.3. Subscript “bd” refer to the bump-down case and “bu” to the bump-up case.

M_∞	C_{Fd}	C_{Fa}	μ	$C_{\Delta P, bd}$	$C_{\Delta P, bu}$
0.2	0.00959	0.00274	1.0431	0.341	
0.3	0.00954	0.00258	1.5151	0.469	
0.4	0.00948	0.00248	1.9580	0.680	
0.5	0.00940	0.00241	2.3261	0.934	1.132
0.6	0.00932	0.00235	2.6630	1.242	1.532
0.7	0.00921	0.00230	2.9197	1.524	1.898
0.8	0.00910	0.00226	3.1166	1.767	2.214
0.9	0.00898	0.00223	3.2517	1.942	2.442

Table 5.3: Theory of friction loss: parameters and results

Theoretical values for P_∞ , ρ_c and V_c can be determined from the general relations for compressible flow, which then allows the determination of P_f from $C_{\Delta P}$.

5.3.2 Numerical results

The dynamic pressure at the inlet capture plane was determined from the averages of the numerically computed density and velocity over the area of that plane. Total pressure was obtained at a point in the free stream streamtube. As first validation of the numerical results, the absolute free stream total pressures and capture plane dynamic pressures are compared in tables 5.4 and 5.5 with the theoretical values. Pressure values are given in Pascal and the errors are percentages.

M_∞	$P_{\infty, th}$	$P_{\infty, bd}$	$\text{Diff}_{P_{\infty, bd}}$	$P_{\infty, bu}$	$\text{Diff}_{P_{\infty, bu}}$
0.2	104191	104193	0.003		
0.3	107853	107859	0.005		
0.4	113135	113143	0.007		
0.5	120193	120204	0.009	120210	0.014
0.6	129240	129255	0.011	129255	0.011
0.7	140548	140561	0.009	140559	0.008
0.8	154454	154461	0.004	154461	0.004
0.9	171371	171375	0.002	171375	0.002

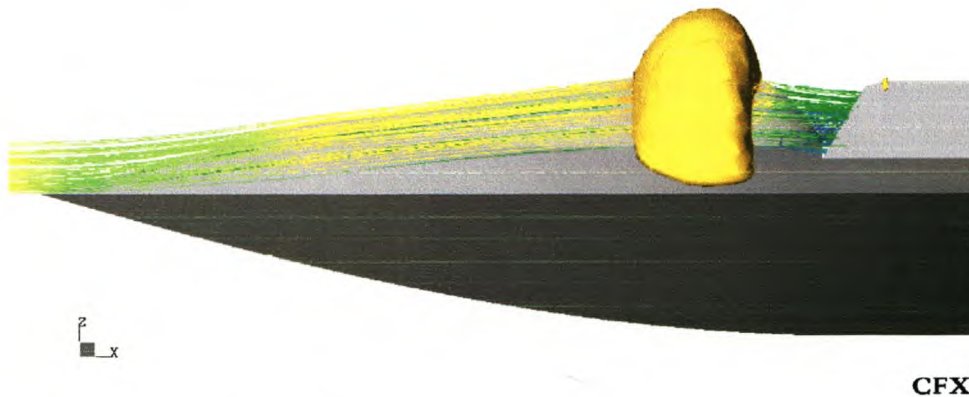
Table 5.4: Comparison between numerical and theoretical values for P_∞

M_∞	$q_{c,th}$	$q_{c,num,bd}$	Diff _{$q_{c,num,bd}$}	$q_{c,num,bu}$	Diff _{$q_{c,num,bu}$}
0.2	2559	2620	2.40		
0.3	2729	2736	0.26		
0.4	2906	2871	-1.21		
0.5	3217	3154	-1.98	3187	-0.94
0.6	3537	3428	-3.06	3481	-1.57
0.7	4006	3858	-3.69	3838	-4.18
0.8	4594	4512	-1.79	4486	-2.36
0.9	5344	5568	4.20	4881	-8.65

Table 5.5: Comparison between numerical and theoretical values for q_c

The software computes the total pressures using the same compressible-flow relations as were used to obtain the theoretical values, hence the negligible differences in table 5.4 [18, p.255].

The numerical values of q_c , at $M_\infty = 0.9$ are somewhat suspect, due to the magnitude of the differences when compared to those at $M_\infty = 0.2$ to $M_\infty = 0.8$. At this speed, there is quite a substantial region of supersonic flow where the fluid accelerates around the bump, shown as a yellow isosurface in figure 5.7.

Figure 5.7: $M_\infty = 0.9$: inlet streamtube and supersonic flow region

Transonic flow is difficult to solve numerically, since the nature of the equations change from elliptic in the subsonic region to hyperbolic in the supersonic region, but the location of this change is not known beforehand [19, Chapter 1]. This might contribute to the larger errors at $M_\infty = 0.9$.

Having validated the total and dynamic pressures, a comparison between the theoretically and numerically predicted inlet performance can now be drawn. Figure 5.8 shows $C_{\Delta P}$ as a function of M_∞ .

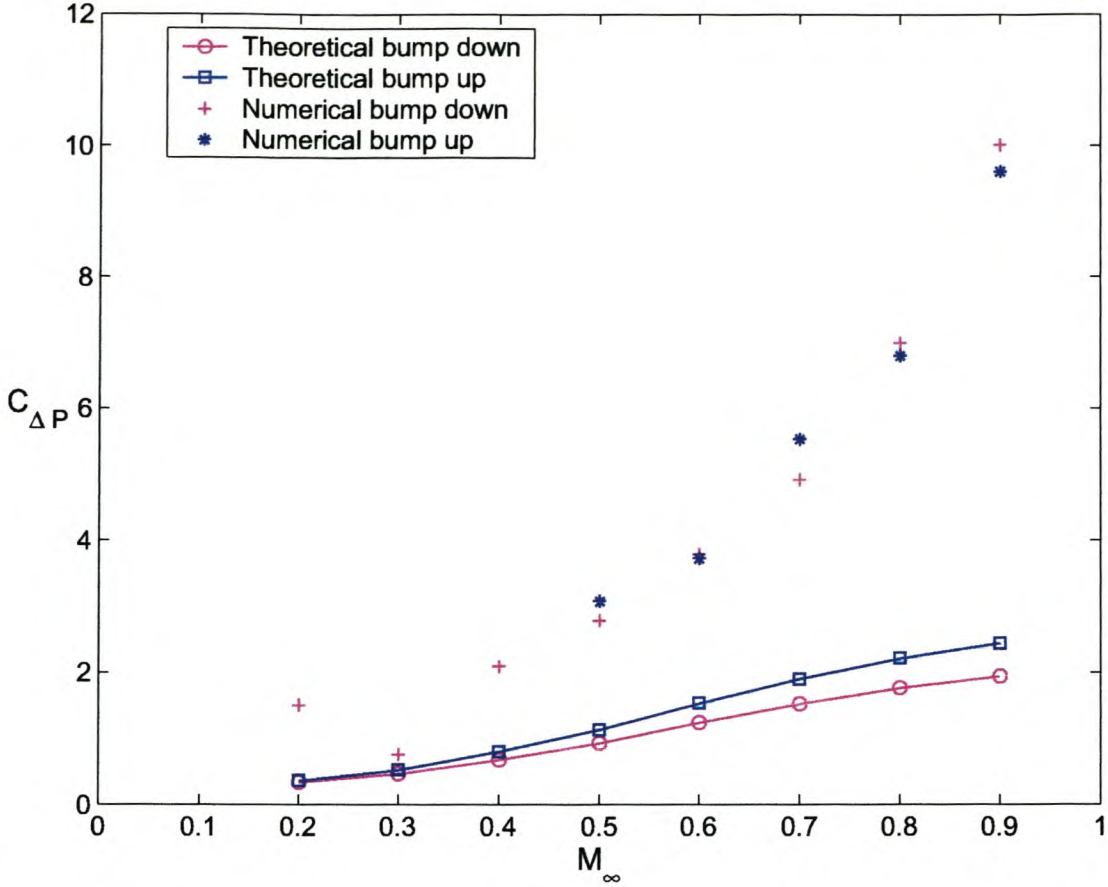


Figure 5.8: Comparison between theoretical and numerical predictions: $C_{\Delta P}$ vs. M_{∞}

As mentioned in section 5.3.1 the theoretical values for P_f can be computed from the corresponding values for $C_{\Delta P}$. This allows a theoretical prediction of the inlet pressure recovery η , which is of course the standard measure of inlet performance. The theoretical and numerical predictions of η are compared in figure 5.9.

It has to be reiterated that the theory of friction loss assumes that there is no flow separation ahead of the inlet, or inside the duct. The differences between the theory and the numerical values suggest that this is not the case. This is confirmed by plots of the velocity vectors on the bump and the walls of the inlet duct. The rest of this section will be devoted to examining the inlet flow, to clarify figures 5.8 and 5.9.

Bump down, $M_{\infty} = 0.2$

The velocity and total pressure profiles at the inlet face plane, in the downstream direction, are shown in figure 5.10. The profiles are symmetric about the vertical plane, with three lobes of higher velocity and pressure in the bottom, port and starboard quadrants, and lower in the top quadrant.

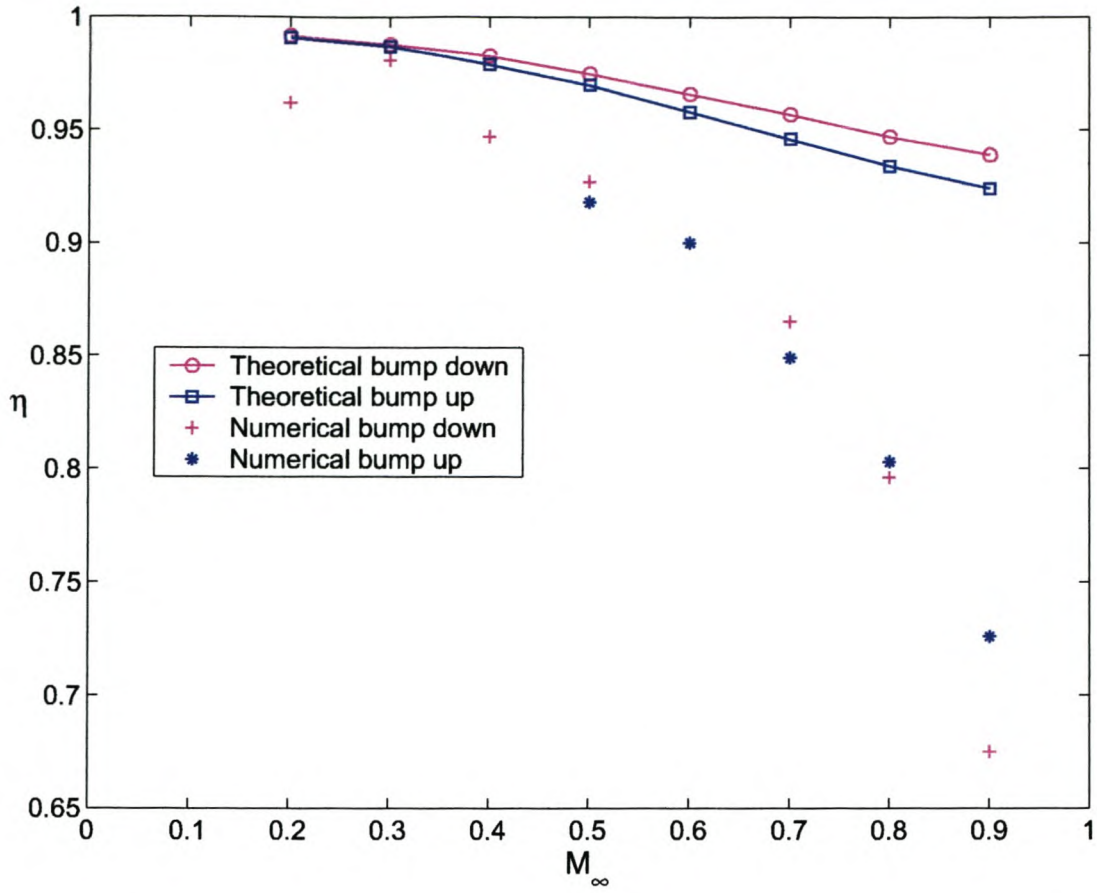


Figure 5.9: Comparison between theoretical and numerical predictions: η vs. M_∞

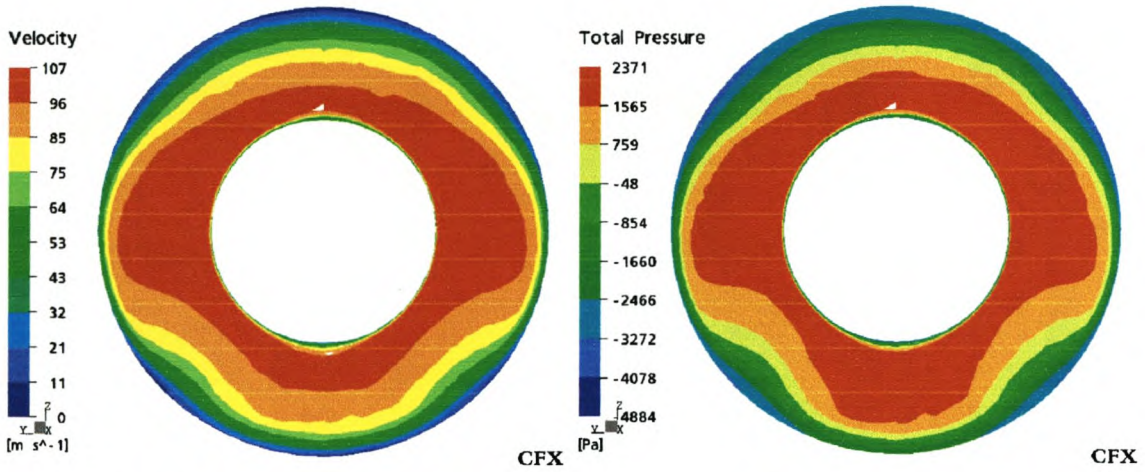


Figure 5.10: Engine face velocity and total pressure profiles, bump down, $M_\infty = 0.2$

A recirculation zone at the top of the inlet capture plane (see figure 5.11) is the probable cause of this lower velocity and total pressure. It is also responsible for the lower-than-expected

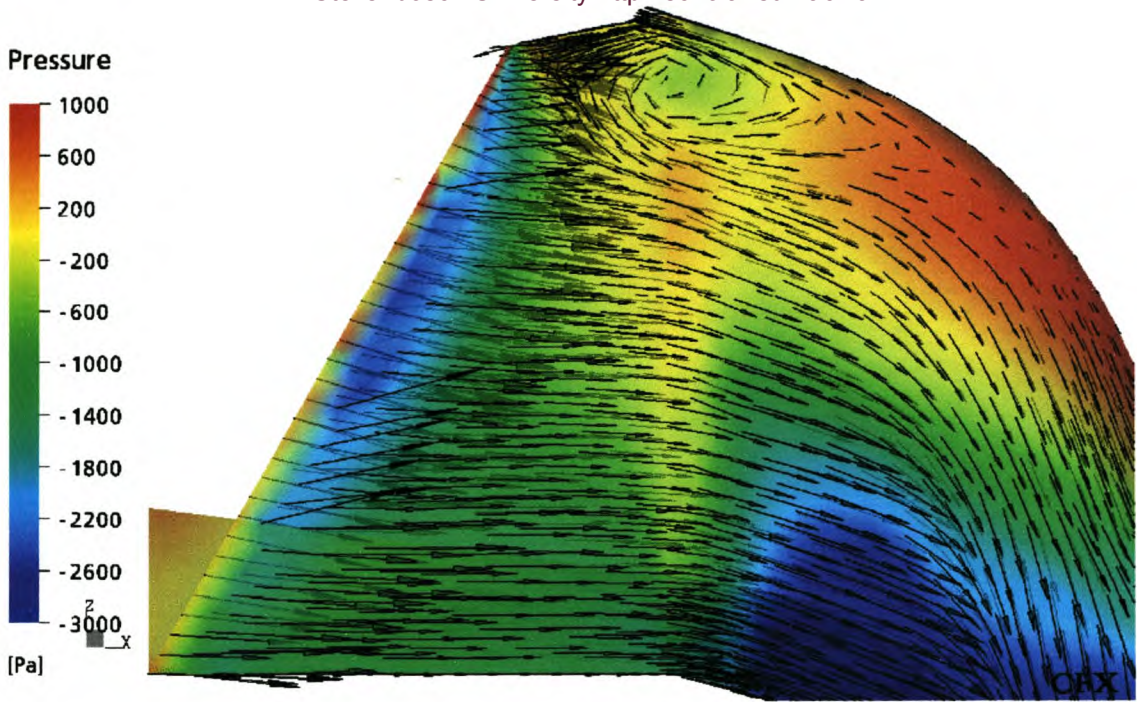


Figure 5.11: Velocity vectors in the inlet capture region, bump down, $M_\infty = 0.2$

pressure recovery at $M_\infty = 0.2$. The flow is smooth around the back of the bump, as seen in figure 5.12, and there is no separation in front of the inlet capture plane.

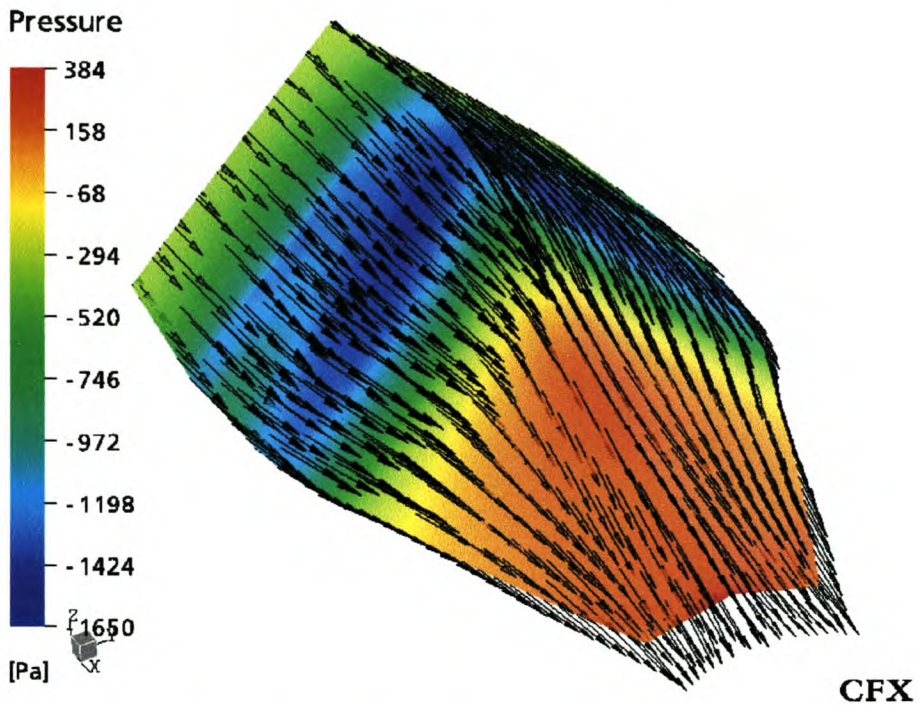


Figure 5.12: Velocity vectors around the bump, bump down, $M_\infty = 0.2$

Bump down, $M_\infty = 0.3$

The velocity and total pressure profiles are symmetric at the inlet face, as shown in figure 5.13. The side lobes of high variable values are less pronounced, and the region of high velocity and pressure in the top quadrant extend further in the radial direction than for $M_\infty = 0.2$. There is no separation in the inlet capture region, as shown in figure 5.14, and also none at the back of the bump (not shown). This is reflected in the relatively good correlation between the numerically and theoretically predicted pressure recoveries for this case.

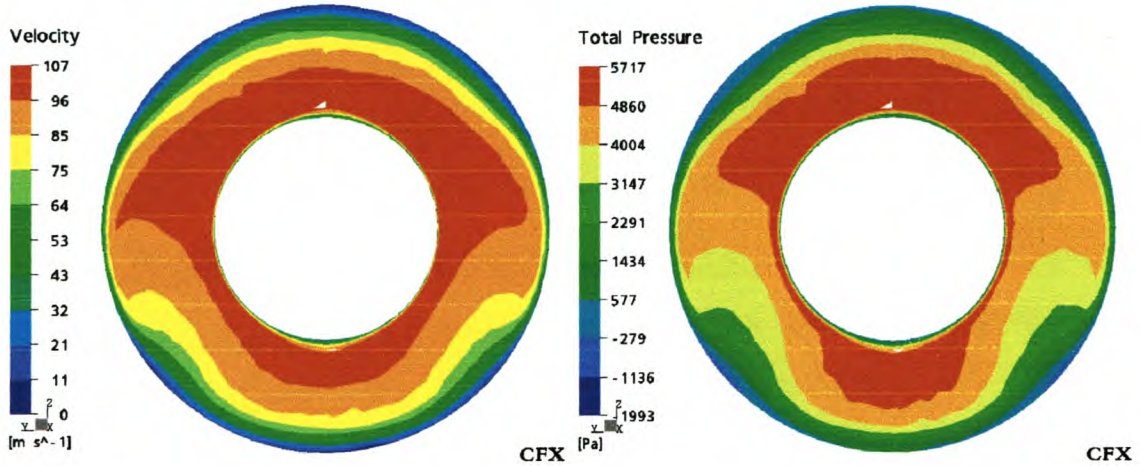


Figure 5.13: Engine face velocity and total pressure profiles, bump down, $M_\infty = 0.3$

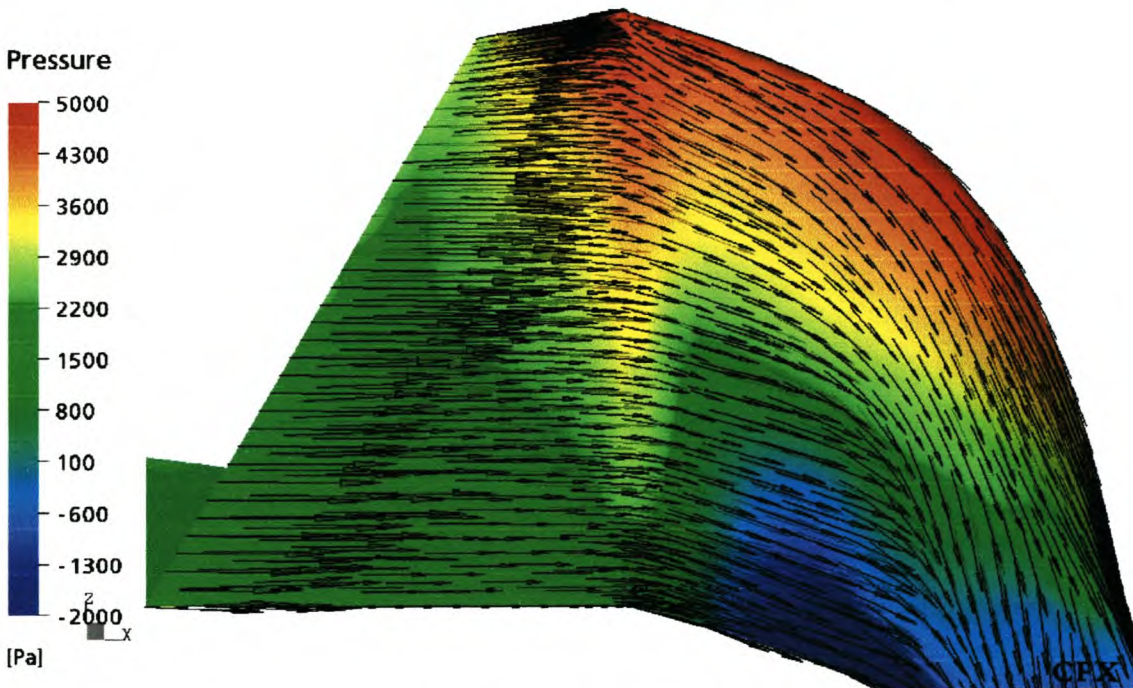


Figure 5.14: Velocity vectors in the inlet capture region, bump down, $M_\infty = 0.3$

Bump down, $M_\infty = 0.4$

The side lobes of high velocity and total pressure at the engine face have been replaced by a profile that is more uniform around the symmetry axis (see figure 5.15). The velocity vectors at the back of the bump and in the capture region of the inlet (figure 5.16) shows that the flow direction is no longer directly into the inlet, but that two small spiral nodes of separation have formed right in front of the inlet. These are responsible for the increased loss in total pressure at this flight Mach number. The flow is still steady, though, as can be seen in the symmetry of the velocity and total pressure profiles.

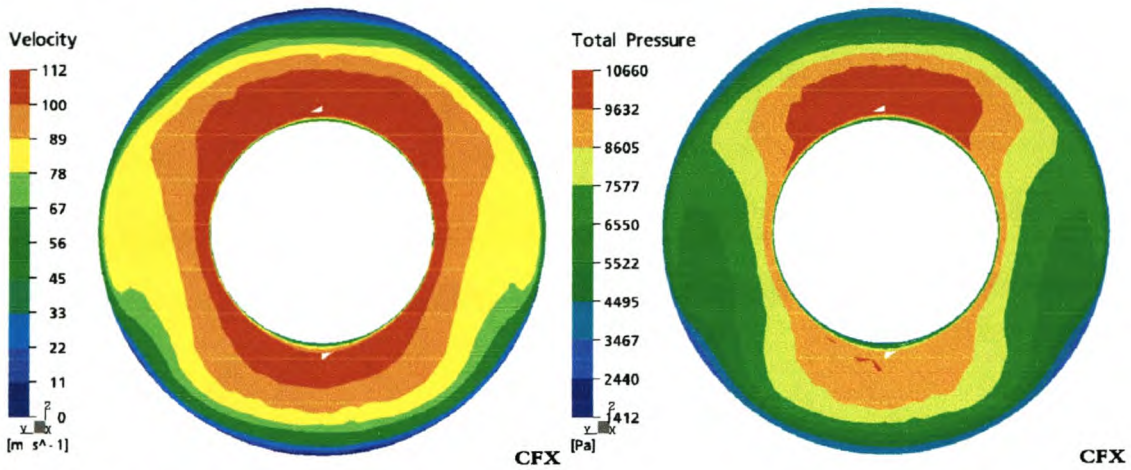


Figure 5.15: Engine face velocity and total pressure profiles, bump down, $M_\infty = 0.4$

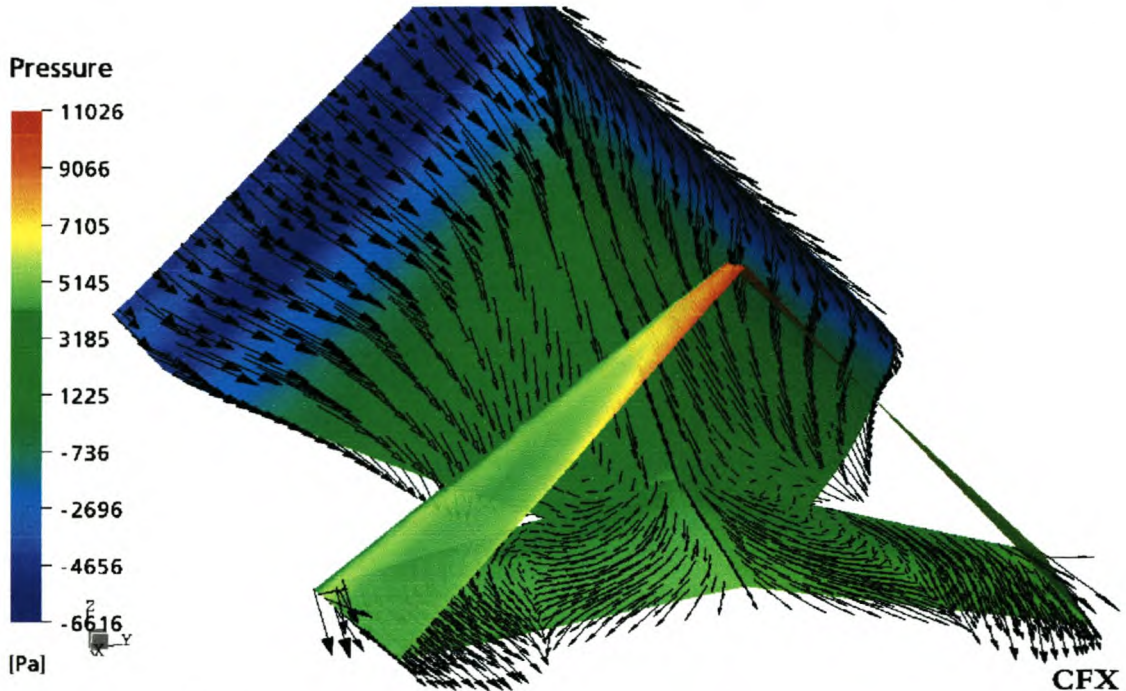


Figure 5.16: Velocity vectors flowing into the inlet, bump down, $M_\infty = 0.4$

Bump down, $M_\infty = 0.5$

Opposed to the symmetrical, separated flow at $M_\infty = 0.4$, the situation has become asymmetric at $M_\infty = 0.5$. This asymmetry – about the vertical plane – of the velocity and total pressure profiles at the engine face are shown in figure 5.17. It is also visible in the flow vectors in the inlet capture region, shown in figure 5.18. The spiral nodes of secondary flow have moved outward when compared to $M_\infty = 0.4$, and in the region between them the flow is asymmetric. The asymmetry might be due to the volume mesh not being wholly symmetric, or to vortex shedding from the back of the bump. This second option can only be confirmed by a transient simulation. The situation is similar at $M_\infty = 0.6$ and is not discussed separately.

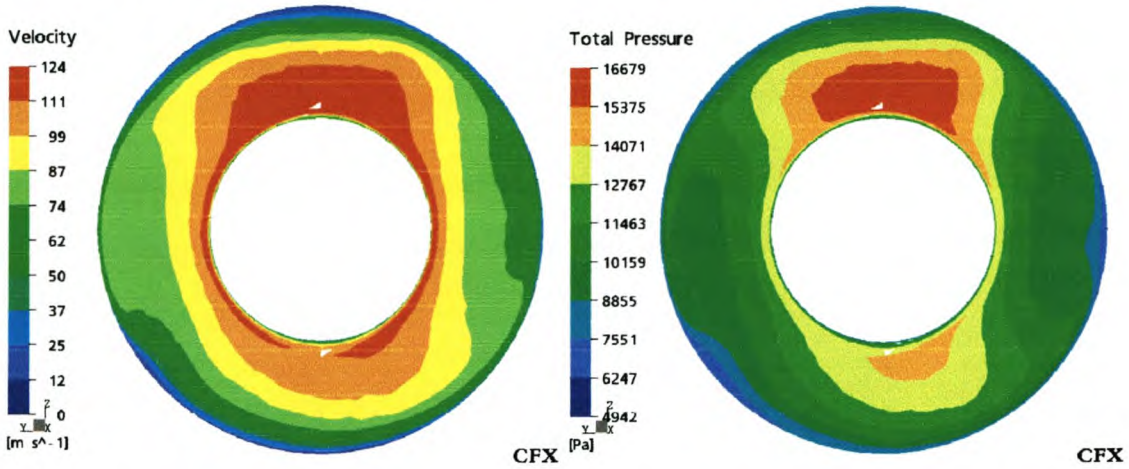


Figure 5.17: Engine face velocity and total pressure profiles, bump down, $M_\infty = 0.5$

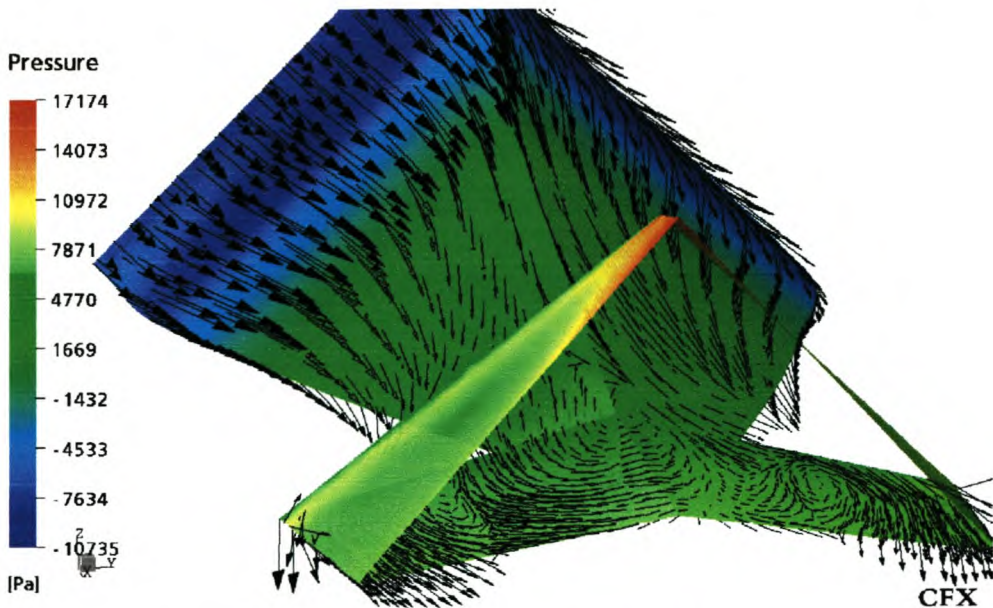


Figure 5.18: Velocity vectors flowing into the inlet, bump down, $M_\infty = 0.5$

Bump down, $M_\infty = 0.7$

Interestingly, where the flow was asymmetric at $M_\infty = 0.5$ and $M_\infty = 0.6$, it is symmetric at $M_\infty = 0.7$, reflected in the velocity and total pressure profiles at the engine face (figure 5.19). The flow into the inlet (figure 5.20) also shows the symmetry clearly. There is a sharply-defined line of separation at the back of the bump (where the pressure plot changes from orange to red). The effects of separation region visible as the relatively low velocities and total pressures in the bottom and side quadrants of the engine face.

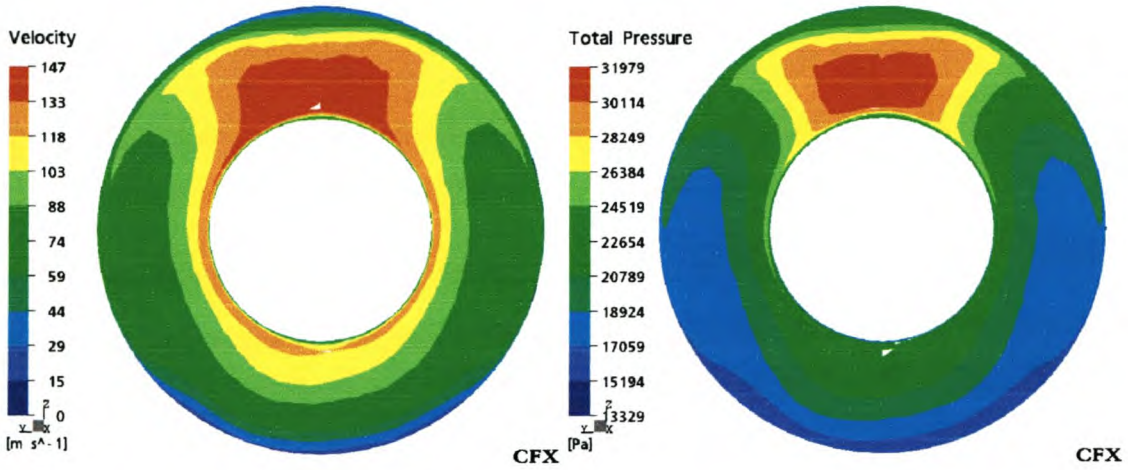


Figure 5.19: Engine face velocity and total pressure profiles, bump down, $M_\infty = 0.7$

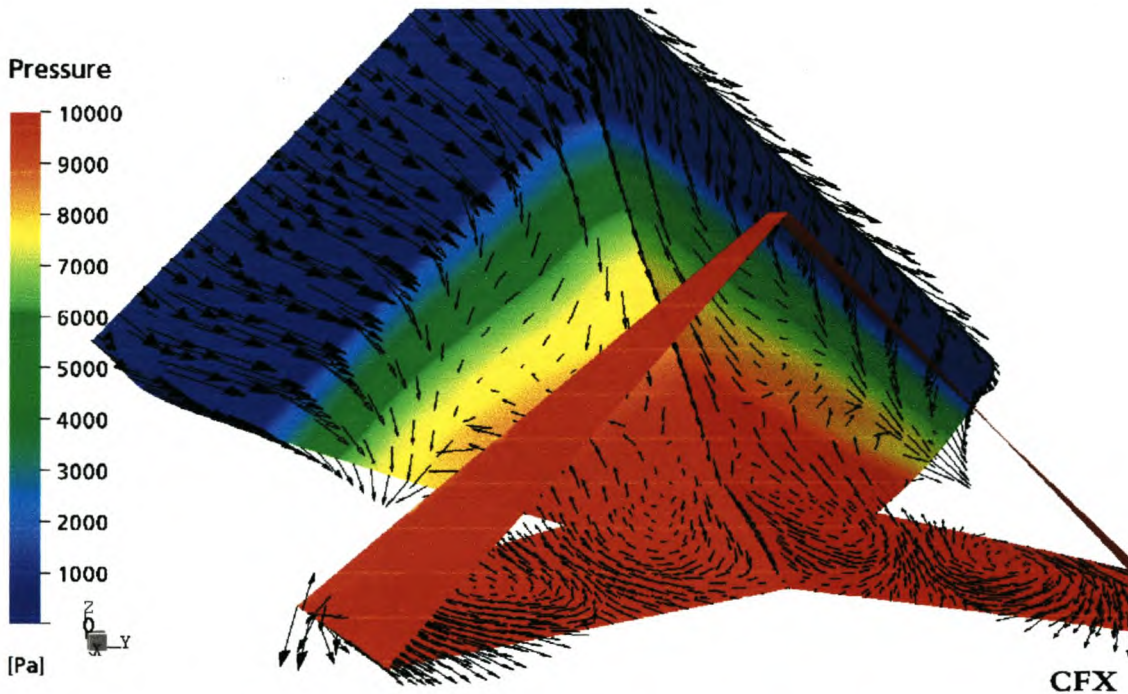


Figure 5.20: Velocity vectors flowing into the inlet, bump down, $M_\infty = 0.7$

Bump down, $M_\infty = 0.8$

The flow is once again asymmetric, as shown in figures 5.21 and 5.22. There is also an additional loss in due to a separation bubble at the top of the inlet capture plane (not shown here), similar to that at $M_\infty = 0.2$. This is the result of the flow entering the inlet more “from the top”, due to the displacement effect of the separation at the bottom of the inlet. The initial line of separation at the back of the bump has also moved further upstream. All these factors contribute to the sharply decreasing inlet performance at higher flight speeds.

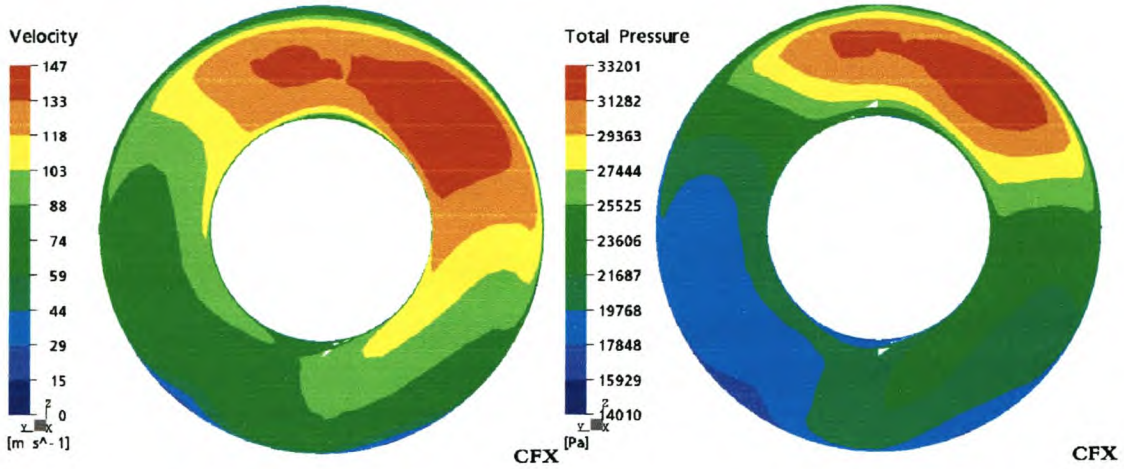


Figure 5.21: Engine face velocity and total pressure profiles, bump down, $M_\infty = 0.8$

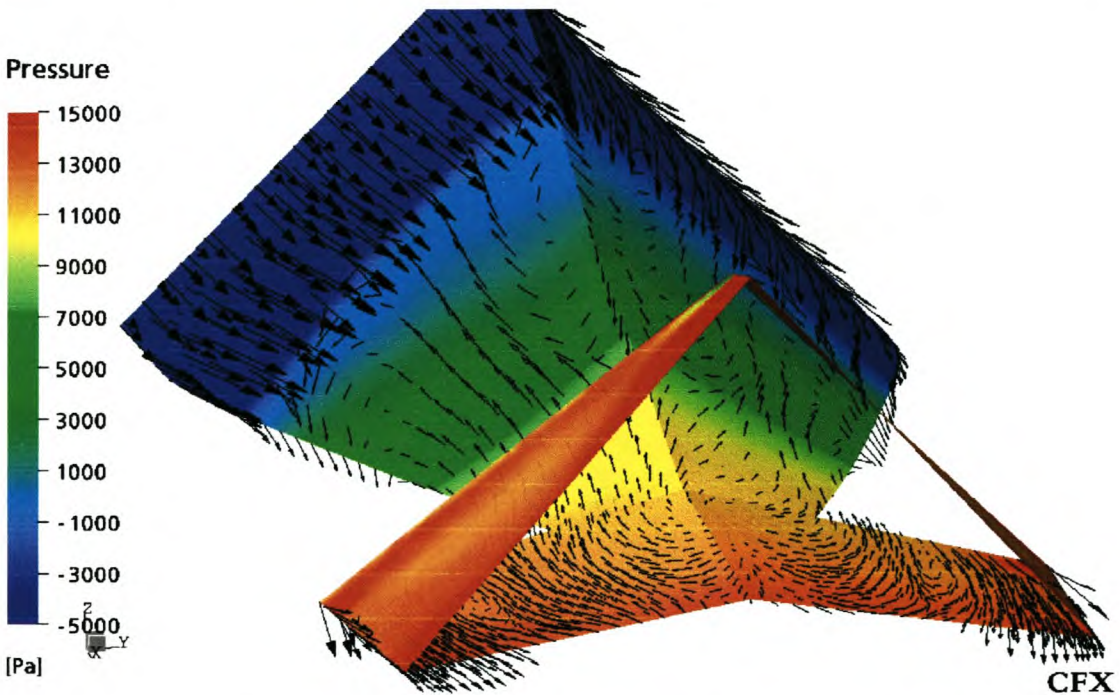


Figure 5.22: Velocity vectors flowing into the inlet, bump down, $M_\infty = 0.8$

Bump down, $M_\infty = 0.9$

The flow at $M_\infty = 0.9$ is generally similar to that at $M_\infty = 0.8$, with slightly less distortion of the velocity and total pressure profiles at the engine face. The profiles are still asymmetric, however. The separation bubble at the top of the inlet capture plane (figure 5.24) are larger than at $M_\infty = 0.8$, indicating even more separation in front of the inlet.

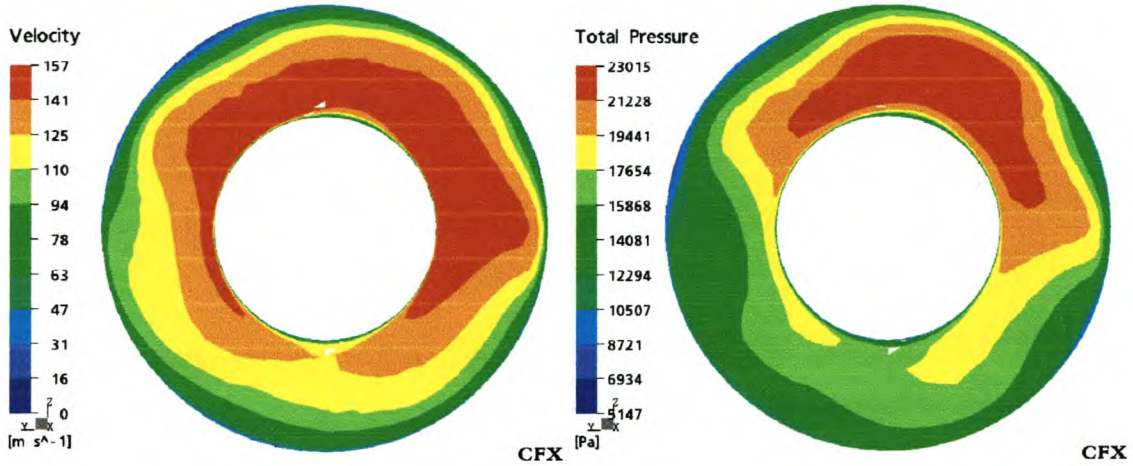


Figure 5.23: Engine face velocity and total pressure profiles, bump down, $M_\infty = 0.9$

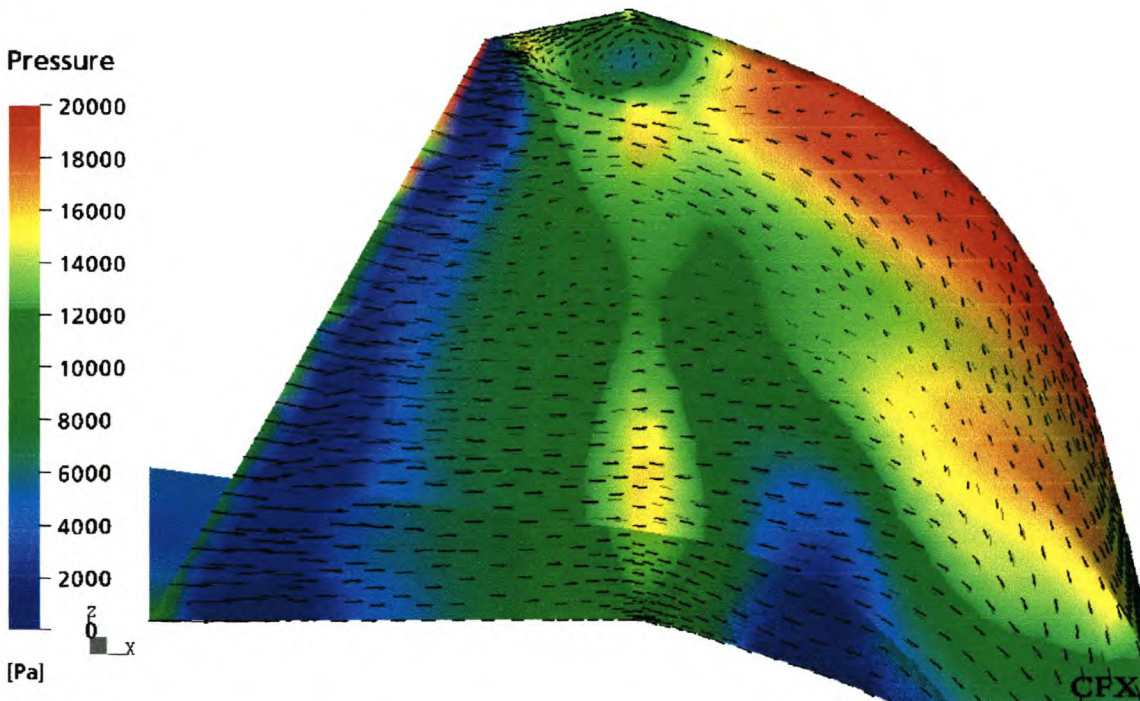


Figure 5.24: Velocity vectors in the inlet capture region, bump down, $M_\infty = 0.9$

Bump up, $M_\infty = 0.5$

In contrast to the bump down case at this speed, the flow in the bump up case is symmetric. The spiral nodes have moved inward (see figure 5.26) compared to the bump down case and there is a more definite line of separation at the back of the bump. There is a very small recirculation zone at the top of the inlet capture plane, which is not shown here. Its presence implies that the displacement effect due to flow separation at the back of the bump is larger in the bump up case than in the bump down case, for which similar separation only started at $M_\infty = 0.8$. This explains the lower pressure recovery in the bump up case.

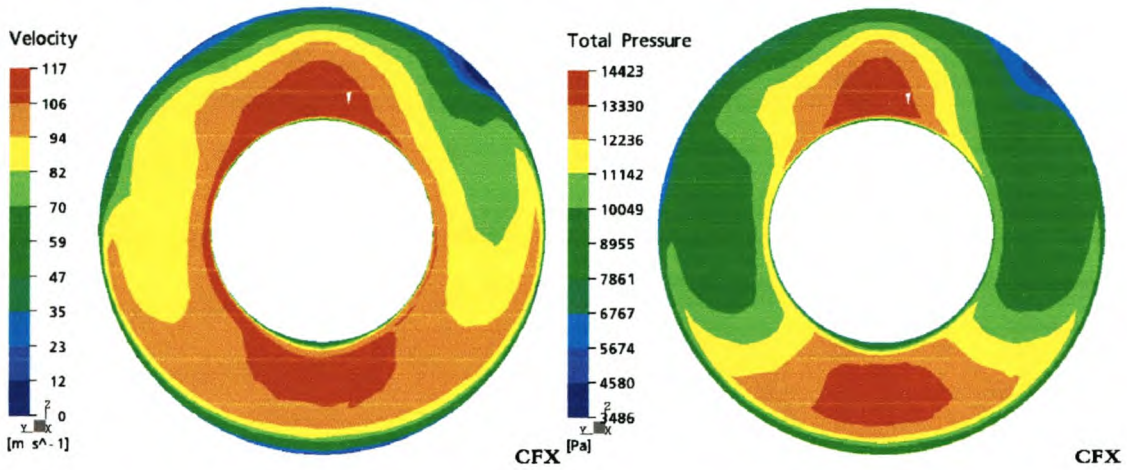


Figure 5.25: Engine face velocity and total pressure profiles, bump up, $M_\infty = 0.5$

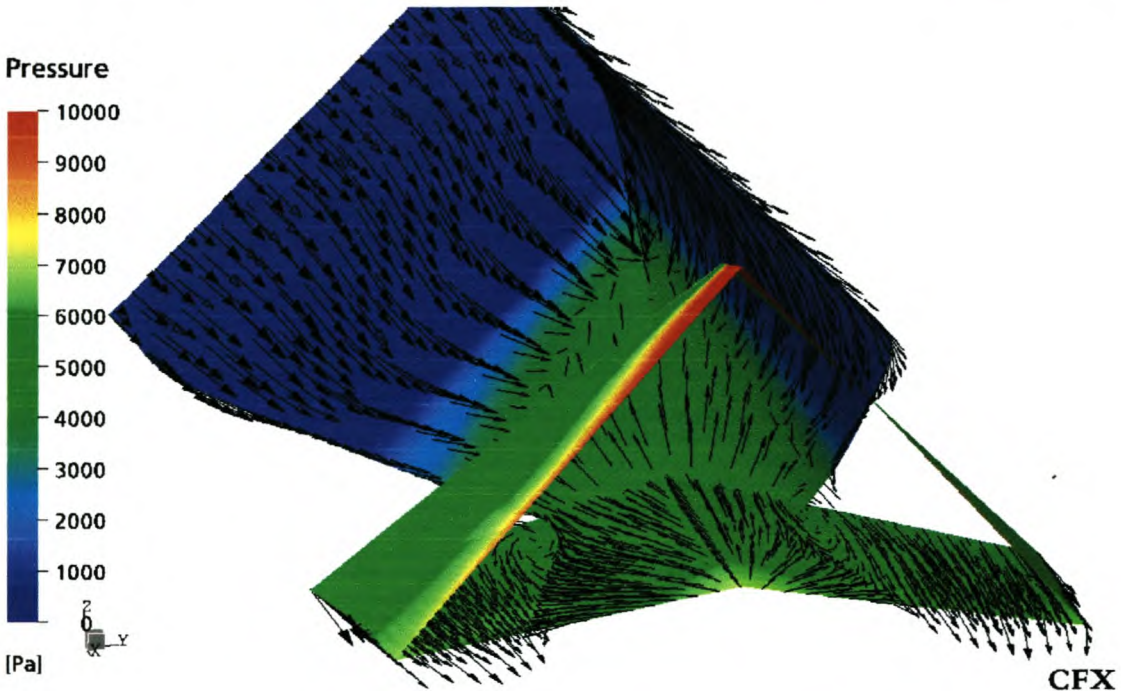


Figure 5.26: Velocity vectors flowing into the inlet, bump up, $M_\infty = 0.5$

Bump up, $M_\infty = 0.6$

The flow is asymmetric, but unlike the bump down case, the two spiral nodes of separation are not symmetric. Here the node on the left hand side is much bigger, and situated further to the back than the one on the right hand side, which is located just behind the bump (see figure 5.28). Also, on the line of separation at the back of the bump (where the pressure plot changes from green to yellow), the fluid moves across the ridge of the bump from the left hand side to the right hand side. The separation zone at the top of the inlet capture plane is also present. Interestingly the pressure recovery is not worse than for the bump down case (see figure 5.9).

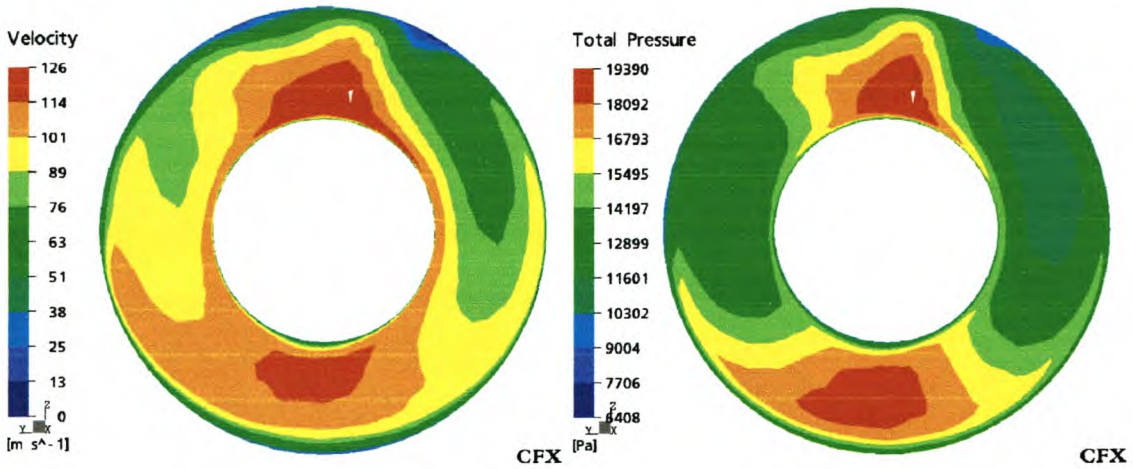


Figure 5.27: Engine face velocity and total pressure profiles, bump up, $M_\infty = 0.6$

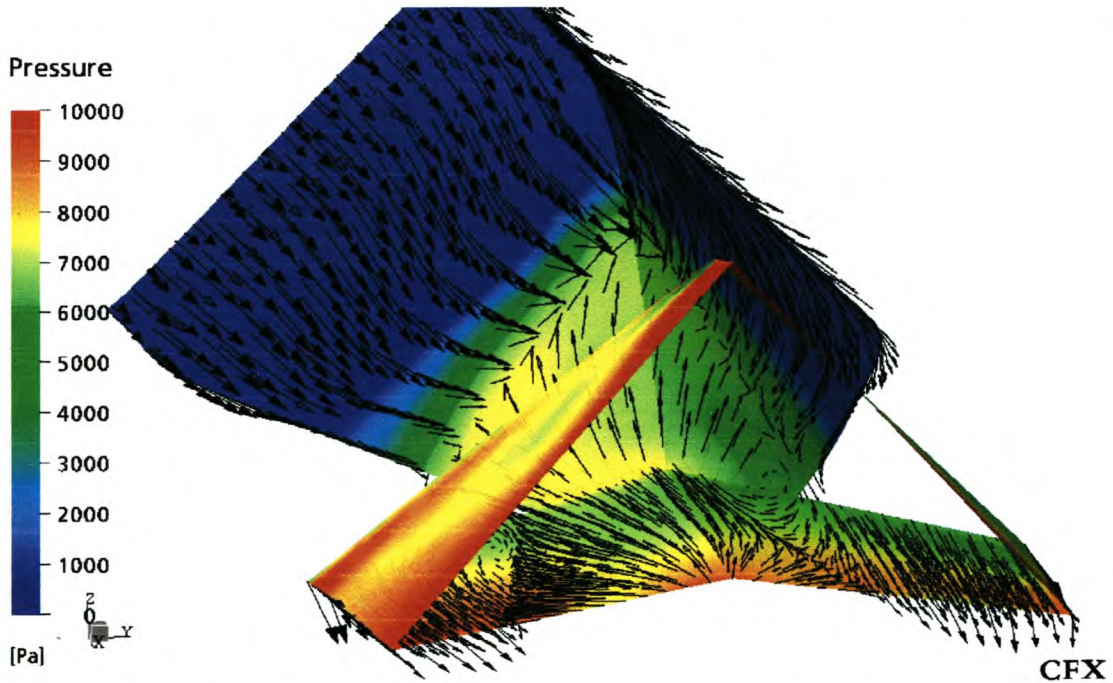


Figure 5.28: Velocity vectors flowing into the inlet, bump up, $M_\infty = 0.6$

Bump up, $M_\infty = 0.7$

The flow is very nearly symmetric, as for the bump down case at this speed. The reason for this deviation from the trend at $M_\infty = 0.7$ is not clear. The slight asymmetry in the engine face velocity and total pressure plots are due to some of the separated flow moving across the ridge of the bump as at $M_\infty = 0.6$. The lower pressure recovery of the bump up case compared to the bump down case can be attributed to the stronger separation and its associated displacement effect. Although not shown, the recirculation bubble at top of the inlet capture plane is stronger than at the lower flight speeds.

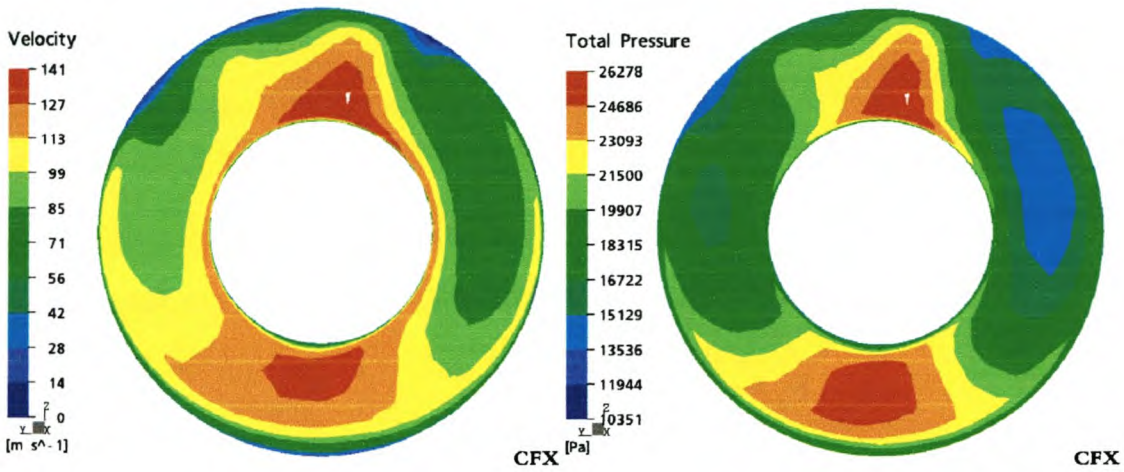


Figure 5.29: Engine face velocity and total pressure profiles, bump up, $M_\infty = 0.7$

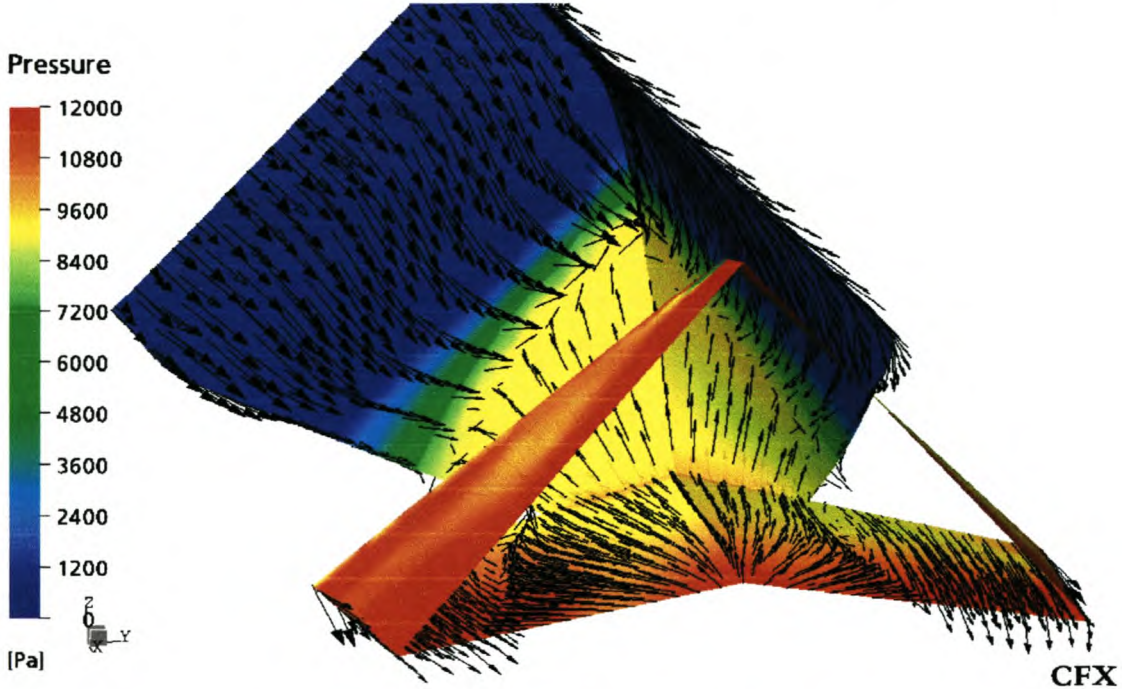


Figure 5.30: Velocity vectors flowing into the inlet, bump up, $M_\infty = 0.7$

Bump up, $M_\infty = 0.8$

As is evident in figure 5.31, the flow situation is strongly asymmetric, especially when compared to that at $M_\infty = 0.7$. All the mechanisms discussed so far contribute to a loss in pressure recovery for this case. The fact that the performance of the inlet is slightly higher than in the bump down case might be because the raised bump has a “stabilising” effect on the flow at higher speeds. This is however pure speculation that cannot be confirmed from steady-state analyses.

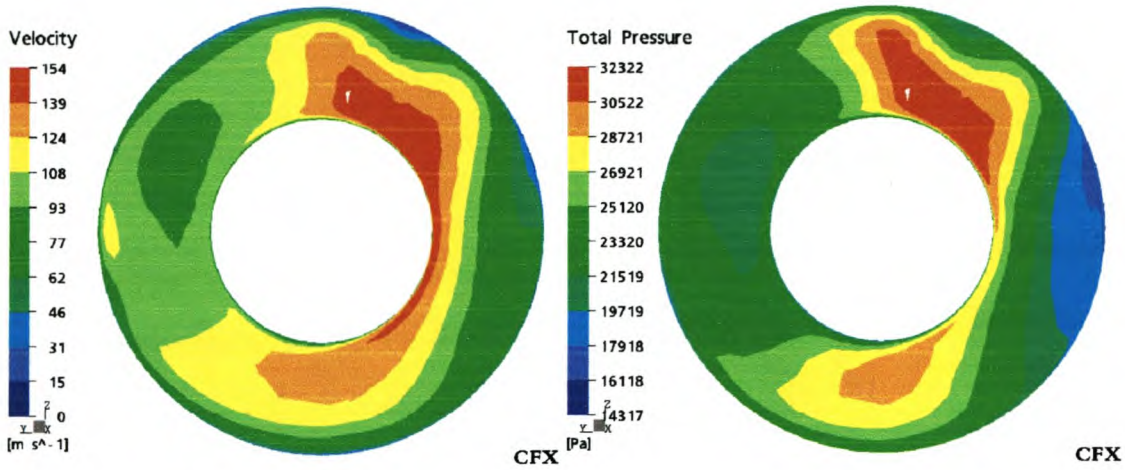


Figure 5.31: Engine face velocity and total pressure profiles, bump up, $M_\infty = 0.8$

Bump up, $M_\infty = 0.9$

The results exhibit features similar, but slightly more symmetric than that at $M_\infty = 0.8$. One feature of the bump up results which is very clear here, is the region of relative high total pressure and velocity values in the bottom quadrant of the profile (figure 5.32).

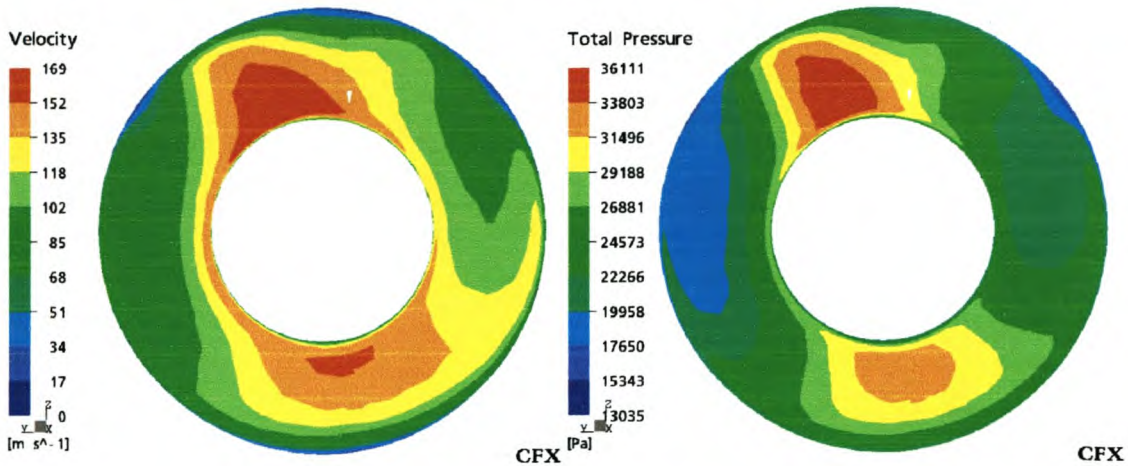


Figure 5.32: Engine face velocity and total pressure profiles, bump up, $M_\infty = 0.9$

5.3.3 Comparison between first and second-order designs

In order to quantify the differences between the two design iterations, the numerical model for the first-order design was adapted to include mesh inflation, and were subsequently run using the high resolution advection scheme. The pressure recoveries obtained from these simulations, compared to the results for the second-order design, are shown in figures 5.33 and 5.34.

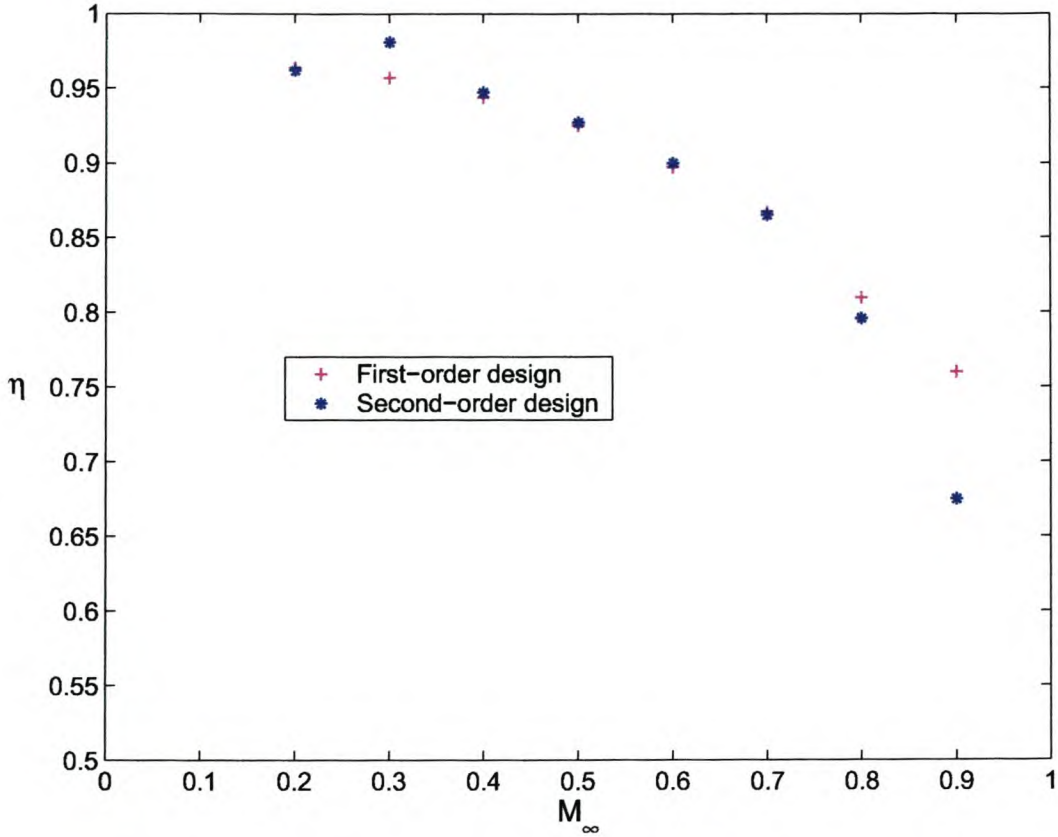


Figure 5.33: Comparison between first and second-order designs, bump down case

For the bump down case, the pressure recoveries are virtually identical for $M_\infty = 0.2$ and $0.4 \leq M_\infty \leq 0.7$. The second-order design performs significantly better at $M_\infty = 0.3$, while it also exhibits a more rapid loss in performance at $M_\infty = 0.8$ and $M_\infty = 0.9$. In the bump-up case, the second-order design performs better throughout most of the operating range. Although flow separation at the back of the bump was not avoided in the second-order design, its better performance in especially the bump-up case suggest that the goals of section 4.3.2 were at least partly achieved.

As further comparison, the distortion in the velocity profile at the engine face was quantified by calculating the kinetic energy correction factor, α , for each configuration at the different flight speeds. A larger value of α indicates a more distorted profile, while for an undistorted profile $\alpha = 1$.

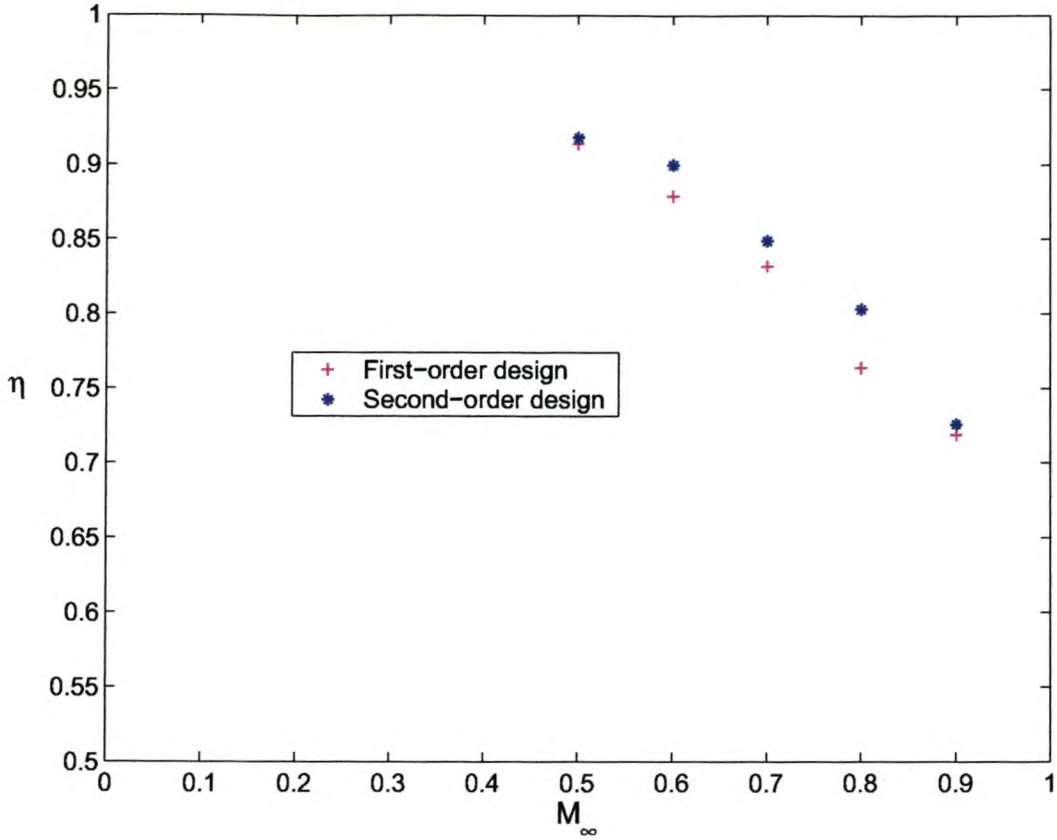


Figure 5.34: Comparison between first and second-order designs, bump up case

The value of α is calculated from

$$\int_f \left(\frac{1}{2} V^2 \right) \rho (\mathbf{V} \cdot \mathbf{n}) dA \equiv \alpha \left(\frac{1}{2} V_{ave}^2 \right) \dot{m} \quad (5.3)$$

as given in [12, section 3.6]. α is plotted against M_∞ in figures 5.35 and 5.36 for the bump down and bump up cases, respectively.

It is clear from both figure 5.35 and 5.36 that the velocity profiles at the engine face are significantly less distorted for the second-order design than for the first-order design. Only at $M_\infty = 0.9$ for the bump-down case is α_{1st} slightly lower than α_{2nd} . What is even more noticeable is that for both bump-down and bump-up configurations, α_{2nd} stays relatively constant across whole speed range, while α_{1st} varies significantly. It seems fair to assume that a constant level of distortion is more acceptable than one which varies with flight speed.

What is not immediately apparent from figures 5.35 and 5.36 is that there is slightly less distortion for the bump-up case of the second-order design than for the bump-down case. Coupled with pressure recoveries that are very similar (refer again to figure 5.9), this seem to

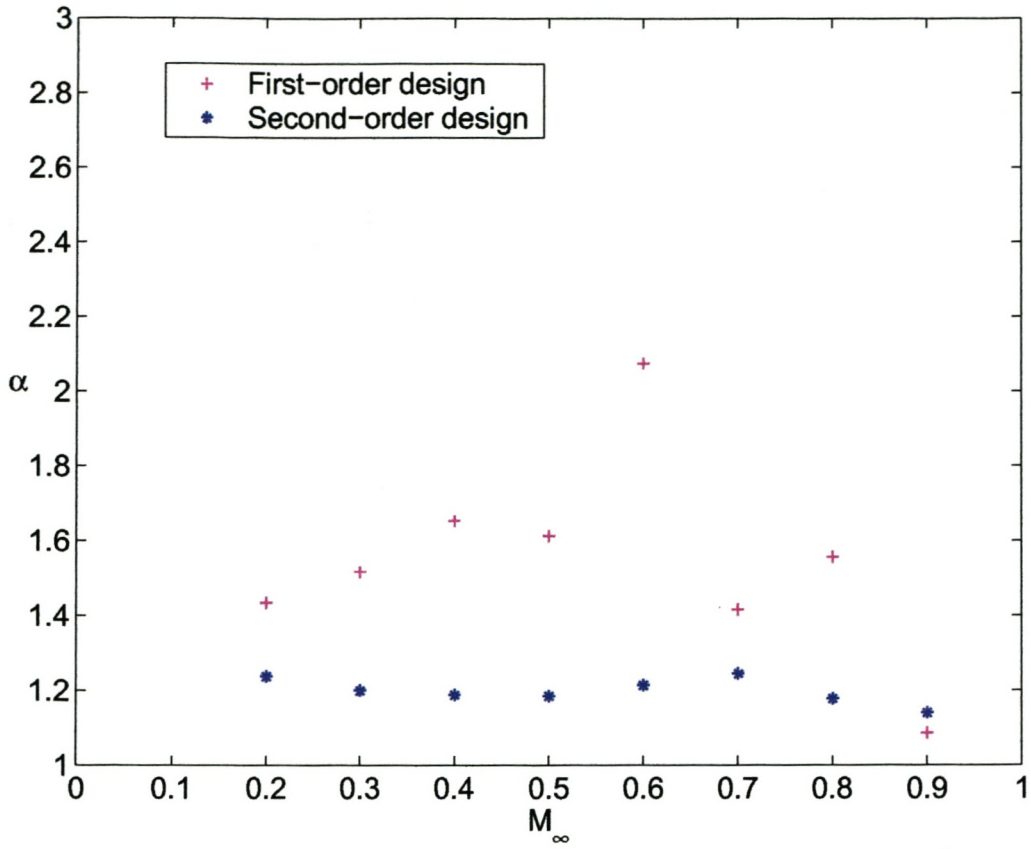


Figure 5.35: Kinetic energy correction factor, bump down

suggest that there are few (if any) aerodynamic advantages of the bump-down configuration over the bump-up configuration. This is discussed further in section 6.4.

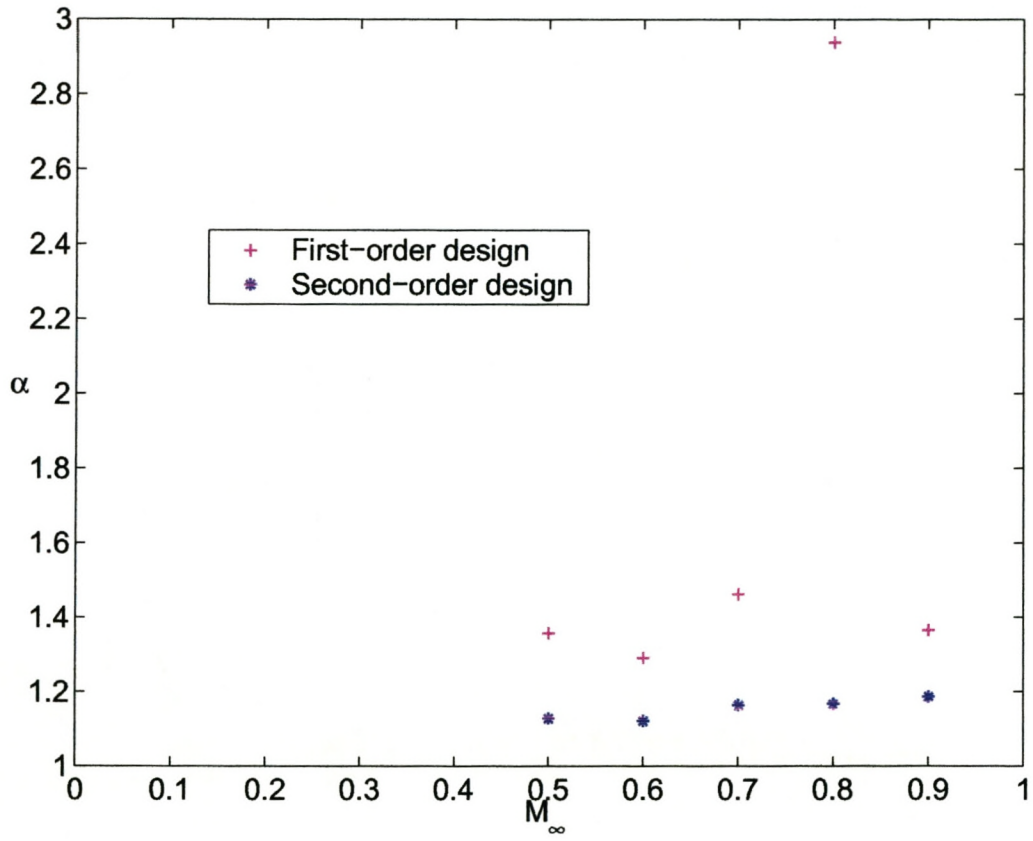


Figure 5.36: Kinetic energy correction factor, bump up

Chapter 6

Conclusion

6.1 Review of thesis objectives

The objectives for the thesis, as identified in section 1.5, are discussed here.

Firstly, the CFD software were validated for a number of flow scenarios with known results. These were similar to certain regions of flow on the conceptual model of the UCAV and its inlet. It was shown that the software returns results that compare well with those known beforehand from analysis or experiment, provided that the numerical model has been defined properly. The validation cases now form part of the knowledge base at the Department, allowing the simulation of similar cases using this software, without the need for an in-depth validation exercise.

Secondly, by constructing a CAD model of the UCAV, complete with inlet and duct, valuable experience was gained in building complex geometries using solid modelling CAD software. Importing of the geometry into CFX was accomplished through an intermediate file format (IGES).

Once the flow geometry was complete, the numerical model was completed by defining the computational mesh, applying physically consistent boundary conditions and specifying an appropriate turbulence model and advection scheme. These are all prerequisites to a numerical model that is consistent with the physical situation, ensuring that the simulation results represent the “real” flow as closely as possible.

In order to identify the variables which have to be examined to characterise the performance of the inlet, a proper understanding of the aerodynamics of subsonic air inlets was required. These variables were extracted from the raw numerical results, synthesised into a useful format and compared to an ideal theoretical model. The differences between the theoretical and numerical results were accounted for by visualisation of the flow into the inlet.

6.2 Recommendations for redesign of inlet

Although the focus of this thesis is not on the design of the inlet, but the numerical simulation thereof, it would be incomplete without suggestions of how the inlet performance can be improved.

The results discussed in section 5.3.2 shows that the major problem of the current design is flow separation in front of the inlet, especially at higher speeds. The bump down case at $M_\infty = 0.3$ has shown that when there is no separation, the numerical results are quite close to that predicted by the theory of friction loss. Therefore, the main aim of a subsequent design iteration should be to eliminate the separation ahead of the inlet capture plane.

The most probable cause of the separation is the interaction between the strong adverse pressure gradient ahead of the inlet and the fuselage boundary layer, as mentioned at the end of section 1.3. This aggravates the pre-entry retardation of the inlet streamtube and increases the probability of separation. Theoretically this effect can be reduced by either decreasing the strength of the adverse pressure gradient, or by reducing the boundary layer thickness. Because the position of the inlet is fixed, little can be done about the flow length into the inlet. Unless some form of active boundary layer control is employed, the boundary layer thickness is also fixed. Focus should therefore first be on relieving the adverse pressure gradient. Boundary layer control is discussed at the end of this section.

The pre-entry retardation is mostly due to the external diffusion of the streamtube from the free stream to the inlet capture plane (corresponding to situations where $\mu > 1$). While this process is 100% efficient for inlets with no wetted area on the approach, it has been shown in the previous paragraph that it can be disadvantageous when interacting with a fuselage boundary layer. Because the engine mass flow values are fixed at particular flight speeds, the free stream areas of the streamtube are also fixed, leaving the inlet capture area A_c as the only parameter to control the external diffusion with. By decreasing A_c (and therefore also μ), one should be able to arrive at a solution where there is little or no pre-entry separation at the main operating speeds of the aircraft ($M_\infty = 0.6$ to 0.8). It should be noted however that μ should still be larger than unity at these speeds, to avoid separation on the inside of the inlet lips, as explained in section 1.3. The equation for the theory of friction loss (equation 1.3), shows that $C_{\Delta P}$ depends on μ^3 , and hence the theoretical pressure recovery would increase as μ is decreased.

Care should be taken, however, since the flow in the duct is strongly dependent on the magnitude of A_c . To avoid separation inside the duct, it had a decreasing cross section up to the second bend. This ensures a favourable pressure gradient, keeping the flow attached through the sharp curves (the design of the duct is explained in more detail in section A.7.2). None of the simulations showed separation inside the duct, and it is recommended that this

initial decrease in cross section is retained.

In addition to decreasing A_c , a diverter can be used to prevent the inlet from ingesting the boundary layer. As an alternative to the passive system, some form of active boundary layer control can be used to either remove or re-energise the fuselage boundary layer. This can respectively be done by suction normal to the flow, or blowing in the flow direction. It has to be stressed, however, that correcting the bulk flow properties should take precedence, in order to obtain the best possible solution *before* boundary layer control is used to correct “trouble spots”.

6.3 General conclusions

The work done in this thesis demonstrated that CFD can be used effectively in the conceptual design process of an aircraft to test the aerodynamic viability of a certain design, *provided* that the simulations mirror the actual situation. One should be careful to not read too much into first-order simulations such as those in chapter 4, for instance. It should also always be kept in mind that even the “best” CFD model is still only a model. Especially in a design situation, it should not be seen as a complete substitute for experimental work.

6.4 Recommendations for further work

1. An accurate model of the inlet duct can be constructed, and experiments conducted to determine its flow characteristics. This could serve as further validation of the numerical model.
2. A model of the external geometry can be manufactured and tested in the wind tunnel, once again as validation for the numerical model.
3. The current geometry can be subjected to transient flow CFD simulations to quantify the influence of the asymmetry in the flow on the performance of the inlet more accurately.
4. A design revised according to the recommendations in section 6.2 can be simulated to test the validity of the alterations.
5. Simulations at different angles of attack should be conducted to determine how much the fuselage interferes with flow into the inlet. This is especially important during maneuvering of the aircraft.
6. In light of the similar performances of the bump-down and bump-up configurations, as shown in figures 5.9, 5.35 and 5.36, a study should be done to determine whether the added

complexity of raising and lowering the back of the bump is justified. A trade-off study between variable and fixed geometries is therefore recommended. Should a fixed geometry be decided upon, CFD can again be used to determine the optimal configuration.

6.5 Closure

As a final note, the validity of this particular inlet concept is illustrated by the Boeing Bird of Prey manned research aircraft (see figure 6.1) which was declassified in October 2002.



Figure 6.1: Boeing Bird of Prey [20]

The inlet configuration of the Bird of Prey suggests that a similar design methodology was used as for the UCAV inlet that was examined in this thesis. The canopy is particularly similar to the bump of the UCAV inlet, as is the geometry of the inlet lips. Relative to the canopy, the inlet entrance is much smaller than that of the UCAV inlet is relative to the bump. This substantiates the suggestions of reducing A_c on the current design.

Appendix A

Details of conceptual UCAV and preliminary inlet design

A.1 Background

The focus of this thesis was on the numerical simulation of a generic, mission adaptive inlet for a stealthy UCAV. Typical mission profiles and geometric guidelines for such a UCAV were obtained from Kentron Dynamics¹. They also supplied the characteristics of a small gas turbine engine. Within this framework a design for the inlet could then be developed. The airframe guidelines and engine characteristics formed the constraints from which engineering specifications were developed.

A.2 Mission profiles

Three possible airframe mission profiles were identified. Each of these consists of ingress, mission and egress phases, with a specified speed and altitude range in each phase, as well as the most probable threats that may be expected. These mission profiles are summarised in Table A.1.

A.3 Airframe geometry

Figure A.1 shows the basic airframe geometry that was suggested for a generic stealthy UCAV.

Of note is the high leading edge sweep angle, intended to reflect incident radar energy well away from the receiver (see section 1.2). This high sweep angle is however not optimal from an aerodynamic viewpoint, considering the subsonic operating envelope of the aircraft. This again demonstrates the contradiction between stealth and aerodynamics requirements.

¹Kentron Dynamics, P.O. Box 7412, Centurion, 0046

Mission Profile	Performance parameters	Ingress phase	Mission phase	Egress phase
High-Low-High	Speed range Altitude Primary threats	M = 0.5-0.7 12000-14000 [m] High altitude radar guided SAM's; Fighter aircraft with guns and AAM's	M = 0.7-0.9 60-300 [m] IR guided missiles, Radar-assisted AA-guns	M = 0.5-0.7 12000-14000 [m] High altitude radar guided SAM's; Fighter aircraft with guns and AAM's
High-High-High	Speed range Altitude Primary threats	M = 0.5-0.7 12000-14000 [m] High altitude radar guided SAM's; Fighter aircraft with guns and AAM's	M = 0.7-0.9 12000-14000 [m] High altitude radar guided SAM's; Fighter aircraft with guns and AAM's	M = 0.5-0.7 12000-14000 [m] High altitude radar guided SAM's; Fighter aircraft with guns and AAM's
Low-Low-Low	Speed range Altitude Primary threats	M = 0.5-0.7 60-300 [m] IR guided missiles, Radar-assisted AA-guns	M = 0.7-0.9 60-300 [m] IR guided missiles, Radar-assisted AA-guns	M = 0.5-0.7 60-300 [m] IR guided missiles, Radar-assisted AA-guns

Table A.1: Airframe performance matrix

A.4 Engine

The engine that was prescribed is the Microturbo TRI 60-5 turbojet, shown in Figure A.2. The TRI 60 family of engines are designed for the propulsion of target drones and tactical missiles and covers a wide thrust range. These engines can be started by compressed air or by windmilling when launched from an aircraft or following a static, booster-assisted launch from ground, ship or helicopter [21].

A program, based on a lookup table of the characteristic curves of the engine, was also supplied by Kentron Dynamics. This program computes (among other parameters) the mass flow through the engine as function of flight altitude (z), free stream Mach number (M_∞) and inlet pressure recovery (η) defined by equation 1.1 and repeated here for convenience.

$$\eta = \frac{P_f}{P_\infty} \quad (\text{A.1})$$

To obtain a first approximation of the expected mass flow, a pressure recovery of 1 was assumed. Subsequently, the engine mass flow at altitudes from sea level to 12000 [m], and flight Mach numbers from 0.2 to 0.9 were calculated. The results are presented in figure A.3,

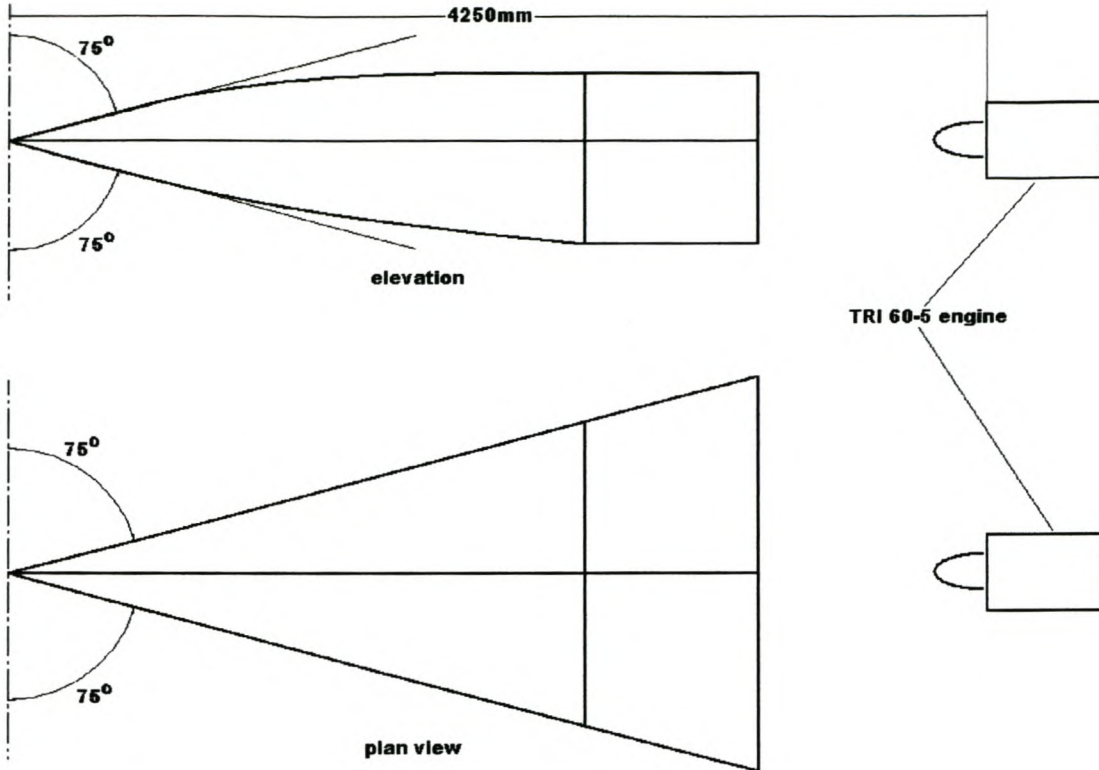


Figure A.1: Geometric layout of conceptual UCAV

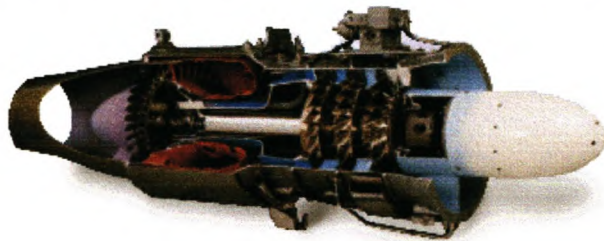


Figure A.2: Microturbo TRI 60-5 [21]

from which it can be seen that the mass flow ideally varies between approximately 1.7 [kg/s] and 8.8 [kg/s]. The maximum mass flow through the engine cannot exceed 6.5 [kg/s], however, shown by the horizontal limit line. The operating envelope of the engine is therefore defined by the combinations of altitude and Mach number for which the mass flow is less than the maximum.

With the mass flow known, the area of the streamtube captured by the inlet is determined from the definition of mass flow rate:

$$A_{\infty} = \frac{\dot{m}}{\rho_0 \cdot V} \quad (\text{A.2})$$

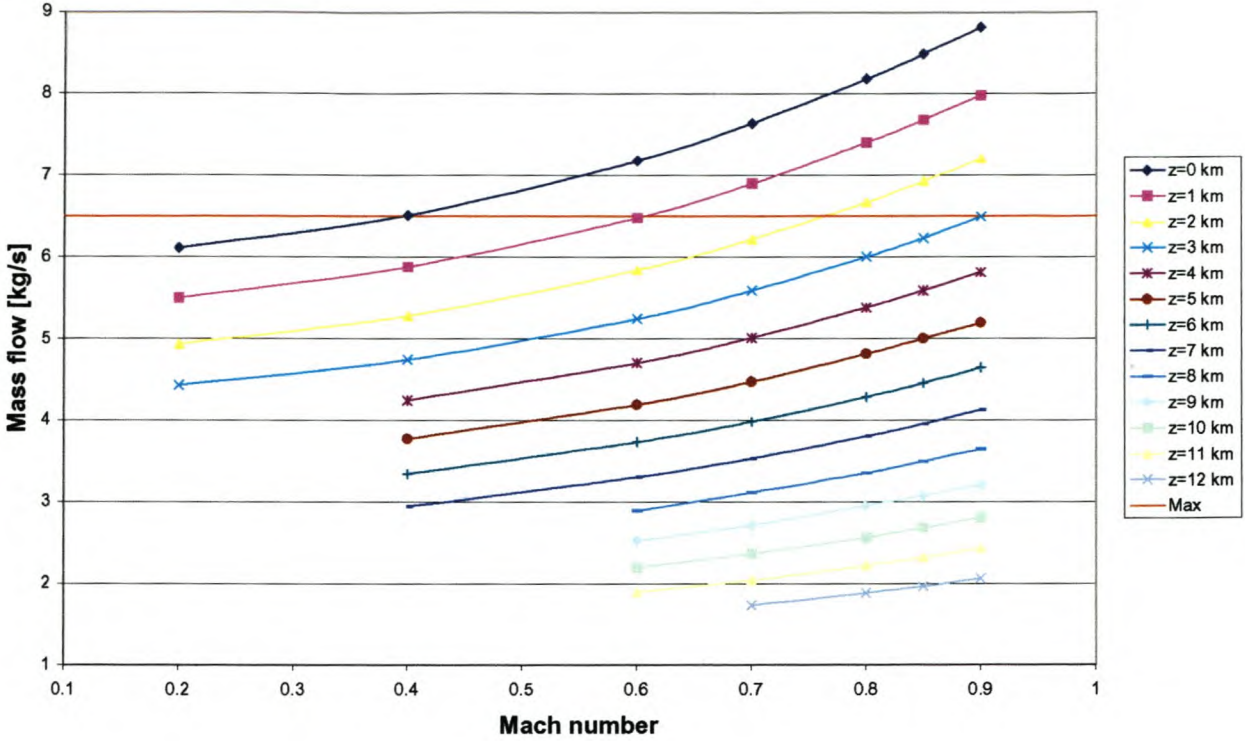


Figure A.3: Inlet mass flow

where the speed is obtained from

$$V = M_{\infty} \cdot c \quad (\text{A.3})$$

with

$$c = \sqrt{\gamma \cdot R \cdot T_0} \quad (\text{A.4})$$

From Figure A.4 it can be seen that the captured streamtube area (A_{∞}) varies between approximately 0.02 [m²] and 0.075 [m²] and that it is only a function of the freestream Mach number. The engine face area, shown by the red line, is the maximum exit area of the inlet duct, which determines the flow velocity seen by the compressor. Using the isentropic flow properties for steady compressible flow [22, Table A.1], it can be shown that for an ideal diffuser with inlet area equal to the streamtube area, and exit area equal to the engine face area, the Mach number at the exit of the duct stays approximately constant at 0.2.

It must be emphasised that the calculations of mass flow, and streamtube area are for a diffuser with 100% efficiency. In practice a lower efficiency and therefore higher Mach number at the engine face is to be expected.

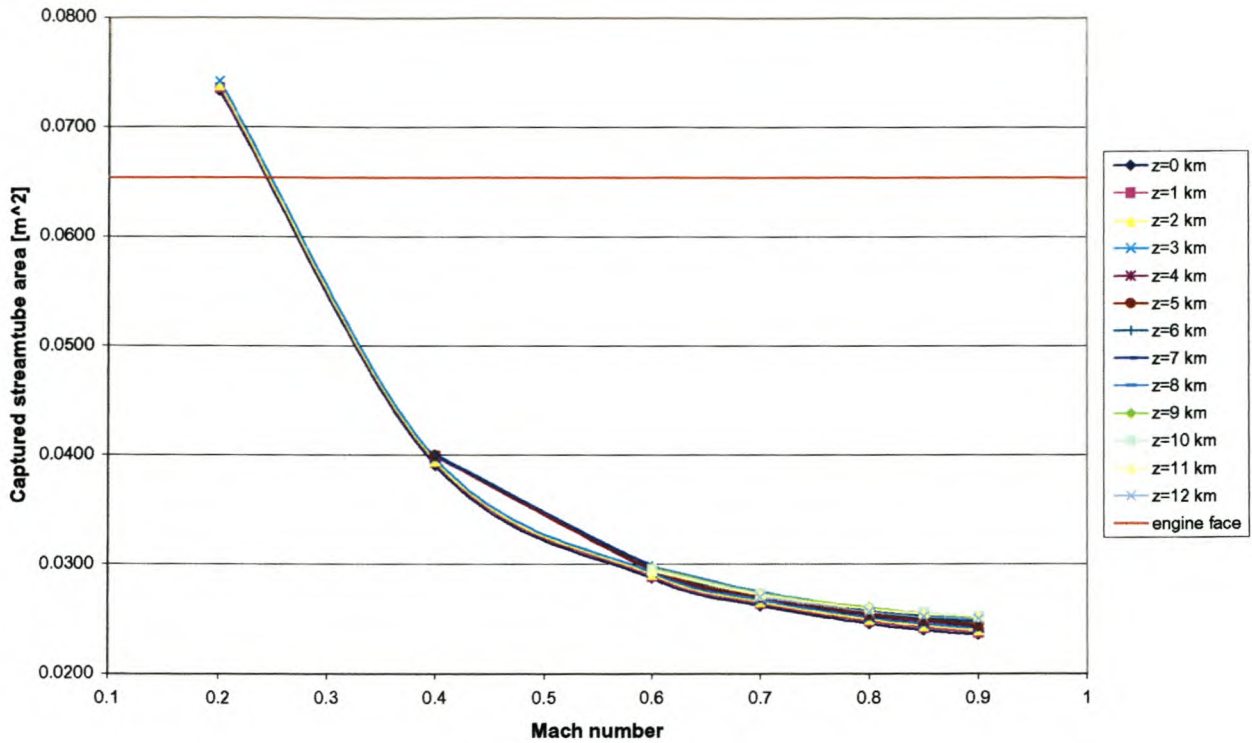


Figure A.4: Captured streamtube areas

A.5 Design specifications

The allowable physical dimensions of the inlet system are specified in figure A.5. Note that this is an unmodified copy of a picture directly obtained from Kentron.

The specifications for the inlet can be divided into aerodynamic requirements and stealth requirements. With the basic assumption in mind that engine is supplied with sufficient air to generate the required thrust, the aerodynamic requirements are that:

- diffusion should take place with the fewest losses, to recover as much of the dynamic pressure as possible.
- the velocity and total pressure profiles at the engine face should be as uniform as possible.
- external flow around the inlet should not interfere with control surfaces.

As specified in figure A.5, a major compromise in the aerodynamic design is that no external boundary layer separation plate is allowed. This is to minimise reflective edges, in line with the overriding stealth requirements, which are simply that the inlet RCS should be low as possible to avoid detection in a specific threat environment.

The aerodynamic and stealth requirements were consolidated by the additional specification that some form of variable geometry should be employed whereby the inlet can be varied

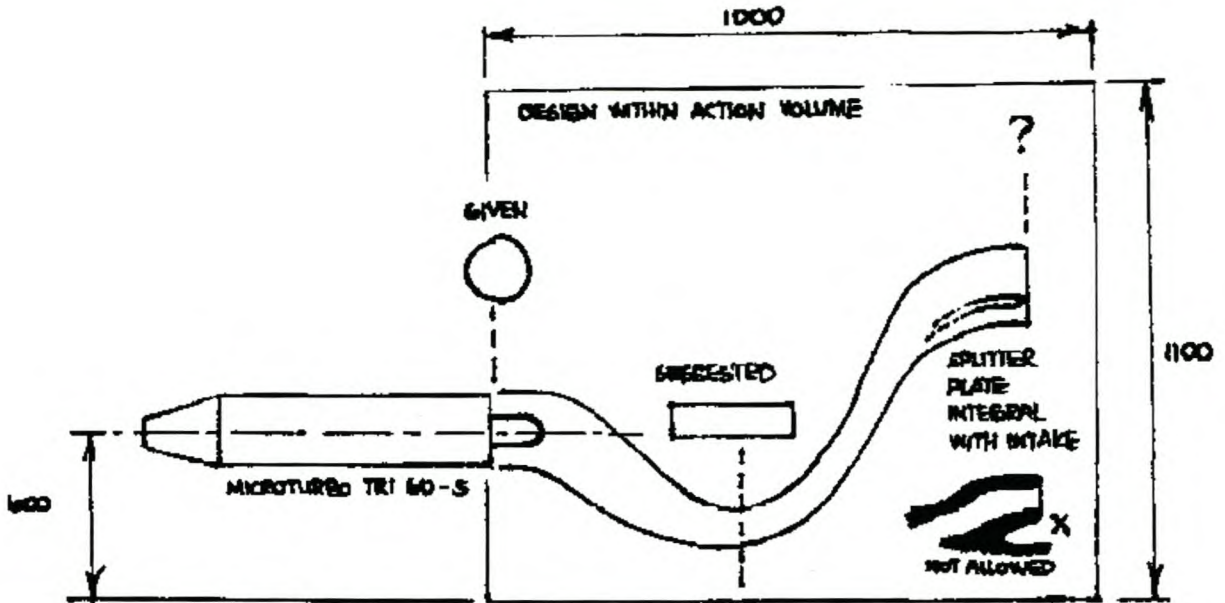


Figure A.5: Specified action volume [?]

between one with higher aerodynamic efficiency (and higher RCS) to one with lower RCS (and lower aerodynamic efficiency).

A.6 Preliminary concept design

Four different conceptual designs were generated to satisfy the specifications in section A.5, and after their evaluation, the concept shown in Figure A.6 was chosen. The main characteristic of this concept is that it is situated on top of the airframe, but sunken, so that the front part of the fuselage forms a “bump” that shields the inlet lips from incident radar energy.

A.7 Detailed design

A.7.1 External inlet configuration

As the design progressed, the variable geometry specification was satisfied by allowing the rear part of the bump to be raised for increased shielding of the inlet during high-threat flight phases, or lowered for higher aerodynamic efficiency during low-treat phases.

Due to the high wing sweep angle, aligning the inlet lip edges parallel to the wing leading edge would have led to large inlet sweep and rake angles (see Figure 1.4). This would have negatively influenced the aerodynamic efficiency of the inlet. Hence, the alignment of the inlet lips were arbitrarily chosen to be 30° from the horizontal (in the top view), and also 30° from the vertical (in the side view). A further compromise with respect to the

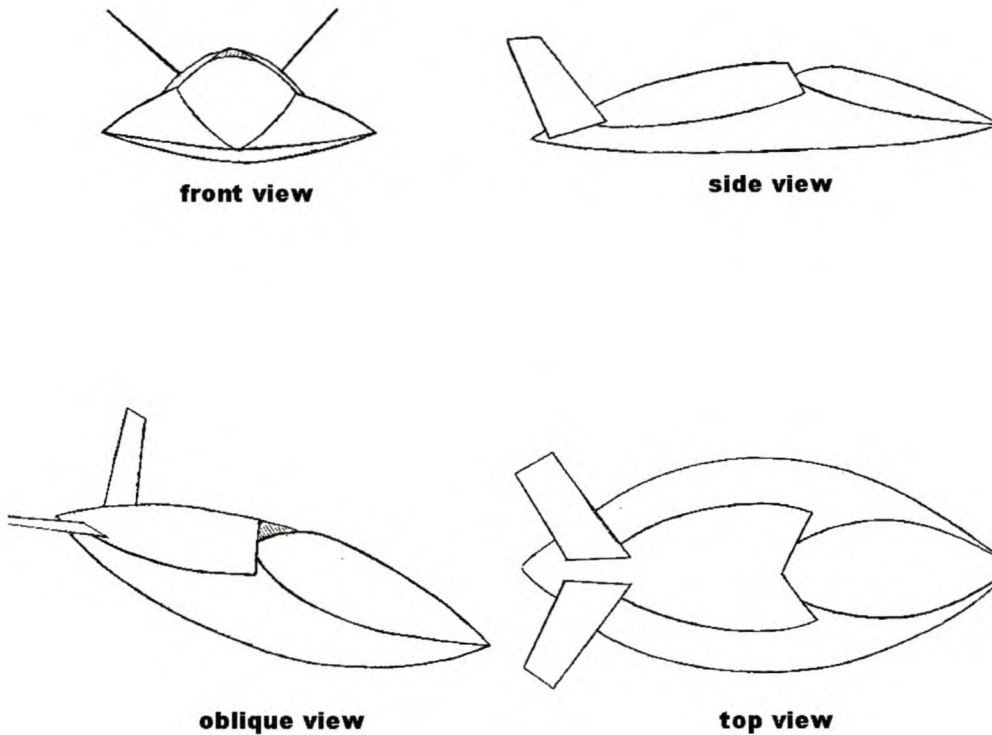


Figure A.6: Bump-shielded inlet, concept sketch

aerodynamic properties of the inlet is the fact that the inlet lips have sharp instead of rounded leading edges. As explained in section 1.3, rounded inlet lips provide a smooth surface for flow to accelerate into and around the inlet, whereas there is a greater probability of flow separation at a sharp leading edge. Sharp edges are however preferred from a stealth viewpoint.

The decision was made to investigate the flow properties of the inlet *without* a system to control the ingested fuselage boundary layer. The main reason is to obtain a “worst case” performance estimate for the inlet. Furthermore, it greatly simplifies the problem definition in the CFD package. Lastly, from a stealth viewpoint, the addition of, for instance, a boundary layer splitter plate would add extra edges that can reflect radar. Close investigation of the inlets on new-generation stealth aircraft such as the Boeing X-45, Northrop Grumman X-47 and Lockheed F-35 Joint Strike Fighter (shown in figure A.7) reveals no boundary layer splitter plates. This does not exclude the possibility that some other form of boundary layer control (like blowing to re-energise the boundary layer, or suction to remove it) is employed on these aircraft.

The geometry of the fuselage, from the nose tip up to the variable geometry part of the bump, was generated from the basic data on distances and angles, as shown in Figure A.1. This is therefore not part of the design *per se*, but rather an attempt to simulate realistic boundary conditions for the flow at the inlet. Figures A.8 and A.9 show the two extreme external



Figure A.7: Inlet detail on Lockheed F-35

configurations of the bump. Note that these figures do not represent the whole aircraft, but only the fuselage up to the inlet.

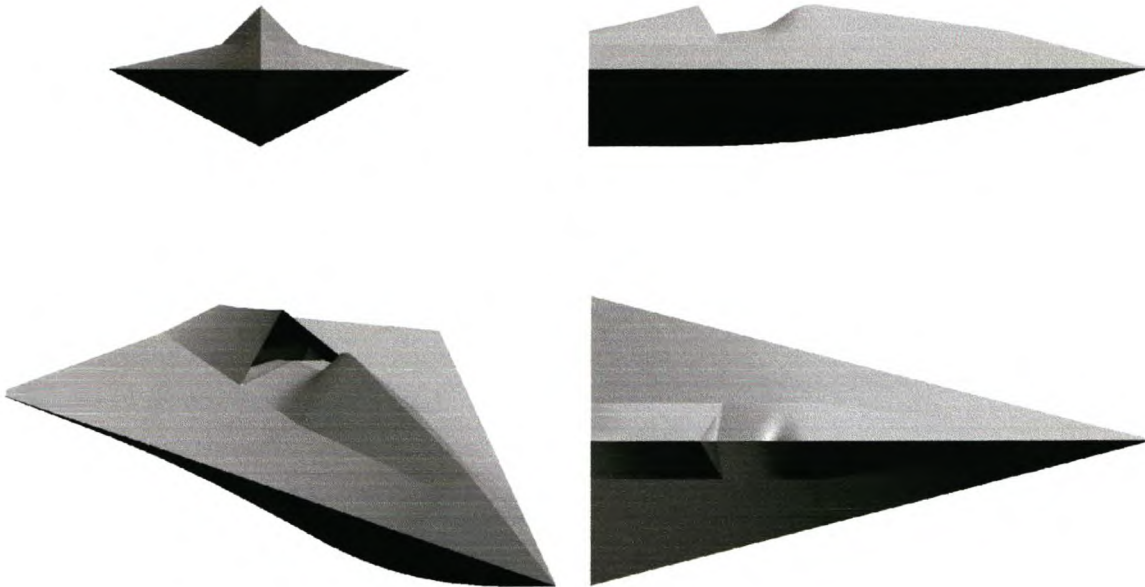


Figure A.8: External inlet design, bump-down configuration

A.7.2 Internal inlet configuration

The original concept drawing (figure A.5) specifies that the engine is buried inside the fuselage, in order to hide the compressor face. Additionally a changing cross-sectional profile is suggested for the duct, to prevent any radar energy that might still enter it from reaching the compressor face: electromagnetic radiation cannot pass through an opening that is smaller than its wavelength, which explains the rectangular cross section.

To accommodate these specifications, as well as the geometric constraints depicted in figure A.5, the S-shaped duct shown in figure A.10 was developed. Note that this represents the cavity *inside* the duct.

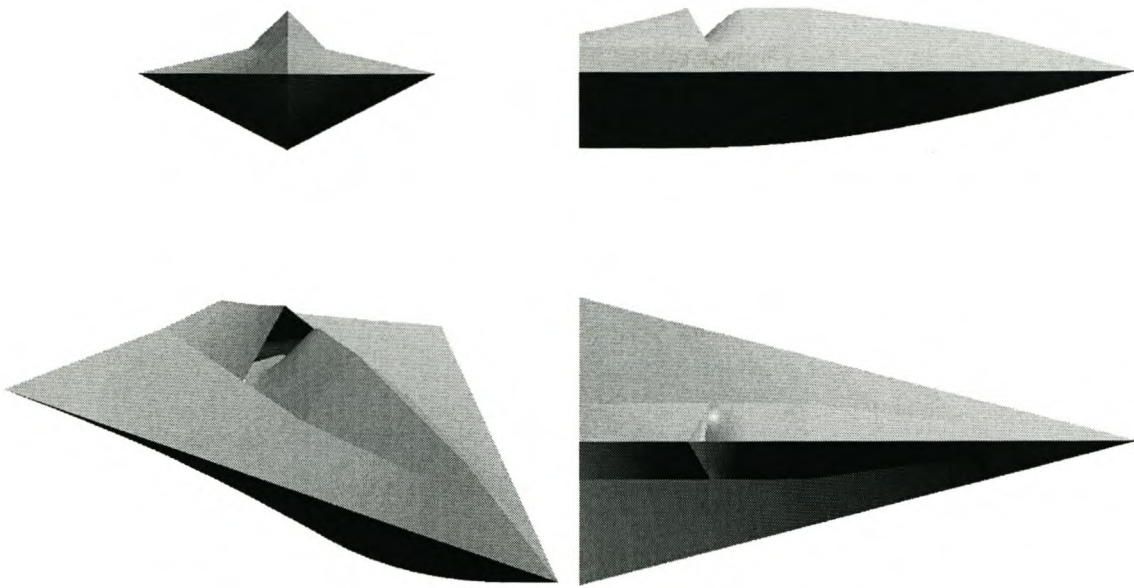


Figure A.9: External inlet design, bump-up configuration

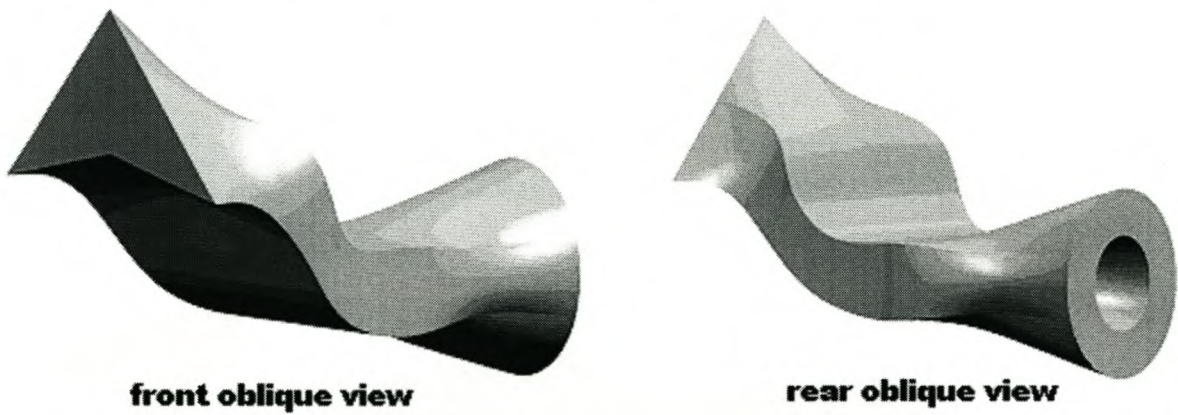


Figure A.10: Internal geometry

To prevent flow separation at the two sharp curves, the initial part of the duct was designed with a decreasing cross-sectional area, in order to maintain a favourable pressure gradient. Hence, only the rear part acts as a diffuser, as shown in figure A.11.

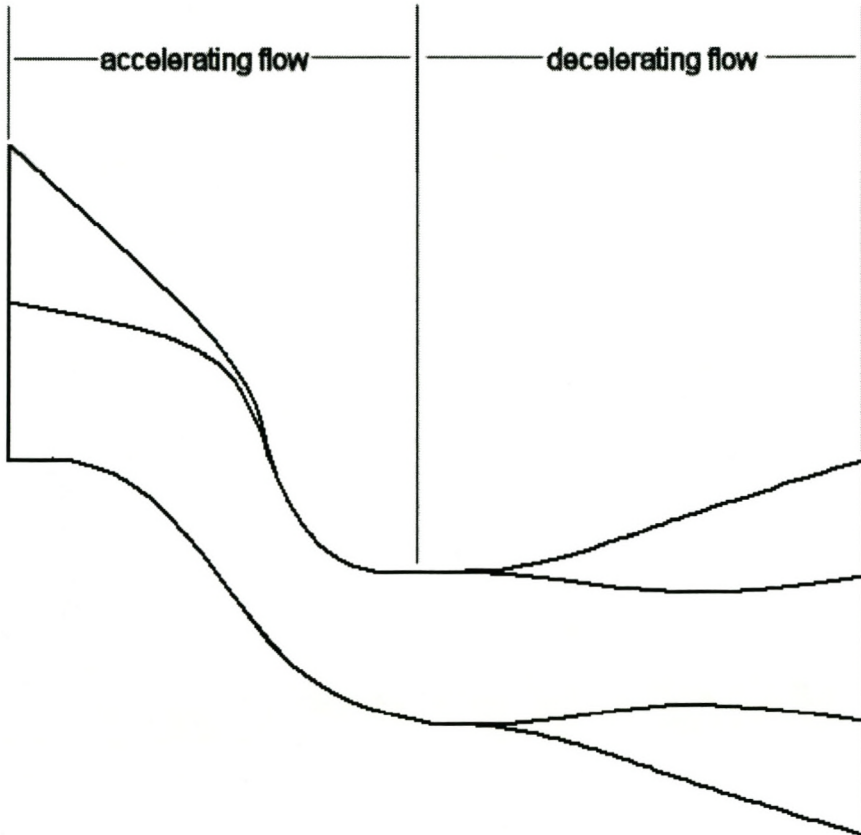


Figure A.11: Inlet duct: side view

Appendix B

Background information on CFX 5.5

B.1 Objectives

In this appendix, the basic principles on which the CFD code operates are explained. Topics that were found to be of particular importance during this project are emphasised. Some theory is presented, but only where it is necessary to clarify a certain concept.

The software that was used is CFX 5.5, a commercial package developed by AEA Technologies. The numerical solver is based on a three-dimensional Finite Volume Method, using an unstructured grid approach (see Section B.3 for more on the grid generation technique).

B.2 Governing equations

The set of equations describing the processes of momentum, heat and mass transfer in a fluid are known as the Navier-Stokes equations. In Cartesian coordinates, equations B.1 to B.3 govern the transport of momentum, and equation B.4 is the continuity equation, governing the conservation of mass. These are a set of coupled partial differential equations to which no general analytical solution is known.

$$\frac{\partial}{\partial t}(\rho u) + \nabla \cdot (\rho \vec{V} u) = -\frac{\partial p}{\partial x} + \nabla \cdot (\mu \nabla u) + S^u \quad (\text{B.1})$$

$$\frac{\partial}{\partial t}(\rho v) + \nabla \cdot (\rho \vec{V} v) = -\frac{\partial p}{\partial y} + \nabla \cdot (\mu \nabla v) + S^v \quad (\text{B.2})$$

$$\frac{\partial}{\partial t}(\rho w) + \nabla \cdot (\rho \vec{V} w) = -\frac{\partial p}{\partial z} + \nabla \cdot (\mu \nabla w) + S^w \quad (\text{B.3})$$

$$\frac{\partial \rho}{\partial t} + \nabla \cdot (\rho \vec{V}) = 0 \quad (\text{B.4})$$

where

$$S^u = f_x + \frac{\partial}{\partial x} \left(\mu \left(\frac{\partial u}{\partial x} - \frac{2}{3} \nabla \cdot \vec{V} \right) \right) + \frac{\partial}{\partial y} \left(\mu \frac{\partial v}{\partial x} \right) + \frac{\partial}{\partial z} \left(\mu \frac{\partial w}{\partial x} \right) \quad (\text{B.5})$$

$$S^v = f_y + \frac{\partial}{\partial y} \left(\mu \left(\frac{\partial v}{\partial y} - \frac{2}{3} \nabla \cdot \vec{V} \right) \right) + \frac{\partial}{\partial z} \left(\mu \frac{\partial w}{\partial y} \right) + \frac{\partial}{\partial x} \left(\mu \frac{\partial u}{\partial y} \right) \quad (\text{B.6})$$

$$S^w = f_z + \frac{\partial}{\partial z} \left(\mu \left(\frac{\partial w}{\partial z} - \frac{2}{3} \nabla \cdot \vec{V} \right) \right) + \frac{\partial}{\partial x} \left(\mu \frac{\partial u}{\partial z} \right) + \frac{\partial}{\partial y} \left(\mu \frac{\partial v}{\partial z} \right) \quad (\text{B.7})$$

In these equations, p denotes the static pressure, and f_x , f_y and f_z the external or “body” forces per unit volume [23, Chapter 5].

In the Finite Volume Method, the region of interest is divided into small subregions, called control volumes. The governing equations (B.1 to B.4) are discretised and solved iteratively for each control volume. As a result, an approximation of the value of each variable at specific points throughout the domain can be obtained. By interpolating between these points, one can derive an image of the complete flowfield [24, p.239].

B.3 Meshing

As noted in Section B.2, CFX 5.5 uses an unstructured grid approach. The boundaries of the fluid domain are discretised into triangular surface elements which are then used as starting points to “fill in” the volume with tetrahedral volume elements, creating the unstructured volume mesh. The tetrahedrons are used to define the control volumes required to solve the discretised governing equations. This is opposed to a structured (or regular) grid approach, where the boundaries are discretised into quadrilateral surface elements, and the volume filled with hexahedral volume elements. Figure B.1 compares unstructured and structured grids.

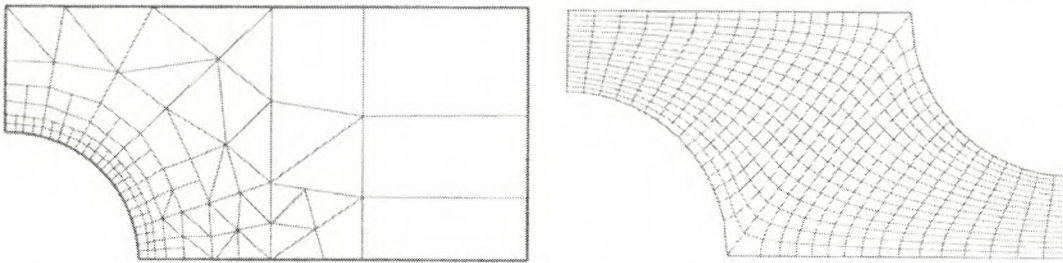


Figure B.1: Two-dimensional unstructured (left) and structured (right) grids [19]

Structured grids have the advantage that each point P has six neighbours in three dimensions, of which the i , j or k indices differ by ± 1 from the corresponding index of P . The matrix of the algebraic equation system also has a regular structure, which can be exploited in developing

an efficient solution technique. Structured grids are, however, mainly used for relatively simple geometries, as generating a volume mesh for complex geometries is extremely difficult, time-consuming and cannot be easily automated.

Unstructured grids are the most flexible type of grid for very complex geometries, because it can fit an arbitrary solution domain boundary. A big advantage is that an unstructured grids can be generated automatically by existing algorithms. The main disadvantage is in the irregularity in the data structure. The solvers for the algebraic equation system are usually slower than those for structured grids, partly because node locations and neighbour connections need to be specified explicitly. This does, however, make computer codes for unstructured grids more flexible than for structured grids. The volume elements are not restricted to a certain shape, so that a volume mesh consisting of both tetrahedral and hexahedral elements would pose no problem to the solver [19, pp.26-29].

In general, an unstructured volume mesh will not adequately resolve boundary layer flow, unless a prohibitively fine surface mesh is used. To remedy this, CFX 5.5 makes it possible to create a structured mesh on the surface, by “inflating” the surface mesh up to a pre-defined height. The unstructured volume mesh is then created “on top of” the structured layer. This is illustrated in Figure B.2.

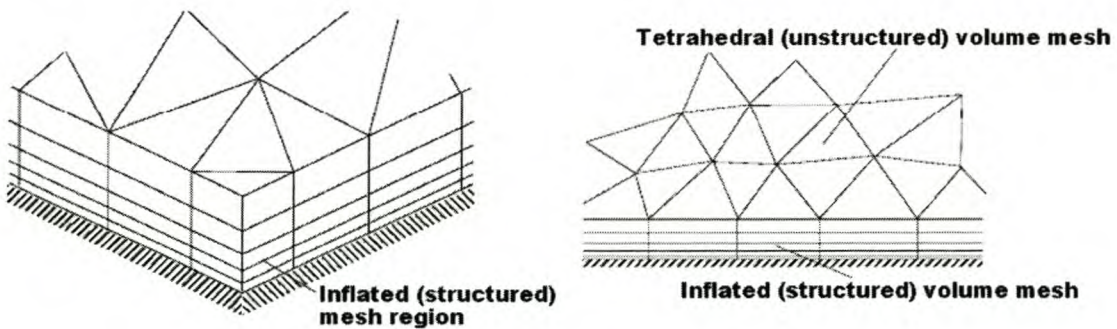


Figure B.2: Mesh inflation [25]

The number of the volume mesh nodes in the normal direction to the wall, as well as their spacing, is important in properly resolving the boundary layer. The CFX User’s Manual recommends at least 10 nodes in the inflated layers [18, p.295]. The node spacing is determined by the boundary layer thickness, which has to be approximated beforehand. The first node next to the wall is then positioned at a normal distance of $y^+ = 11$, the defined transition point between the laminar sublayer and the log-law layer in a turbulent boundary layer. This ensures that the flow is calculated in the sublayer, and not approximated entirely by turbulent wall functions. Increasing the number of elements in the sublayer may lead to elements with very high aspect ratios.

B.4 Turbulence modelling

In principle, the Navier-Stokes equations describe both laminar and turbulent flows. At high Reynolds numbers, however, the solutions of these equations become chaotic and unsteady, with fluctuations much smaller than can be resolved with practical volume meshes. For this reason turbulence models have been developed to account for the effects of turbulence. This is generally based on modifying the unsteady terms in the Navier-Stokes equations by separating the fluctuating property from its time-mean value. This time-averaging procedure produces the Reynolds Averaged Navier-Stokes Equations (RANSE). Additional unknown terms are introduced, containing the products of the fluctuating quantities, which act like viscous stresses, termed “Reynolds stresses”, in the fluid.

A number of turbulence models are available in CFX 5.5. For the purpose of code validation, the results obtained from two two-equation models (where the additional variables introduced in the RANSE are solved using two separate transport equations) are compared. These are the standard $k - \varepsilon$ model and the Shear Stress Transport (SST) model. Both are “eddy viscosity models”, which model turbulence as small eddies that are continually forming and dissipating, and in which the Reynolds stresses are assumed to be proportional to mean velocity gradients. The viscous stresses can then be said to be due to an “eddy viscosity” μ_t , added to the molecular viscosity in the RANSE [18, pp.273-279].

For the eddy viscosity assumption, the RANSE are given by the following set of equations [23, Chapter 5],

$$\frac{\partial \rho}{\partial t} + \nabla \cdot (\rho \vec{V}) = 0 \quad (\text{B.8})$$

$$\frac{\partial}{\partial t}(\rho \bar{u}) + \nabla \cdot (\rho \vec{V} \bar{u}) = -\frac{\partial}{\partial x} \left(\bar{p} + \frac{2}{3} \rho k \right) + \nabla \cdot ((\mu + \mu_t) \nabla \bar{u}) + \overline{S^u} \quad (\text{B.9})$$

$$\frac{\partial}{\partial t}(\rho \bar{v}) + \nabla \cdot (\rho \vec{V} \bar{v}) = -\frac{\partial}{\partial y} \left(\bar{p} + \frac{2}{3} \rho k \right) + \nabla \cdot ((\mu + \mu_t) \nabla \bar{v}) + \overline{S^v} \quad (\text{B.10})$$

$$\frac{\partial}{\partial t}(\rho \bar{w}) + \nabla \cdot (\rho \vec{V} \bar{w}) = -\frac{\partial}{\partial z} \left(\bar{p} + \frac{2}{3} \rho k \right) + \nabla \cdot ((\mu + \mu_t) \nabla \bar{w}) + \overline{S^w} \quad (\text{B.11})$$

where a bar indicates a time-averaged variable. k is the turbulence kinetic energy per unit mass, defined as

$$k = \frac{1}{2} (\overline{u'u'} + \overline{v'v'} + \overline{w'w'}) \quad (\text{B.12})$$

where the primes indicate the time-dependent fluctuation of the velocity components about the average value.

B.4.1 $k - \varepsilon$ model

The $k - \varepsilon$ model is considered to be the industry standard two-equation turbulence model [18, Turbulence and Near-Wall Modelling]. ε is the turbulence eddy dissipation (the rate at which the turbulent kinetic energy dissipates). The eddy viscosity is computed from the turbulence kinetic energy and the dissipation via equation B.13

$$\mu_t = C_\mu \rho \frac{k^2}{\varepsilon} \quad (\text{B.13})$$

where C_μ is a constant [18, pp.279-280].

One of the main problems with the $k - \varepsilon$ model is that it often fails to give realistic results in flows with an adverse pressure gradient, and hence it is unsuccessful in predicting the associated displacement effect and boundary layer separation. The reason for this is that the formulation of the eddy viscosity in equation B.13 fails to recognise that the principle turbulent shear stress is proportional to k in the wake region of the boundary layer. This failure causes the model to miss the transport of turbulent shear stress in the boundary layer, leading to an overprediction of shear stress levels in the logarithmic part of the boundary layer [26]. These higher shear stress levels manifests in a computed boundary layer that is more “resistant” to separation.

The $k - \varepsilon$ model relies on “wall functions” to supply the boundary conditions in the near-wall region when the mesh is not fine enough to resolve the boundary layer. Its “near-wall” version also involves complex non-linear damping functions, which can influence accuracy and robustness.

B.4.2 SST model

The SST Model of Menter [26] is based on the $k - \omega$ model of Wilcox [27]. ω is the turbulence frequency, defined as:

$$\omega = \frac{\varepsilon}{\beta^* k} \quad (\text{B.14})$$

where β^* is a constant. The advantage of the $k - \omega$ formulation lies in its near-wall treatment, in that an analytical expression is known for ω in the viscous sublayer, eliminating the need for complex wall functions [18, p.298]. Neither does the model involve the complex damping functions required for the $k - \varepsilon$ model, making it more accurate and robust [18, p.281]. It does require, however, that the mesh be fine enough to resolve the boundary layer. The eddy viscosity is given by:

$$\mu_t = \frac{\rho k}{\omega} \quad (\text{B.15})$$

The disadvantage of Wilcox’s model is that it is very sensitive to the (quite arbitrary)

freestream values of ω specified outside the boundary layer, a weakness not displayed by the $k - \varepsilon$ model. Like the $k - \varepsilon$ model, it also misses the transportation of turbulence shear stress, with the same consequences as explained in section B.4.1. In developing the SST model, Menter addressed the first problem by using a blending function to activate the $k - \omega$ model in the near wall region, and the $k - \varepsilon$ model in the outer wake region and free shear layers. The second problem is addressed by modifying the definition of the eddy viscosity to account for the transport of the principle turbulent shear stress, as will be explained in the following paragraphs.

Because flow separation is such an important phenomenon in many technical applications, much research has gone into developing turbulence models that can correctly predict the onset and amount of flow separation. Johnson and King [28] developed a successful algebraic model that features a transport equation for the turbulent shear stress τ_t . This is based on Bradshaw's observation that the principle turbulent shear stress is proportional to the turbulent kinetic energy in the wake region of the boundary layer:

$$\tau_t = \rho a_1 k \quad (\text{B.16})$$

where a_1 is a constant. In two-equation models, the shear stress is computed from:

$$\tau_t = \mu_t \Omega \quad (\text{B.17})$$

with $\Omega = (\partial u)/(\partial y)$. Equation B.17 can be rewritten as:

$$\tau_t = \rho \sqrt{\frac{\text{Production}_k}{\text{Dissipation}_k}} a_1 k \quad (\text{B.18})$$

According to equation B.16, the ratio of production to dissipation of k should equal 1, which is true for fully developed flow. For a boundary layer in an adverse pressure gradient, Driver [29] has shown experimentally that this ratio is significantly larger than one, and thus equation B.18 lead to the overprediction of the turbulent shear stress, as mentioned in section B.4.1. To satisfy equation B.16 from an eddy-viscosity formulation, the eddy viscosity is redefined as:

$$\mu_t = \frac{a_1 k}{\max(a_1 \omega; \Omega F_1)} \quad (\text{B.19})$$

where F_2 is a function that is zero in free shear layers and unity in the boundary-layer. Because the production to dissipation ratio for k is larger than one in an adverse pressure gradient, ($\Omega > a_1 \omega$) and equation B.19 guarantees that equation B.16 is satisfied. In a free shear layer, ($a_1 \omega > \Omega$), and the original formulation of the eddy viscosity is recovered.

In reference [26], numerical results based on the $k - \varepsilon$, $k - \omega$ and SST model are compared to experimental data for flows with strong adverse pressure gradients. The SST model consistently

delivered superior results to the other models. The CFX 5 Solver manual also recommends this model for high-accuracy boundary layer simulations [18, Turbulence and Near-Wall Modelling]

B.5 Boundary conditions

The governing equations have an infinite number of solutions on a given geometry. The uniqueness of a solution depends on the specification of the flow variables (or their derivatives) at the boundaries of the computational domain. This closes the problem numerically.

CFX 5.5 has 6 main types of boundary conditions, namely Inlet, Outlet, Opening, Wall, Symmetry plane and Periodic pair. These are discussed in sections B.5.1 to B.5.6.

B.5.1 Inlet

An Inlet is defined as a boundary across which flow is only allowed to enter the computational domain. Momentum, energy and turbulence variable values have to be specified on the boundary. The momentum flux is determined by specifying *one* of the following parameters:

1. the velocity normal to the boundary,
2. the cartesian velocity components,
3. the mass flow rate through the boundary, or
4. the static pressure relative to a pre-defined reference value.

For the parameters 1, 2 and 4 above, the specified value is applied at each grid point.

Unless the flow has been previously defined to be isothermal, the static temperature on the boundary must be specified. Turbulence quantities for two-equation models are determined by specifying either the turbulence intensity and length scale, or values for k and ε .

B.5.2 Outlet

An Outlet is a boundary where flow is only allowed to exit the computational domain. Only the momentum flux needs to be specified on this type of boundary, using the same parameters as for an inlet. If the static pressure is specified, the user has a choice regarding whether that pressure is applied uniformly across the boundary, or if it should be the average static pressure on the boundary. Energy and turbulence values are extrapolated from upstream values.

B.5.3 Opening

An Opening allows both inflow and outflow across the boundary. The momentum flux is defined similar to that for an Inlet, except that no provision is made to specify a mass flow rate across

the boundary. Energy and turbulence values are specified as for an Inlet, but where outflow across an Opening occurs, a zero-gradient condition is applied for these quantities.

B.5.4 Wall

At a Wall, the velocity component normal to the boundary is defined to be zero. The wall can either be moving or stationary, with the no slip condition applied to ensure that the relative velocity between the wall and the fluid directly next to it is zero. It is also possible to define a free slip wall, at which the no slip condition is not enforced.

B.5.5 Symmetry plane

A Symmetry plane ensures that all flow variables are symmetric about the specified plane. This is useful when the user is sure that the flow is steady and symmetric about the specified plane, or in the solution of two-dimensional problems.

B.5.6 Periodic pair

For a Periodic pair, the flow conditions due to outflow on one of the specified faces is used as the entrance conditions at the other specified face. This type of boundary is normally employed in simulating rotating machinery.

B.6 Advection schemes

The governing equations are discretised using a Taylor-series expansion, and the derivatives of the variables at a point is approximated by interpolating from the values of that variable at neighbouring points. In the discretised equations, the higher-order terms are neglected, leading to a truncation error manifesting in the computed results. This error is reduced as the grid spacing is reduced, with the numerical and “real” results being (theoretically) equal in the limit.

Various interpolation schemes can be used: “First-order” schemes neglect all terms of order two and higher. The first-order scheme most often employed is termed the “upwind differencing scheme” (UDS) because only upstream values are used to compute the variables at a point [23, Chapter 3]. Its main advantage is that it is numerically robust. The UDS scheme is *numerically diffusive*, meaning that when the flow is oblique to the grid, the truncation error produces a false diffusion in the direction normal to the flow, as well as in the streamwise direction. This false diffusion causes peaks or rapid variations in the variables to be “smeared out” [19, Chapter 4]. On unstructured grids, false diffusion will always be present, because there is no single direction in which the cells are aligned [18, p.344].

“Second-order” schemes (where terms of order three and higher are neglected) are more accurate, without the problem of false diffusion. They are usually based on a Central Difference Scheme, where both upstream and downstream values are used to compute the derivative at a point. They are less robust though, and require a careful definition of initial values to ensure numerical stability. The second-order differencing scheme employed in CFX 5.5 exhibits a phenomenon called *numerical dispersion*, which results in oscillations in the solution, particularly where there are steep flow gradients [18, pp.345-346]

The CFX 5.5 solver has three options for specifying the advection scheme: ‘1st Order’, naturally refers to the UDS scheme. The “Specify Blend” option allows the user to set a blend factor value between 0 and 1, where 0 is equivalent to “1st Order”, and 1 enforces full second-order differencing for the advection terms. The “2nd Order High Resolution” scheme calculates the blend factor locally throughout the flow field. In flow regions with low variable gradients, the Blend Factor will be close to 1.0 for accuracy, but where the gradients change sharply, it will be closer to 0.0 to prevent numerical dispersion and maintain robustness [25, Chapter 10].

Appendix C

Details of CFD models for validation cases

The tables in this appendix gives information on the solution variables and convergence history of the simulations that were run for the purpose of code validation. Unless otherwise mentioned, all simulations were run on a 1300 MHz AMD Athlon processor with 512 MB of RAM.

Run times are reported as *hours:minutes*. The error convergence data is reported as *initial residual; final residual*, where the reported size is the RMS value for the particular variable. The CFX 5.5 solver treats the turbulence variables as converged when their residuals are no more than one order of magnitude larger than the specified target RMS residual.

C.1 Flat plate

C.1.1 Structured mesh

Solution variable	Value	Comment
Run time	01:14	
Total number of iterations	49	
Advection time	0.01 s	
False time step	0.03 s	
Target RMS residual	1×10^{-5}	
Error convergence		
U Momentum	2.1×10^{-3} ; 5.1×10^{-5}	Error stabilised after 28 iterations
V Momentum	1.7×10^{-3} ; 1.2×10^{-7}	
W Momentum	1.8×10^{-4} ; 3.5×10^{-8}	
Continuity	6.7×10^{-4} ; 1.7×10^{-6}	Error stabilised after 28 iterations
k	2.7×10^{-2} ; 1.8×10^{-5}	Error stabilised after 33 iterations
ε	6.7×10^{-2} ; 1.2×10^{-5}	Error stabilised after 33 iterations

Table C.1: Details of numerical simulation: Flat plate structured mesh, UDS, $k - \varepsilon$

Solution variable	Value	Comment
Run time	01:32	
Total number of iterations	57	Started with UDS, $k - \varepsilon$ solution
Advection time	0.01 s	
False time step	0.01 s	
Target RMS residual	1×10^{-5}	
Error convergence		
U Momentum	1.7×10^{-3} ; 6.7×10^{-5}	Error stabilised after 35 iterations
V Momentum	7.5×10^{-5} ; 4.1×10^{-7}	
W Momentum	1.6×10^{-6} ; 4.9×10^{-8}	
Continuity	5.9×10^{-6} ; 2.3×10^{-6}	Error stabilised after 35 iterations
k	2.0×10^{-2} ; 6.7×10^{-4}	Error stabilised after 40 iterations
ε	3.0×10^{-2} ; 1.5×10^{-5}	Error stabilised after 40 iterations

Table C.2: Details of numerical simulation: Flat plate structured mesh, 2nd, $k - \varepsilon$

Solution variable	Value	Comment
Run time	00:53	
Total number of iterations	26	Started with UDS, $k - \varepsilon$ solution
Advection time	0.01 s	
False time step	0.01 s	
Target RMS residual	1×10^{-5}	
Error convergence		
U Momentum	1.7×10^{-3} ; 3.8×10^{-5}	Error stabilised after 16 iterations
V Momentum	7.9×10^{-5} ; 3.9×10^{-7}	
W Momentum	2.1×10^{-6} ; 3.6×10^{-8}	
Continuity	8.3×10^{-6} ; 1.3×10^{-6}	Error stabilised after 16 iterations
k	1.9×10^{-2} ; 1.1×10^{-5}	Error stabilised after 22 iterations
ε	2.9×10^{-2} ; 7.2×10^{-6}	Error stabilised after 22 iterations

Table C.3: Details of numerical simulation: Flat plate structured mesh, 2ndhr, $k - \varepsilon$

Solution variable	Value	Comment
Run time	00:42	
Total number of iterations	26	
Advection time	0.01 s	
False time step	0.03 s	
Target RMS residual	1×10^{-5}	
Error convergence		
U Momentum	1.1×10^{-3} ; 1.1×10^{-4}	Error stabilised after 10 iterations
V Momentum	5.2×10^{-5} ; 2.2×10^{-7}	
W Momentum	4.7×10^{-7} ; 4.4×10^{-8}	
Continuity	5.6×10^{-6} ; 3.0×10^{-6}	Error stabilised after 10 iterations
k	2.0×10^{-2} ; 5.4×10^{-6}	Error stabilised after 16 iterations
ω	3.0×10^{-2} ; 1.2×10^{-5}	Error stabilised after 24 iterations

Table C.4: Details of numerical simulation: Flat plate structured mesh, UDS, SST

Solution variable	Value	Comment
Run time	02:33	450 MHz Intel Celeron, 786 MB RAM
Total number of iterations	42	Started with UDS, $k - \varepsilon$ solution
Advection time	0.01 s	
False time step	0.01 s	
Target RMS residual	1×10^{-5}	
Error convergence		
U Momentum	1.5×10^{-3} ; 9.1×10^{-5}	Error stabilised after 12 iterations
V Momentum	7.9×10^{-5} ; 5.4×10^{-7}	
W Momentum	1.9×10^{-6} ; 8.7×10^{-8}	
Continuity	7.8×10^{-6} ; 2.5×10^{-6}	Error stabilised after 12 iterations
k	2.0×10^{-2} ; 3.0×10^{-6}	Error stabilised after 32 iterations
ω	3.0×10^{-2} ; 6.8×10^{-6}	Error stabilised after 25 iterations

Table C.5: Details of numerical simulation: Flat plate structured mesh, 2nd, SST

Solution variable	Value	Comment
Run time	01:03	
Total number of iterations	34	Started with UDS, $k - \varepsilon$ solution
Advection time	0.01 s	
False time step	0.01 s	
Target RMS residual	1×10^{-5}	
Error convergence		
U Momentum	1.5×10^{-3} ; 9.0×10^{-5}	Error stabilised after 15 iterations
V Momentum	7.9×10^{-5} ; 5.7×10^{-7}	
W Momentum	1.9×10^{-6} ; 8.6×10^{-8}	
Continuity	7.8×10^{-6} ; 2.5×10^{-6}	Error stabilised after 15 iterations
k	4.4×10^{-2} ; 4.3×10^{-6}	
ω	1.1×10^{-1} ; 9.9×10^{-6}	Error stabilised after 21 iterations

Table C.6: Details of numerical simulation: Flat plate structured mesh, 2ndhr, SST

C.1.2 Unstructured mesh

Solution variable	Value	Comment
Run time	00:35	
Total number of iterations	24	
Advection time	0.01 s	
False time step	0.03 s	
Target RMS residual	1×10^{-4}	
Error convergence		
U Momentum	5.4×10^{-3} ; 7.7×10^{-5}	
V Momentum	4.6×10^{-5} ; 2.6×10^{-6}	
W Momentum	2.3×10^{-6} ; 2.4×10^{-7}	
Continuity	4.9×10^{-6} ; 5.1×10^{-6}	
k	1.8×10^{-2} ; 3.4×10^{-4}	
ε	2.4×10^{-2} ; 1.7×10^{-4}	

Table C.7: Details of numerical simulation: Flat plate unstructured mesh, UDS, $k - \varepsilon$

Solution variable	Value	Comment
Run time	01:32	
Total number of iterations	58	Started with UDS, $k - \varepsilon$ solution
Advection time	0.01 s	
False time step	0.03 s	
Target RMS residual	1×10^{-5}	
Error convergence		
U Momentum	8.4×10^{-3} ; 9.5×10^{-6}	
V Momentum	2.2×10^{-5} ; 1.0×10^{-6}	
W Momentum	1.8×10^{-6} ; 2.3×10^{-7}	
Continuity	2.7×10^{-5} ; 1.4×10^{-6}	
k	6.5×10^{-3} ; 5.0×10^{-6}	
ε	6.5×10^{-3} ; 2.9×10^{-6}	

Table C.8: Details of numerical simulation: Flat plate unstructured mesh, 2nd, $k - \varepsilon$

Solution variable	Value	Comment
Run time	01:45	
Total number of iterations	71	Started with UDS, $k - \varepsilon$ solution
Advection time	0.01 s	
False time step	0.03 s	
Target RMS residual	1×10^{-6}	
Error convergence		
U Momentum	1.0×10^{-2} ; 9.5×10^{-7}	
V Momentum	1.3×10^{-4} ; 5.5×10^{-7}	
W Momentum	1.4×10^{-5} ; 6.8×10^{-8}	
Continuity	4.8×10^{-5} ; 6.3×10^{-7}	
k	1.7×10^{-2} ; 9.9×10^{-7}	
ε	1.4×10^{-2} ; 7.4×10^{-7}	

Table C.9: Details of numerical simulation: Flat plate unstructured mesh, 2ndhr, $k - \varepsilon$

Solution variable	Value	Comment
Run time	01:49	
Total number of iterations	58	Started with UDS, $k - \varepsilon$ solution
Advection time	0.01 s	
False time step	0.01 s	
Target RMS residual	1×10^{-5}	
Error convergence		
U Momentum	1.3×10^{-2} ; 1.6×10^{-5}	Error stabilised after 35 iterations
V Momentum	6.4×10^{-5} ; 2.2×10^{-7}	
W Momentum	3.3×10^{-6} ; 2.2×10^{-8}	
Continuity	6.6×10^{-5} ; 5.1×10^{-7}	Error stabilised after 60 iterations
k	9.8×10^{-2} ; 9.9×10^{-6}	
ω	2.1×10^{-2} ; 7.2×10^{-7}	

Table C.10: Details of numerical simulation: Flat plate unstructured mesh, UDS, SST

Solution variable	Value	Comment
Run time	01:55	
Total number of iterations	68	Started with UDS, $k - \epsilon$ solution
Advection time	0.01 s	
False time step	0.03 s	
Target RMS residual	1×10^{-5}	
Error convergence		
U Momentum	1.7×10^{-2} ; 1.0×10^{-5}	
V Momentum	1.3×10^{-4} ; 9.9×10^{-7}	
W Momentum	1.4×10^{-5} ; 1.7×10^{-7}	
Continuity	4.8×10^{-5} ; 8.7×10^{-7}	
k	2.0×10^{-2} ; 1.0×10^{-5}	
ω	7.2×10^{-2} ; 2.2×10^{-6}	

Table C.11: Details of numerical simulation: Flat plate unstructured mesh, 2nd, SST

Solution variable	Value	Comment
Run time	02:35	
Total number of iterations	95	Started with UDS, $k - \epsilon$ solution
Advection time	0.01 s	
False time step	0.03 s	
Target RMS residual	1×10^{-6}	
Error convergence		
U Momentum	1.7×10^{-2} ; 9.0×10^{-7}	
V Momentum	1.3×10^{-4} ; 4.5×10^{-7}	
W Momentum	1.4×10^{-5} ; 4.9×10^{-8}	
Continuity	4.8×10^{-5} ; 3.4×10^{-7}	
k	2.0×10^{-2} ; 2.6×10^{-6}	
ω	7.2×10^{-2} ; 3.7×10^{-7}	

Table C.12: Details of numerical simulation: Flat plate unstructured mesh, 2ndhr, SST

C.2 Rankine halfbody

Solution variable	Value	Comment
Run time	00:44	
Total number of iterations	25	
Advection time	0.007 s	
False time step	0.01 s	
Target RMS residual	1×10^{-5}	
Error convergence		
U Momentum	5.8×10^{-3} ; 1.0×10^{-5}	
V Momentum	3.4×10^{-3} ; 5.3×10^{-6}	
W Momentum	3.4×10^{-3} ; 5.2×10^{-6}	
Continuity	2.8×10^{-2} ; 7.7×10^{-7}	
k	2.2×10^{-1} ; 1.4×10^{-4}	
ε	8.3×10^{-2} ; 1.4×10^{-4}	

Table C.13: Details of numerical simulation: Rankine halfbody, UDS, $k - \varepsilon$

Solution variable	Value	Comment
Run time	01:39	
Total number of iterations	56	Started with UDS, $k - \varepsilon$ solution
Advection time	0.007 s	
False time step	0.0025 s	
Target RMS residual	1×10^{-5}	
Error convergence		
U Momentum	8.3×10^{-3} ; 9.9×10^{-6}	
V Momentum	4.5×10^{-3} ; 1.8×10^{-7}	
W Momentum	4.5×10^{-3} ; 1.8×10^{-7}	
Continuity	4.5×10^{-2} ; 9.1×10^{-8}	
k	3.6×10^{-2} ; 1.4×10^{-7}	
ε	2.6×10^{-2} ; 1.4×10^{-7}	

Table C.14: Details of numerical simulation: Rankine halfbody, 2nd, $k - \varepsilon$

Solution variable	Value	Comment
Run time	01:39	
Total number of iterations	56	Started with UDS, $k - \varepsilon$ solution
Advection time	0.007 s	
False time step	0.0025 s	
Target RMS residual	1×10^{-5}	
Error convergence		
U Momentum	8.3×10^{-3} ; 9.9×10^{-6}	
V Momentum	4.5×10^{-3} ; 1.8×10^{-7}	
W Momentum	4.5×10^{-3} ; 1.8×10^{-7}	
Continuity	4.5×10^{-2} ; 9.1×10^{-8}	
k	3.6×10^{-2} ; 1.4×10^{-7}	
ε	2.6×10^{-2} ; 1.4×10^{-7}	

Table C.15: Details of numerical simulation: Rankine halfbody, 2ndhr, $k - \varepsilon$

Solution variable	Value	Comment
Run time	00:37	
Total number of iterations	19	Started with UDS, $k - \varepsilon$ solution
Advection time	0.007 s	
False time step	0.01 s	
Target RMS residual	1×10^{-5}	
Error convergence		
U Momentum	8.6×10^{-3} ; 9.0×10^{-6}	
V Momentum	4.5×10^{-3} ; 5.2×10^{-6}	
W Momentum	4.5×10^{-3} ; 5.7×10^{-6}	
Continuity	4.5×10^{-2} ; 4.7×10^{-8}	
k	3.0×10^{-2} ; 5.5×10^{-5}	
ω	2.1×10^{-2} ; 2.5×10^{-5}	

Table C.16: Details of numerical simulation: Rankine Halfbody, UDS, SST

Solution variable	Value	Comment
Run time	01:44	
Total number of iterations	56	Started with UDS, SST solution
Advection time	0.007 s	
False time step	0.0025 s	
Target RMS residual	1×10^{-5}	
Error convergence		
U Momentum	8.8×10^{-3} ; 9.9×10^{-6}	
V Momentum	4.7×10^{-3} ; 1.8×10^{-7}	
W Momentum	4.8×10^{-3} ; 1.8×10^{-7}	
Continuity	4.3×10^{-2} ; 9.0×10^{-8}	
k	5.6×10^{-2} ; 1.8×10^{-7}	
ω	8.4×10^{-3} ; 7.6×10^{-8}	

Table C.17: Details of numerical simulation: Rankine Halfbody, 2nd, SST

Solution variable	Value	Comment
Run time	01:03	
Total number of iterations	31	Started with UDS, SST solution
Advection time	0.007 s	
False time step	0.0025 s	
Target RMS residual	1×10^{-5}	
Error convergence		
U Momentum	8.8×10^{-3} ; 8.8×10^{-6}	
V Momentum	4.8×10^{-3} ; 3.3×10^{-6}	
W Momentum	4.8×10^{-3} ; 3.1×10^{-6}	
Continuity	4.3×10^{-2} ; 3.6×10^{-7}	
k	5.6×10^{-2} ; 2.2×10^{-5}	
ω	8.4×10^{-3} ; 1.3×10^{-5}	

Table C.18: Details of numerical simulation: Rankine Halfbody, 2ndhr, SST

C.3 Sphere

Solution variable	Value	Comment
Run time	01:32	
Total number of iterations	41	
Advection time	0.027 s	
False time step	0.02 s	
Target RMS residual	1×10^{-4}	
Error convergence		
U Momentum	3.5×10^{-2} ; 1.3×10^{-4}	Error stabilised after 20 iterations
V Momentum	1.9×10^{-2} ; 1.5×10^{-4}	Error stabilised after 20 iterations
W Momentum	1.9×10^{-2} ; 1.8×10^{-4}	Error stabilised after 20 iterations
Continuity	5.7×10^{-2} ; 7.6×10^{-7}	Error stabilised after 29 iterations
k	2.8×10^{-1} ; 2.5×10^{-3}	Error stabilised after 16 iterations
ε	1.2×10^{-1} ; 4.8×10^{-3}	Error stabilised after 16 iterations

Table C.19: Details of numerical simulation: Sphere, UDS, $k - \varepsilon$

Solution variable	Value	Comment
Run time	04:29	
Total number of iterations	119	Started with UDS, $k - \varepsilon$ solution
Advection time	0.027 s	
False time step	0.005 s	
Target RMS residual	1×10^{-5}	
Error convergence		
U Momentum	1.4×10^{-2} ; 3.8×10^{-4}	Long-period oscillation about 2.5×10^{-4}
V Momentum	9.3×10^{-3} ; 2.5×10^{-4}	Long-period oscillation about 2.5×10^{-4}
W Momentum	9.3×10^{-3} ; 2.1×10^{-4}	Long-period oscillation about 2.5×10^{-4}
Continuity	7.7×10^{-2} ; 2.8×10^{-5}	Long-period oscillation about 2.0×10^{-5}
k	5.5×10^{-2} ; 2.3×10^{-3}	Error stabilised after 20 iterations
ε	2.9×10^{-2} ; 6.6×10^{-3}	Error stabilised after 80 iterations

Table C.20: Details of numerical simulation: Sphere, 2nd, $k - \varepsilon$

Solution variable	Value	Comment
Run time	07:53	
Total number of iterations	200	Started with UDS, $k - \varepsilon$ solution
Advection time	0.027 s	
False time step	0.005 s	
Target RMS residual	1×10^{-5}	
Error convergence		
U Momentum	1.4×10^{-2} ; 2.8×10^{-4}	Long-period oscillation about 2.5×10^{-4}
V Momentum	9.2×10^{-3} ; 2.2×10^{-4}	Long-period oscillation about 2.0×10^{-4}
W Momentum	9.2×10^{-3} ; 2.6×10^{-4}	Long-period oscillation about 2.0×10^{-4}
Continuity	7.7×10^{-2} ; 2.3×10^{-5}	Long-period oscillation about 2.0×10^{-5}
k	5.5×10^{-2} ; 2.1×10^{-3}	Error stabilised after 60 iterations
ε	3.0×10^{-2} ; 2.3×10^{-3}	Error stabilised after 60 iterations

 Table C.21: Details of numerical simulation: Sphere, 2ndhr, $k - \varepsilon$

Solution variable	Value	Comment
Run time	02:16	
Total number of iterations	61	Started with UDS, $k - \varepsilon$ solution
Advection time	0.027 s	
False time step	0.02 s	
Target RMS residual	1×10^{-5}	
Error convergence		
U Momentum	1.5×10^{-2} ; 9.9×10^{-6}	
V Momentum	9.1×10^{-3} ; 4.6×10^{-6}	
W Momentum	9.2×10^{-3} ; 8.8×10^{-6}	
Continuity	8.6×10^{-2} ; 5.8×10^{-7}	
k	4.8×10^{-2} ; 3.1×10^{-5}	
ω	7.8×10^{-2} ; 5.5×10^{-6}	

Table C.22: Details of numerical simulation: Sphere, UDS, SST

Solution variable	Value	Comment
Run time	08:04	
Total number of iterations	200	Started with UDS, SST solution
Advection time	0.027 s	
False time step	0.005 s	
Target RMS residual	1×10^{-5}	
Error convergence		
U Momentum	1.7×10^{-2} ; 5.6×10^{-4}	Long-period oscillation about 3.0×10^{-4}
V Momentum	1.0×10^{-2} ; 2.9×10^{-4}	Long-period oscillation about 2.0×10^{-4}
W Momentum	1.0×10^{-2} ; 4.0×10^{-4}	Long-period oscillation about 2.0×10^{-4}
Continuity	7.2×10^{-2} ; 4.5×10^{-5}	Long-period oscillation about 2.0×10^{-5}
k	1.3×10^{-1} ; 9.1×10^{-4}	Error stabilised after 100 iterations
ω	1.9×10^{-2} ; 4.1×10^{-4}	Error stabilised after 100 iterations

Table C.23: Details of numerical simulation: Sphere, 2nd, SST

Solution variable	Value	Comment
Run time	08:16	
Total number of iterations	200	Started with UDS, SST solution
Advection time	0.027 s	
False time step	0.005 s	
Target RMS residual	1×10^{-5}	
Error convergence		
U Momentum	1.7×10^{-2} ; 7.1×10^{-4}	Error stabilised after 70 iterations
V Momentum	1.0×10^{-2} ; 3.2×10^{-4}	Error stabilised after 70 iterations
W Momentum	1.0×10^{-2} ; 4.0×10^{-4}	Error stabilised after 70 iterations
Continuity	7.2×10^{-2} ; 5.8×10^{-5}	Error stabilised after 70 iterations
k	1.3×10^{-1} ; 2.2×10^{-3}	Error stabilised after 70 iterations
ω	1.9×10^{-2} ; 4.5×10^{-4}	Error stabilised after 70 iterations

Table C.24: Details of numerical simulation: Sphere, 2ndhr, SST

C.4 Pipe flow

C.4.1 Structured grid

Solution variable	Value	Comment
Run time	04:22	
Total number of iterations	1000	
Advection time	0.0075 s	
False time step	0.0023 s	
Target RMS residual	1×10^{-4}	
Error convergence		
U Momentum	3.2×10^{-4} ; 7.1×10^{-4}	Error stabilised after 550 iterations
V Momentum	4.4×10^{-4} ; 4.7×10^{-4}	Rapid oscillation about 4.7×10^{-4}
W Momentum	1.3×10^{-4} ; 1.5×10^{-4}	Rapid oscillation about 1.5×10^{-4}
Continuity	1.8×10^{-4} ; 1.5×10^{-4}	Rapid oscillation about 1.5×10^{-4}
k	6.4×10^{-4} ; 6.5×10^{-6}	Error stabilised after 550 iterations
ϵ	6.1×10^{-4} ; 1.4×10^{-7}	

Table C.25: Details of numerical simulation: Pipe flow structured mesh, UDS, $k - \epsilon$

Solution variable	Value	Comment
Run time	00:12	
Total number of iterations	39	Started with UDS, $k - \epsilon$ solution
Advection time	0.0075 s	
False time step	0.0023 s	
Target RMS residual	1×10^{-5}	
Error convergence		
U Momentum	1.1×10^{-4} ; 9.2×10^{-6}	
V Momentum	3.9×10^{-4} ; 7.2×10^{-7}	
W Momentum	3.0×10^{-4} ; 3.2×10^{-6}	
Continuity	9.6×10^{-5} ; 1.7×10^{-7}	
k	1.5×10^{-4} ; 2.6×10^{-5}	
ϵ	1.1×10^{-4} ; 1.5×10^{-5}	

Table C.26: Details of numerical simulation: Pipe flow structured mesh, 2nd, $k - \epsilon$

Solution variable	Value	Comment
Run time	00:12	
Total number of iterations	36	Started with UDS, $k - \epsilon$ solution
Advection time	0.0075 s	
False time step	0.0023 s	
Target RMS residual	1×10^{-5}	
Error convergence		
U Momentum	2.3×10^{-5} ; 9.4×10^{-6}	
V Momentum	3.9×10^{-4} ; 8.3×10^{-7}	
W Momentum	3.0×10^{-4} ; 2.6×10^{-6}	
Continuity	9.6×10^{-5} ; 2.0×10^{-7}	
k	5.3×10^{-5} ; 2.8×10^{-5}	
ϵ	2.9×10^{-5} ; 1.7×10^{-5}	

Table C.27: Details of numerical simulation: Pipe flow structured mesh, 2ndhr, $k - \epsilon$

Solution variable	Value	Comment
Run time	00:16	
Total number of iterations	50	Started with UDS, $k - \epsilon$ solution
Advection time	0.0075 s	
False time step	0.0023 s	
Target RMS residual	1×10^{-5}	
Error convergence		
U Momentum	7.2×10^{-4} ; 1.9×10^{-5}	
V Momentum	3.9×10^{-4} ; 4.8×10^{-7}	
W Momentum	3.0×10^{-4} ; 2.0×10^{-6}	
Continuity	9.6×10^{-5} ; 9.7×10^{-8}	
k	5.6×10^{-2} ; 1.8×10^{-4}	
ω	4.4×10^{-5} ; 3.8×10^{-5}	

Table C.28: Details of numerical simulation: Pipe flow structured mesh, UDS, SST

Solution variable	Value	Comment
Run time	00:17	
Total number of iterations	50	Started with UDS, $k - \varepsilon$ solution
Advection time	0.0075 s	
False time step	0.0023 s	
Target RMS residual	1×10^{-5}	
Error convergence		
U Momentum	7.2×10^{-4} ; 1.9×10^{-5}	
V Momentum	3.9×10^{-4} ; 5.1×10^{-7}	
W Momentum	3.0×10^{-4} ; 2.1×10^{-6}	
Continuity	9.6×10^{-5} ; 9.7×10^{-8}	
k	5.6×10^{-2} ; 1.8×10^{-4}	
ω	4.4×10^{-5} ; 3.9×10^{-5}	

Table C.29: Details of numerical simulation: Pipe flow structured mesh, 2nd, SST

Solution variable	Value	Comment
Run time	00:17	
Total number of iterations	50	Started with UDS, $k - \varepsilon$ solution
Advection time	0.0075 s	
False time step	0.0023 s	
Target RMS residual	1×10^{-5}	
Error convergence		
U Momentum	7.2×10^{-4} ; 1.2×10^{-5}	
V Momentum	3.9×10^{-4} ; 5.5×10^{-7}	
W Momentum	3.0×10^{-4} ; 2.1×10^{-6}	
Continuity	9.6×10^{-5} ; 9.7×10^{-8}	
k	5.6×10^{-2} ; 1.8×10^{-4}	
ω	4.4×10^{-5} ; 3.8×10^{-5}	

Table C.30: Details of numerical simulation: Pipe flow structured mesh, 2ndhr, SST

C.4.2 Unstructured grid

Solution variable	Value	Comment
Run time	02:57	
Total number of iterations	46	
Advection time	0.026 s	
False time step	0.4 s	
Target RMS residual	1×10^{-5}	
Error convergence		
U Momentum	3.5×10^{-2} ; 8.7×10^{-6}	
V Momentum	1.8×10^{-3} ; 1.2×10^{-7}	
W Momentum	1.8×10^{-3} ; 1.2×10^{-7}	
Continuity	1.7×10^{-3} ; 1.1×10^{-7}	
k	1.9×10^{-2} ; 1.4×10^{-4}	
ϵ	2.9×10^{-2} ; 1.3×10^{-4}	

Table C.31: Details of numerical simulation: Pipe flow unstructured mesh, UDS, $k - \epsilon$

Solution variable	Value	Comment
Run time	03:43	
Total number of iterations	55	Started with UDS, $k - \epsilon$ solution
Advection time	0.026 s	
False time step	0.1 s	
Target RMS residual	1×10^{-5}	
Error convergence		
U Momentum	3.1×10^{-3} ; 9.5×10^{-6}	
V Momentum	7.2×10^{-5} ; 1.3×10^{-7}	
W Momentum	7.9×10^{-5} ; 1.3×10^{-7}	
Continuity	1.2×10^{-6} ; 1.6×10^{-7}	
k	1.5×10^{-4} ; 1.4×10^{-5}	
ϵ	1.1×10^{-4} ; 1.5×10^{-5}	

Table C.32: Details of numerical simulation: Pipe flow unstructured mesh, 2nd, $k - \epsilon$

Solution variable	Value	Comment
Run time	02:54	
Total number of iterations	39	Started with 2nd, $k - \epsilon$ solution
Advection time	0.026 s	
False time step	0.1 s	
Target RMS residual	1×10^{-5}	
Error convergence		
U Momentum	4.9×10^{-3} ; 9.6×10^{-6}	
V Momentum	6.0×10^{-5} ; 7.2×10^{-6}	
W Momentum	6.6×10^{-5} ; 7.2×10^{-6}	
Continuity	2.3×10^{-5} ; 6.7×10^{-6}	
k	5.1×10^{-3} ; 1.4×10^{-5}	
ϵ	2.9×10^{-3} ; 1.5×10^{-5}	

 Table C.33: Details of numerical simulation: Pipe flow unstructured mesh, 2ndhr, $k - \epsilon$

Solution variable	Value	Comment
Run time	01:19	
Total number of iterations	14	Started with UDS, $k - \epsilon$ solution
Advection time	0.026 s	
False time step	0.428 s	
Target RMS residual	1×10^{-5}	
Error convergence		
U Momentum	1.4×10^{-3} ; 9.2×10^{-6}	
V Momentum	2.8×10^{-6} ; 1.3×10^{-7}	
W Momentum	2.9×10^{-6} ; 1.4×10^{-7}	
Continuity	1.3×10^{-6} ; 8.5×10^{-8}	
k	1.7×10^{-2} ; 8.4×10^{-5}	
ω	1.3×10^{-5} ; 2.0×10^{-5}	

Table C.34: Details of numerical simulation: Pipe flow unstructured mesh, UDS, SST

Solution variable	Value	Comment
Run time	01:59	
Total number of iterations	26	Started with UDS, SST solution
Advection time	0.026 s	
False time step	0.1 s	
Target RMS residual	1×10^{-5}	
Error convergence		
U Momentum	1.2×10^{-4} ; 9.6×10^{-6}	
V Momentum	5.9×10^{-7} ; 1.4×10^{-7}	
W Momentum	6.2×10^{-7} ; 1.4×10^{-7}	
Continuity	6.0×10^{-7} ; 1.2×10^{-7}	
k	8.5×10^{-4} ; 1.5×10^{-5}	
ω	2.8×10^{-4} ; 4.5×10^{-6}	

Table C.35: Details of numerical simulation: Pipe flow unstructured mesh, 2nd, SST

Solution variable	Value	Comment
Run time	07:40	
Total number of iterations	94	Started with UDS, $k - \epsilon$ solution
Advection time	0.026 s	
False time step	0.0066 s	
Target RMS residual	1×10^{-5}	
Error convergence		
U Momentum	1.4×10^{-3} ; 1.2×10^{-5}	Error stabilised after 86 iterations
V Momentum	2.3×10^{-5} ; 2.0×10^{-7}	
W Momentum	2.5×10^{-5} ; 1.9×10^{-7}	
Continuity	1.3×10^{-6} ; 2.6×10^{-7}	
k	1.7×10^{-2} ; 2.8×10^{-5}	
ω	1.3×10^{-2} ; 5.1×10^{-6}	

Table C.36: Details of numerical simulation: Pipe flow unstructured mesh, 2ndhr, SST

C.5 Two-dimensional diffuser

Solution variable	Value	Comment
Run time	00:56	
Total number of iterations	37	
Advection time	0.017 s	
False time step	0.003 s	
Target RMS residual	1×10^{-4}	
Error convergence		
U Momentum	3.3×10^{-3} ; 9.4×10^{-5}	
V Momentum	3.1×10^{-4} ; 4.4×10^{-7}	
W Momentum	3.4×10^{-4} ; 6.4×10^{-6}	
Continuity	4.8×10^{-4} ; 7.1×10^{-7}	
k	3.6×10^{-3} ; 4.7×10^{-4}	
ϵ	5.9×10^{-2} ; 3.1×10^{-5}	

Table C.37: Details of numerical simulation: 2D asymmetric diffuser, UDS, $k - \epsilon$

Solution variable	Value	Comment
Run time	03:53	
Total number of iterations	125	Started with UDS, $k - \epsilon$ solution
Advection time	0.017 s	
False time step	0.004 s	
Target RMS residual	1×10^{-5}	
Error convergence		
U Momentum	3.4×10^{-4} ; 9.9×10^{-6}	
V Momentum	9.1×10^{-6} ; 2.7×10^{-8}	
W Momentum	1.2×10^{-4} ; 3.0×10^{-7}	
Continuity	2.5×10^{-5} ; 2.8×10^{-8}	
k	6.9×10^{-4} ; 9.5×10^{-6}	
ϵ	1.4×10^{-3} ; 1.8×10^{-6}	

Table C.38: Details of numerical simulation: 2D asymmetric diffuser, 2ndhr, $k - \epsilon$

Solution variable	Value	Comment
Run time	06:59	
Total number of iterations	210	Started with UDS, $k - \varepsilon$ solution
Advection time	0.017 s	
False time step	0.004 s	
Target RMS residual	1×10^{-5}	
Error convergence		
U Momentum	3.2×10^{-3} ; 9.0×10^{-6}	
V Momentum	1.1×10^{-5} ; 9.2×10^{-8}	
W Momentum	1.3×10^{-4} ; 1.3×10^{-6}	
Continuity	3.9×10^{-5} ; 6.8×10^{-8}	
k	1.3×10^{-1} ; 6.7×10^{-6}	
ω	7.6×10^{-2} ; 9.0×10^{-7}	

Table C.39: Details of numerical simulation: 2D asymmetric diffuser, 2ndhr, SST

C.6 M2129 inlet

C.6.1 Low mass flow case

Solution variable	Value	Comment
Run time	03:15	
Total number of iterations	100	
Advection time	0.0044 s	
False time step	0.0025 s	
Target RMS residual	1×10^{-4}	
Error convergence		
U Momentum	7.7×10^{-3} ; 1.2×10^{-4}	Error stabilised after 60 iterations
V Momentum	5.3×10^{-3} ; 7.7×10^{-6}	Error stabilised after 60 iterations
W Momentum	9.1×10^{-3} ; 2.3×10^{-5}	Error stabilised after 60 iterations
Continuity	1.6×10^{-3} ; 8.2×10^{-7}	Error stabilised after 60 iterations
Energy	8.9×10^{-5} ; 2.7×10^{-6}	
k	1.3×10^{-1} ; 1.8×10^{-3}	Error stabilised after 40 iterations
ϵ	9.1×10^{-2} ; 8.2×10^{-4}	Error stabilised after 40 iterations

Table C.40: Details of numerical simulation: M2129 inlet, UDS, $k - \epsilon$

Solution variable	Value	Comment
Run time	07:26	
Total number of iterations	200	Started with UDS, $k - \epsilon$ solution
Advection time	0.0045 s	
False time step	0.0006 s	
Target RMS residual	1×10^{-5}	
Error convergence		
U Momentum	2.4×10^{-2} ; 1.9×10^{-4}	Error stabilised after 100 iterations
V Momentum	1.3×10^{-2} ; 5.9×10^{-4}	Error stabilised after 50 iterations
W Momentum	1.3×10^{-2} ; 6.0×10^{-4}	Error stabilised after 50 iterations
Continuity	8.1×10^{-3} ; 1.4×10^{-5}	Error stabilised after 130 iterations
Energy	1.3×10^{-4} ; 4.6×10^{-6}	Error stabilised after 100 iterations
k	4.3×10^{-2} ; 2.0×10^{-4}	Error stabilised after 100 iterations
ϵ	2.5×10^{-2} ; 2.6×10^{-4}	Error stabilised after 100 iterations

Table C.41: Details of numerical simulation: M2129 inlet, 2ndhr, $k - \epsilon$

Solution variable	Value	Comment
Run time	04:58	
Total number of iterations	120	Started with UDS, $k - \varepsilon$ solution
Advection time	0.0045 s	
False time step	0.0006 s	
Target RMS residual	1×10^{-5}	
Error convergence		
U Momentum	2.4×10^{-2} ; 2.4×10^{-4}	Error stabilised after 80 iterations
V Momentum	1.3×10^{-2} ; 7.9×10^{-4}	Error stabilised after 40 iterations
W Momentum	1.3×10^{-2} ; 9.8×10^{-4}	Error stabilised after 40 iterations
Continuity	8.1×10^{-3} ; 1.6×10^{-5}	Error stabilised after 100 iterations
Energy	1.3×10^{-4} ; 2.2×10^{-6}	
k	4.3×10^{-2} ; 1.7×10^{-4}	
ω	2.5×10^{-2} ; 4.0×10^{-4}	Error stabilised after 60 iterations

Table C.42: Details of numerical simulation: M2129 inlet, 2ndhr, SST

C.6.2 High mass flow case

Solution variable	Value	Comment
Run time	02:03	
Total number of iterations	56	
Advection time	0.0022 s	
False time step	0.0025 s	
Target RMS residual	1×10^{-4}	
Error convergence		
U Momentum	1.5×10^{-1} ; 4.5×10^{-4}	Error stabilised after 40 iterations
V Momentum	2.3×10^{-3} ; 1.1×10^{-4}	Error stabilised after 25 iterations
W Momentum	3.4×10^{-3} ; 1.3×10^{-4}	Error stabilised after 25 iterations
Continuity	3.2×10^{-2} ; 3.7×10^{-6}	Error stabilised after 35 iterations
Energy	2.3×10^{-4} ; 6.4×10^{-5}	Error stabilised after 40 iterations
k	4.4×10^{-2} ; 2.6×10^{-3}	Error stabilised after 20 iterations
ϵ	5.9×10^{-2} ; 9.3×10^{-3}	Error stabilised after 20 iterations

Table C.43: Details of numerical simulation: M2129 inlet, UDS, $k - \epsilon$

Solution variable	Value	Comment
Run time	07:36	
Total number of iterations	200	Started with UDS, $k - \epsilon$ solution
Advection time	0.0045 s	
False time step	0.0006 s	
Target RMS residual	1×10^{-5}	
Error convergence		
U Momentum	2.6×10^{-2} ; 7.1×10^{-4}	Error stabilised after 40 iterations
V Momentum	1.1×10^{-2} ; 4.0×10^{-4}	Error stabilised after 40 iterations
W Momentum	1.3×10^{-2} ; 3.6×10^{-4}	Error stabilised after 40 iterations
Continuity	2.4×10^{-3} ; 1.5×10^{-5}	Error stabilised after 90 iterations
Energy	1.2×10^{-4} ; 2.8×10^{-6}	Error stabilised after 50 iterations
k	7.2×10^{-2} ; 3.4×10^{-3}	Error stabilised after 50 iterations
ϵ	4.7×10^{-2} ; 2.9×10^{-3}	Error stabilised after 80 iterations

Table C.44: Details of numerical simulation: M2129 inlet, 2ndhr, $k - \epsilon$

Solution variable	Value	Comment
Run time	06:01	
Total number of iterations	146	Started with UDS, $k - \varepsilon$ solution
Advection time	0.0045 s	
False time step	0.0006 s	
Target RMS residual	1×10^{-5}	
Error convergence		
U Momentum	2.4×10^{-2} ; 8.9×10^{-4}	Error stabilised after 50 iterations
V Momentum	1.3×10^{-2} ; 4.8×10^{-4}	Error stabilised after 50 iterations
W Momentum	1.3×10^{-2} ; 5.3×10^{-4}	Error stabilised after 50 iterations
Continuity	8.1×10^{-3} ; 2.3×10^{-5}	Error stabilised after 80 iterations
Energy	1.3×10^{-4} ; 3.3×10^{-5}	Error stabilised after 40 iterations
k	4.3×10^{-2} ; 1.3×10^{-3}	Error stabilised after 40 iterations
ω	2.5×10^{-2} ; 3.5×10^{-4}	Error stabilised after 40 iterations

Table C.45: Details of numerical simulation: M2129 inlet, 2ndhr, SST

Appendix D

Details of CFD models for UCAV inlet simulations

The tables in this appendix gives information on the solution variables and convergence history of the simulations that were run to determine the performance of the UCAV inlet.

The tables has the same layout as those for the validation cases. Refer to the preamble of appendix C for further explanation.

D.1 First-order design

D.1.1 Bump down

Solution variable	Value	Comment
Run time	02:37	
Total number of iterations	52	
Advection time	0.085 s	
False time step	0.024 s	Value automatically chosen by CFX
Target RMS residual	1×10^{-5}	
Error convergence		
U Momentum	1.7×10^{-3} ; 8.2×10^{-7}	
V Momentum	3.9×10^{-3} ; 9.9×10^{-6}	
W Momentum	5.3×10^{-3} ; 1.5×10^{-6}	
Continuity	4.0×10^{-3} ; 7.4×10^{-6}	
Energy	1.1×10^{-6} ; 8.9×10^{-8}	
k	1.0×10^{-1} ; 2.9×10^{-6}	
ε	2.0×10^{-2} ; 9.6×10^{-8}	

Table D.1: Details of numerical simulation: $M_\infty = 0.2$, UDS, $k - \varepsilon$

Solution variable	Value	Comment
Run time	06:35	
Total number of iterations	131	
Advection time	0.062 s	
False time step	0.018 s	Value automatically chosen by CFX
Target RMS residual	1×10^{-5}	
Error convergence		
U Momentum	2.4×10^{-3} ; 1.2×10^{-6}	
V Momentum	6.0×10^{-3} ; 1.0×10^{-5}	
W Momentum	7.1×10^{-3} ; 9.1×10^{-7}	
Continuity	5.4×10^{-3} ; 3.8×10^{-6}	
Energy	5.7×10^{-5} ; 8.7×10^{-8}	
k	1.5×10^{-1} ; 1.1×10^{-6}	
ε	3.4×10^{-2} ; 3.9×10^{-8}	

Table D.2: Details of numerical simulation: $M_\infty = 0.3$, UDS, $k - \varepsilon$

Solution variable	Value	Comment
Run time	24:06	
Total number of iterations	480	
Advection time	0.048 s	
False time step	0.0007 s	Value automatically chosen by CFX
Target RMS residual	1×10^{-5}	
Error convergence		
U Momentum	6.7×10^{-3} ; 5.3×10^{-6}	
V Momentum	2.0×10^{-2} ; 9.9×10^{-6}	
W Momentum	1.3×10^{-2} ; 9.6×10^{-6}	
Continuity	1.3×10^{-2} ; 4.8×10^{-6}	
Energy	1.1×10^{-3} ; 8.3×10^{-8}	
k	2.3×10^{-1} ; 6.2×10^{-7}	
ε	6.5×10^{-2} ; 3.6×10^{-7}	

Table D.3: Details of numerical simulation: $M_\infty = 0.4$, UDS, $k - \varepsilon$

Solution variable	Value	Comment
Run time	12:01	
Total number of iterations	239	
Advection time	0.039 s	
False time step	0.0007 s	Value automatically chosen by CFX
Target RMS residual	1×10^{-5}	
Error convergence		
U Momentum	4.5×10^{-3} ; 5.5×10^{-6}	
V Momentum	7.9×10^{-3} ; 7.8×10^{-6}	
W Momentum	8.1×10^{-3} ; 9.9×10^{-6}	
Continuity	1.2×10^{-2} ; 3.8×10^{-6}	
Energy	4.4×10^{-6} ; 8.5×10^{-8}	
k	2.5×10^{-3} ; 7.8×10^{-7}	
ε	2.7×10^{-3} ; 2.7×10^{-7}	

Table D.4: Details of numerical simulation: $M_\infty = 0.5$, UDS, $k - \varepsilon$

Solution variable	Value	Comment
Run time	20:04	
Total number of iterations	397	
Advection time	0.0033 s	
False time step	0.0007 s	Value automatically chosen by CFX
Target RMS residual	1×10^{-5}	
Error convergence		
U Momentum	4.7×10^{-3} ; 4.7×10^{-6}	
V Momentum	1.1×10^{-2} ; 9.6×10^{-6}	
W Momentum	8.3×10^{-3} ; 8.7×10^{-6}	
Continuity	1.3×10^{-2} ; 4.3×10^{-6}	
Energy	1.6×10^{-3} ; 8.5×10^{-8}	
k	2.9×10^{-1} ; 3.1×10^{-6}	
ε	1.1×10^{-1} ; 2.4×10^{-7}	

 Table D.5: Details of numerical simulation: $M_\infty = 0.6$, UDS, $k - \varepsilon$

Solution variable	Value	Comment
Run time	17:28	
Total number of iterations	346	
Advection time	0.028 s	
False time step	0.0007 s	Value automatically chosen by CFX
Target RMS residual	1×10^{-5}	
Error convergence		
U Momentum	4.2×10^{-6} ; 5.4×10^{-6}	
V Momentum	1.0×10^{-2} ; 8.6×10^{-6}	
W Momentum	7.2×10^{-3} ; 9.7×10^{-6}	
Continuity	1.40×10^{-2} ; 4.2×10^{-6}	
Energy	2.1×10^{-3} ; 8.6×10^{-8}	
k	3.4×10^{-1} ; 4.4×10^{-6}	
ε	1.5×10^{-1} ; 7.0×10^{-7}	

 Table D.6: Details of numerical simulation: $M_\infty = 0.7$, UDS, $k - \varepsilon$

Solution variable	Value	Comment
Run time	12:54	
Total number of iterations	257	
Advection time	0.0025 s	
False time step	0.0007 s	Value automatically chosen by CFX
Target RMS residual	1×10^{-5}	
Error convergence		
U Momentum	4.4×10^{-4} ; 5.1×10^{-6}	
V Momentum	3.7×10^{-3} ; 9.5×10^{-6}	
W Momentum	6.3×10^{-4} ; 9.3×10^{-6}	
Continuity	3.2×10^{-3} ; 5.1×10^{-6}	
Energy	2.1×10^{-3} ; 8.5×10^{-8}	
k	2.4×10^{-3} ; 2.9×10^{-6}	
ε	2.1×10^{-4} ; 5.8×10^{-7}	

 Table D.7: Details of numerical simulation: $M_\infty = 0.8$, UDS, $k - \varepsilon$

Solution variable	Value	Comment
Run time	09:45	
Total number of iterations	194	
Advection time	0.022 s	
False time step	0.0007 s	Value automatically chosen by CFX
Target RMS residual	1×10^{-5}	
Error convergence		
U Momentum	3.4×10^{-4} ; 4.5×10^{-6}	
V Momentum	3.0×10^{-3} ; 1.0×10^{-5}	
W Momentum	4.8×10^{-4} ; 8.3×10^{-6}	
Continuity	2.5×10^{-3} ; 5.8×10^{-6}	
Energy	1.0×10^{-3} ; 8.6×10^{-8}	
k	2.2×10^{-3} ; 8.2×10^{-6}	
ε	2.7×10^{-4} ; 1.1×10^{-6}	

 Table D.8: Details of numerical simulation: $M_\infty = 0.9$, UDS, $k - \varepsilon$

D.1.2 Bump up

Solution variable	Value	Comment
Run time	20:40	
Total number of iterations	419	
Advection time	0.039 s	
False time step	0.0007 s	Value automatically chosen by CFX
Target RMS residual	1×10^{-5}	
Error convergence		
U Momentum	4.6×10^{-3} ; 9.9×10^{-7}	
V Momentum	8.2×10^{-3} ; 1.1×10^{-6}	
W Momentum	8.1×10^{-3} ; 1.8×10^{-6}	
Continuity	1.4×10^{-2} ; 5.1×10^{-7}	
Energy	5.3×10^{-6} ; 8.3×10^{-8}	
k	8.1×10^{-1} ; 1.7×10^{-7}	
ε	1.6×10^0 ; 4.6×10^{-8}	

Table D.9: Details of numerical simulation: $M_\infty = 0.5$, UDS, $k - \varepsilon$

Solution variable	Value	Comment
Run time	20:52	
Total number of iterations	422	
Advection time	0.033 s	
False time step	0.007 s	Value automatically chosen by CFX
Target RMS residual	1×10^{-5}	
Error convergence		
U Momentum	9.7×10^{-4} ; 4.2×10^{-6}	
V Momentum	8.0×10^{-3} ; 9.1×10^{-6}	
W Momentum	1.4×10^{-3} ; 7.7×10^{-6}	
Continuity	1.2×10^{-2} ; 4.6×10^{-6}	
Energy	1.6×10^{-3} ; 8.5×10^{-8}	
k	3.4×10^{-3} ; 3.0×10^{-6}	
ε	8.0×10^{-4} ; 9.1×10^{-7}	

Table D.10: Details of numerical simulation: $M_\infty = 0.6$, UDS, $k - \varepsilon$

Solution variable	Value	Comment
Run time	17:12	
Total number of iterations	346	
Advection time	0.028 s	
False time step	0.0007 s	Value automatically chosen by CFX
Target RMS residual	1×10^{-5}	
Error convergence		
U Momentum	6.8×10^{-4} ; 5.6×10^{-6}	
V Momentum	6.9×10^{-3} ; 9.2×10^{-6}	
W Momentum	9.6×10^{-4} ; 9.5×10^{-6}	
Continuity	8.7×10^{-3} ; 4.8×10^{-6}	
Energy	1.9×10^{-3} ; 8.6×10^{-8}	
k	2.6×10^{-3} ; 3.7×10^{-6}	
ε	7.2×10^{-4} ; 1.4×10^{-6}	

Table D.11: Details of numerical simulation: $M_\infty = 0.7$, UDS, $k - \varepsilon$

Solution variable	Value	Comment
Run time	13:08	
Total number of iterations	262	
Advection time	0.025 s	
False time step	0.0007 s	Value automatically chosen by CFX
Target RMS residual	1×10^{-5}	
Error convergence		
U Momentum	5.0×10^{-4} ; 5.5×10^{-6}	
V Momentum	6.0×10^{-3} ; 9.5×10^{-6}	
W Momentum	7.1×10^{-4} ; 1.0×10^{-5}	
Continuity	6.5×10^{-3} ; 5.8×10^{-6}	
Energy	2.1×10^{-3} ; 8.6×10^{-8}	
k	2.1×10^{-3} ; 4.0×10^{-6}	
ε	6.5×10^{-4} ; 1.6×10^{-6}	

Table D.12: Details of numerical simulation: $M_\infty = 0.8$, UDS, $k - \varepsilon$

Solution variable	Value	Comment
Run time	10:41	
Total number of iterations	211	
Advection time	0.022 s	
False time step	0.0007 s	Value automatically chosen by CFX
Target RMS residual	1×10^{-5}	
Error convergence		
U Momentum	3.8×10^{-4} ; 2.5×10^{-6}	
V Momentum	5.3×10^{-3} ; 9.7×10^{-6}	
W Momentum	5.3×10^{-4} ; 4.6×10^{-6}	
Continuity	5.0×10^{-3} ; 5.4×10^{-6}	
Energy	2.3×10^{-3} ; 8.7×10^{-8}	
k	1.7×10^{-3} ; 5.2×10^{-6}	
ε	6.0×10^{-4} ; 1.9×10^{-6}	

Table D.13: Details of numerical simulation: $M_\infty = 0.9$, UDS, $k - \varepsilon$

D.2 Second-order design

D.2.1 Bump down

Solution variable	Value	Comment
Run time	02:12	
Total number of iterations	29	
Advection time	0.084 s	
False time step	0.022 s	Value automatically chosen by CFX
Target RMS residual	1×10^{-4}	
Error convergence		
U Momentum	9.6×10^{-3} ; 8.4×10^{-5}	
V Momentum	2.7×10^{-3} ; 1.3×10^{-5}	
W Momentum	8.8×10^{-3} ; 1.7×10^{-5}	
Continuity	1.8×10^{-2} ; 6.8×10^{-6}	
Energy	9.8×10^{-5} ; 1.3×10^{-6}	
k	1.2×10^{-1} ; 4.6×10^{-4}	
ε	5.8×10^{-2} ; 1.5×10^{-4}	

Table D.14: Details of numerical simulation: $M_\infty = 0.2$, UDS, $k - \varepsilon$

Solution variable	Value	Comment
Run time	11:41	
Total number of iterations	134	Started with UDS solution
Advection time	0.088 s	
False time step	0.021 s	Value automatically chosen by CFX
Target RMS residual	1×10^{-5}	
Error convergence		
U Momentum	8.3×10^{-3} ; 2.3×10^{-4}	Error stabilised after 26 iterations
V Momentum	3.5×10^{-3} ; 2.9×10^{-4}	Error stabilised after 41 iterations
W Momentum	7.3×10^{-3} ; 2.2×10^{-4}	Error stabilised after 36 iterations
Continuity	1.1×10^{-2} ; 2.8×10^{-6}	Error stabilised after 91 iterations
Energy	3.6×10^{-5} ; 3.6×10^{-6}	Error stabilised after 31 iterations
k	3.0×10^{-2} ; 1.8×10^{-3}	Error stabilised after 18 iterations
ε	7.8×10^{-3} ; 5.9×10^{-4}	Error stabilised after 18 iterations

Table D.15: Details of numerical simulation: $M_\infty = 0.2$, 2ndhr, $k - \varepsilon$

Solution variable	Value	Comment
Run time	02:43	
Total number of iterations	36	
Advection time	0.067 s	
False time step	0.017 s	Value automatically chosen by CFX
Target RMS residual	1×10^{-4}	
Error convergence		
U Momentum	1.6×10^{-2} ; 8.3×10^{-5}	
V Momentum	4.2×10^{-3} ; 7.7×10^{-6}	
W Momentum	1.5×10^{-2} ; 1.4×10^{-5}	
Continuity	2.6×10^{-2} ; 4.7×10^{-6}	
Energy	1.8×10^{-4} ; 2.5×10^{-6}	
k	1.8×10^{-1} ; 9.7×10^{-4}	
ε	9.2×10^{-2} ; 2.3×10^{-4}	

 Table D.16: Details of numerical simulation: $M_\infty = 0.3$, UDS, $k - \varepsilon$

Solution variable	Value	Comment
Run time	16:27	
Total number of iterations	189	Started with UDS solution
Advection time	0.070 s	
False time step	0.017 s	
Target RMS residual	1×10^{-5}	
Error convergence		
U Momentum	1.0×10^{-2} ; 3.3×10^{-4}	Error stabilised after 34 iterations
V Momentum	4.1×10^{-3} ; 3.9×10^{-4}	Error stabilised after 34 iterations
W Momentum	7.5×10^{-3} ; 3.6×10^{-4}	Error stabilised after 34 iterations
Continuity	2.2×10^{-2} ; 2.7×10^{-6}	Error stabilised after 84 iterations
Energy	1.4×10^{-4} ; 8.7×10^{-6}	Error stabilised after 44 iterations
k	5.6×10^{-2} ; 1.0×10^{-3}	Error stabilised after 34 iterations
ε	2.1×10^{-2} ; 6.4×10^{-4}	Error stabilised after 34 iterations

 Table D.17: Details of numerical simulation: $M_\infty = 0.3$, 2ndhr, $k - \varepsilon$

Solution variable	Value	Comment
Run time	07:39	
Total number of iterations	100	
Advection time	0.054 s	
False time step	0.0007 s	Value automatically chosen by CFX
Target RMS residual	1×10^{-4}	
Error convergence		
U Momentum	1.3×10^{-2} ; 9.8×10^{-5}	
V Momentum	6.6×10^{-3} ; 1.6×10^{-5}	
W Momentum	1.4×10^{-2} ; 1.7×10^{-5}	
Continuity	2.4×10^{-2} ; 7.3×10^{-5}	
Energy	3.5×10^{-4} ; 1.4×10^{-6}	
k	1.6×10^{-1} ; 8.3×10^{-4}	
ε	6.9×10^{-2} ; 2.5×10^{-4}	

 Table D.18: Details of numerical simulation: $M_\infty = 0.4$, UDS, $k - \varepsilon$

Solution variable	Value	Comment
Run time	09:04	
Total number of iterations	98	Started with UDS solution
Advection time	0.056 s	
False time step	0.014 s	
Target RMS residual	1×10^{-5}	
Error convergence		
U Momentum	1.2×10^{-2} ; 5.1×10^{-4}	Error stabilised after 30 iterations
V Momentum	6.7×10^{-3} ; 4.6×10^{-4}	Error stabilised after 30 iterations
W Momentum	1.0×10^{-2} ; 3.5×10^{-4}	Error stabilised after 30 iterations
Continuity	3.6×10^{-2} ; 4.8×10^{-6}	Error stabilised after 93 iterations
Energy	2.7×10^{-4} ; 1.5×10^{-5}	Error stabilised after 40 iterations
k	7.3×10^{-2} ; 2.3×10^{-3}	Error stabilised after 30 iterations
ε	3.1×10^{-2} ; 6.4×10^{-4}	Error stabilised after 30 iterations

 Table D.19: Details of numerical simulation: $M_\infty = 0.4$, 2ndhr, $k - \varepsilon$

Solution variable	Value	Comment
Run time	11:33	
Total number of iterations	150	
Advection time	0.044 s	
False time step	0.0007 s	Value automatically chosen by CFX
Target RMS residual	1×10^{-4}	
Error convergence		
U Momentum	1.4×10^{-2} ; 1.0×10^{-4}	
V Momentum	5.8×10^{-3} ; 1.0×10^{-5}	
W Momentum	1.2×10^{-2} ; 1.5×10^{-5}	
Continuity	2.8×10^{-2} ; 5.7×10^{-5}	
Energy	5.3×10^{-4} ; 1.3×10^{-6}	
k	4.3×10^{-2} ; 2.3×10^{-3}	
ε	4.9×10^{-2} ; 7.3×10^{-4}	

 Table D.20: Details of numerical simulation: $M_\infty = 0.5$, UDS, $k - \varepsilon$

Solution variable	Value	Comment
Run time	14:13	
Total number of iterations	163	Started with UDS solution
Advection time	0.047 s	
False time step	0.011 s	
Target RMS residual	1×10^{-5}	
Error convergence		
U Momentum	1.3×10^{-2} ; 6.5×10^{-4}	Error stabilised after 50 iterations
V Momentum	6.5×10^{-3} ; 6.3×10^{-4}	Error stabilised after 50 iterations
W Momentum	8.6×10^{-3} ; 4.5×10^{-4}	Error stabilised after 50 iterations
Continuity	4.1×10^{-2} ; 8.9×10^{-6}	Error stabilised after 100 iterations
Energy	4.3×10^{-4} ; 2.8×10^{-5}	Error stabilised after 30 iterations
k	7.5×10^{-2} ; 6.0×10^{-3}	Error stabilised after 50 iterations
ε	3.2×10^{-2} ; 8.9×10^{-4}	Error stabilised after 50 iterations

 Table D.21: Details of numerical simulation: $M_\infty = 0.5$, 2ndhr, $k - \varepsilon$

Solution variable	Value	Comment
Run time	11:12	
Total number of iterations	150	
Advection time	0.038 s	
False time step	0.0007 s	Value automatically chosen by CFX
Target RMS residual	1×10^{-4}	
Error convergence		
U Momentum	1.6×10^{-2} ; 2.4×10^{-4}	Error stabilised after 120 iterations
V Momentum	5.1×10^{-3} ; 3.8×10^{-5}	
W Momentum	9.7×10^{-3} ; 2.7×10^{-5}	
Continuity	3.2×10^{-2} ; 3.2×10^{-5}	
Energy	7.5×10^{-4} ; 7.3×10^{-6}	
k	1.7×10^{-1} ; 2.1×10^{-3}	
ε	4.7×10^{-2} ; 1.5×10^{-3}	

 Table D.22: Details of numerical simulation: $M_\infty = 0.6$, UDS, $k - \varepsilon$

Solution variable	Value	Comment
Run time	08:30	
Total number of iterations	91	Started with UDS solution
Advection time	0.040 s	
False time step	0.009 s	
Target RMS residual	1×10^{-5}	
Error convergence		
U Momentum	1.4×10^{-2} ; 7.4×10^{-4}	Error stabilised after 50 iterations
V Momentum	1.0×10^{-2} ; 6.4×10^{-4}	Error stabilised after 20 iterations
W Momentum	1.2×10^{-2} ; 5.5×10^{-4}	Error stabilised after 30 iterations
Continuity	4.8×10^{-2} ; 2.6×10^{-5}	Error stabilised after 70 iterations
Energy	6.4×10^{-4} ; 7.9×10^{-5}	Error stabilised after 50 iterations
k	7.2×10^{-2} ; 5.1×10^{-3}	Error stabilised after 50 iterations
ε	3.1×10^{-2} ; 1.3×10^{-3}	Error stabilised after 50 iterations

 Table D.23: Details of numerical simulation: $M_\infty = 0.6$, 2ndhr, $k - \varepsilon$

Solution variable	Value	Comment
Run time	07:56	
Total number of iterations	100	
Advection time	0.034 s	
False time step	0.0007 s	Value automatically chosen by CFX
Target RMS residual	1×10^{-4}	
Error convergence		
U Momentum	1.7×10^{-2} ; 3.7×10^{-4}	Error stabilised after 50 iterations
V Momentum	4.8×10^{-3} ; 7.2×10^{-5}	
W Momentum	8.8×10^{-3} ; 7.8×10^{-5}	
Continuity	3.4×10^{-2} ; 1.0×10^{-4}	
Energy	9.9×10^{-4} ; 1.5×10^{-5}	
k	1.8×10^{-1} ; 2.2×10^{-3}	
ε	8.6×10^{-2} ; 9.9×10^{-4}	

 Table D.24: Details of numerical simulation: $M_\infty = 0.7$, UDS, $k - \varepsilon$

Solution variable	Value	Comment
Run time	05:48	
Total number of iterations	162	Started with UDS solution
Advection time	0.034 s	
False time step	0.004 s	
Target RMS residual	1×10^{-5}	
Error convergence		
U Momentum	1.4×10^{-2} ; 8.4×10^{-4}	Error stabilised after 20 iterations
V Momentum	9.8×10^{-3} ; 6.4×10^{-4}	Error stabilised after 25 iterations
W Momentum	1.1×10^{-2} ; 5.7×10^{-4}	Error stabilised after 35 iterations
Continuity	4.5×10^{-2} ; 2.2×10^{-5}	Error stabilised after 35 iterations
Energy	7.0×10^{-4} ; 1.0×10^{-4}	Error stabilised after 25 iterations
k	7.7×10^{-2} ; 7.8×10^{-3}	Error stabilised after 30 iterations
ε	3.2×10^{-2} ; 3.2×10^{-3}	Error stabilised after 30 iterations

 Table D.25: Details of numerical simulation: $M_\infty = 0.7$, 2ndhr, $k - \varepsilon$

Solution variable	Value	Comment
Run time	11:14	
Total number of iterations	150	
Advection time	0.03 s	
False time step	0.0007 s	Value automatically chosen by CFX
Target RMS residual	1×10^{-4}	
Error convergence		
U Momentum	1.8×10^{-2} ; 4.3×10^{-4}	
V Momentum	4.6×10^{-3} ; 1.0×10^{-4}	
W Momentum	8.3×10^{-3} ; 9.8×10^{-5}	
Continuity	3.7×10^{-2} ; 8.1×10^{-5}	
Energy	1.2×10^{-3} ; 2.9×10^{-5}	
k	1.9×10^{-1} ; 3.4×10^{-3}	
ε	1.1×10^{-1} ; 1.3×10^{-3}	

 Table D.26: Details of numerical simulation: $M_\infty = 0.8$, UDS, $k - \varepsilon$

Solution variable	Value	Comment
Run time	08:45	
Total number of iterations	53	Started with UDS solution
Advection time	0.03 s	
False time step	0.003 s	
Target RMS residual	1×10^{-5}	
Error convergence		
U Momentum	1.5×10^{-2} ; 1.0×10^{-3}	Error stabilised after 30 iterations
V Momentum	1.4×10^{-2} ; 6.5×10^{-4}	Error stabilised after 20 iterations
W Momentum	1.5×10^{-2} ; 5.0×10^{-4}	Error stabilised after 20 iterations
Continuity	1.4×10^{-3} ; 2.3×10^{-5}	Error stabilised after 30 iterations
Energy	4.5×10^{-4} ; 1.2×10^{-4}	Error stabilised after 20 iterations
k	6.2×10^{-2} ; 4.6×10^{-3}	Error stabilised after 20 iterations
ε	3.1×10^{-2} ; 1.7×10^{-3}	Error stabilised after 20 iterations

 Table D.27: Details of numerical simulation: $M_\infty = 0.8$, 2ndhr, $k - \varepsilon$

Solution variable	Value	Comment
Run time	11:14	
Total number of iterations	150	
Advection time	0.028 s	
False time step	0.0007 s	Value automatically chosen by CFX
Target RMS residual	1×10^{-4}	
Error convergence		
U Momentum	1.9×10^{-2} ; 4.0×10^{-4}	Error stabilised after 80 iterations
V Momentum	4.6×10^{-3} ; 1.2×10^{-4}	Error stabilised after 80 iterations
W Momentum	8.1×10^{-3} ; 1.1×10^{-4}	Error stabilised after 80 iterations
Continuity	4.0×10^{-4} ; 6.7×10^{-5}	Error stabilised after 80 iterations
Energy	1.5×10^{-3} ; 3.0×10^{-5}	Error stabilised after 80 iterations
k	2.1×10^{-1} ; 3.1×10^{-3}	Error stabilised after 80 iterations
ε	9.9×10^{-2} ; 1.3×10^{-3}	Error stabilised after 80 iterations

 Table D.28: Details of numerical simulation: $M_\infty = 0.9$, UDS, $k - \varepsilon$

Solution variable	Value	Comment
Run time	23:41	
Total number of iterations	141	Started with UDS solution
Advection time	0.027 s	
False time step	0.0025 s	
Target RMS residual	1×10^{-5}	
Error convergence		
U Momentum	1.5×10^{-2} ; 9.9×10^{-4}	Error stabilised after 30 iterations
V Momentum	1.1×10^{-2} ; 6.9×10^{-4}	Error stabilised after 30 iterations
W Momentum	1.2×10^{-2} ; 5.5×10^{-4}	Error stabilised after 30 iterations
Continuity	4.5×10^{-2} ; 1.6×10^{-5}	Error stabilised after 90 iterations
Energy	5.4×10^{-4} ; 1.5×10^{-4}	Error stabilised after 30 iterations
k	8.6×10^{-2} ; 6.5×10^{-3}	Error stabilised after 30 iterations
ε	3.5×10^{-2} ; 5.4×10^{-3}	Error stabilised after 30 iterations

 Table D.29: Details of numerical simulation: $M_\infty = 0.9$, 2ndhr, $k - \varepsilon$

D.2.2 Bump up

Solution variable	Value	Comment
Run time	11:12	
Total number of iterations	144	
Advection time	0.044 s	
False time step	0.0007 s	Value automatically chosen by CFX
Target RMS residual	1×10^{-4}	
Error convergence		
U Momentum	1.4×10^{-2} ; 1.0×10^{-4}	
V Momentum	5.9×10^{-3} ; 2.4×10^{-5}	
W Momentum	1.1×10^{-2} ; 3.4×10^{-5}	
Continuity	2.8×10^{-2} ; 5.8×10^{-5}	
Energy	5.3×10^{-4} ; 2.1×10^{-6}	
k	1.7×10^{-1} ; 1.1×10^{-3}	
ε	7.3×10^{-2} ; 4.8×10^{-4}	

Table D.30: Details of numerical simulation: $M_\infty = 0.5$, UDS, $k - \varepsilon$

Solution variable	Value	Comment
Run time	22:23	
Total number of iterations	250	Started with UDS solution
Advection time	0.046 s	
False time step	0.0007 s	Value automatically chosen by CFX
Target RMS residual	1×10^{-5}	
Error convergence		
U Momentum	1.3×10^{-2} ; 4.8×10^{-4}	Error stabilised after 100 iterations
V Momentum	3.7×10^{-3} ; 5.8×10^{-4}	Error stabilised after 50 iterations
W Momentum	6.9×10^{-3} ; 3.8×10^{-4}	Error stabilised after 50 iterations
Continuity	3.0×10^{-2} ; 6.0×10^{-6}	Error stabilised after 200 iterations
Energy	2.9×10^{-4} ; 1.5×10^{-5}	Error stabilised after 150 iterations
k	7.3×10^{-2} ; 1.7×10^{-3}	Error stabilised after 100 iterations
ε	4.0×10^{-2} ; 4.0×10^{-4}	Error stabilised after 100 iterations

Table D.31: Details of numerical simulation: $M_\infty = 0.5$, 2ndhr, $k - \varepsilon$

Solution variable	Value	Comment
Run time	11:42	
Total number of iterations	145	
Advection time	0.037 s	
False time step	0.0007 s	Value chosen automatically by CFX
Target RMS residual	1×10^{-4}	
Error convergence		
U Momentum	1.6×10^{-2} ; 1.4×10^{-4}	
V Momentum	5.4×10^{-3} ; 4.4×10^{-5}	
W Momentum	9.5×10^{-3} ; 3.3×10^{-5}	
Continuity	3.2×10^{-2} ; 3.8×10^{-5}	
Energy	7.4×10^{-4} ; 4.3×10^{-6}	
k	1.8×10^{-1} ; 8.6×10^{-4}	
ε	8.2×10^{-2} ; 4.5×10^{-4}	

 Table D.32: Details of numerical simulation: $M_\infty = 0.6$, UDS, $k - \varepsilon$

Solution variable	Value	Comment
Run time	42:16	
Total number of iterations	250	Started with UDS solution
Advection time	0.039 s	
False time step	0.0007 s	Value chosen automatically by CFX
Target RMS residual	1×10^{-5}	
Error convergence		
U Momentum	1.4×10^{-2} ; 5.0×10^{-4}	
V Momentum	1.0×10^{-2} ; 6.0×10^{-5}	Error stabilised after 100 iterations
W Momentum	1.2×10^{-2} ; 4.4×10^{-4}	Error stabilised after 100 iterations
Continuity	3.5×10^{-2} ; 1.5×10^{-5}	
Energy	3.2×10^{-4} ; 1.2×10^{-5}	Error stabilised after 150 iterations
k	1.9×10^{-2} ; 1.5×10^{-3}	Error stabilised after 100 iterations
ε	1.8×10^{-2} ; 7.1×10^{-3}	Error stabilised after 100 iterations

 Table D.33: Details of numerical simulation: $M_\infty = 0.6$, 2ndhr, $k - \varepsilon$

Solution variable	Value	Comment
Run time	11:41	
Total number of iterations	150	
Advection time	0.033 s	
False time step	0.0007 s	Value chosen automatically by CFX
Target RMS residual	1×10^{-4}	
Error convergence		
U Momentum	1.7×10^{-2} ; 2.4×10^{-4}	
V Momentum	5.1×10^{-3} ; 8.8×10^{-5}	
W Momentum	8.8×10^{-3} ; 8.6×10^{-5}	
Continuity	3.5×10^{-2} ; 1.8×10^{-5}	
Energy	9.7×10^{-4} ; 1.4×10^{-5}	
k	1.9×10^{-1} ; 1.9×10^{-3}	
ε	1.0×10^{-1} ; 6.7×10^{-4}	

 Table D.34: Details of numerical simulation: $M_\infty = 0.7$, UDS, $k - \varepsilon$

Solution variable	Value	Comment
Run time	42:47	
Total number of iterations	250	Started with UDS solution
Advection time	0.034 s	
False time step	0.0007 s	Value chosen automatically by CFX
Target RMS residual	1×10^{-5}	
Error convergence		
U Momentum	1.4×10^{-2} ; 4.6×10^{-4}	Error stabilised after 200 iterations
V Momentum	1.3×10^{-2} ; 5.9×10^{-4}	Error stabilised after 100 iterations
W Momentum	1.4×10^{-2} ; 4.7×10^{-4}	Error stabilised after 100 iterations
Continuity	3.7×10^{-2} ; 1.1×10^{-5}	
Energy	4.1×10^{-4} ; 2.9×10^{-5}	Error stabilised after 100 iterations
k	5.5×10^{-2} ; 8.3×10^{-4}	Error stabilised after 100 iterations
ε	2.2×10^{-3} ; 0.0×10^{-0}	Error stabilised after 100 iterations

 Table D.35: Details of numerical simulation: $M_\infty = 0.7$, 2ndhr, $k - \varepsilon$

Solution variable	Value	Comment
Run time	08:54	
Total number of iterations	111	
Advection time	0.031 s	
False time step	0.0007 s	Value chosen automatically by CFX
Target RMS residual	1×10^{-4}	
Error convergence		
U Momentum	1.8×10^{-2} ; 2.7×10^{-4}	
V Momentum	4.9×10^{-3} ; 1.1×10^{-4}	
W Momentum	8.4×10^{-3} ; 8.8×10^{-5}	
Continuity	3.8×10^{-2} ; 9.7×10^{-5}	
Energy	1.2×10^{-3} ; 1.7×10^{-5}	
k	2.1×10^{-1} ; 1.1×10^{-3}	
ε	1.1×10^{-1} ; 7.2×10^{-4}	

 Table D.36: Details of numerical simulation: $M_\infty = 0.8$, UDS, $k - \varepsilon$

Solution variable	Value	Comment
Run time	42:57	
Total number of iterations	250	Started with UDS solution
Advection time	0.030 s	
False time step	0.0007 s	Value chosen automatically by CFX
Target RMS residual	1×10^{-5}	
Error convergence		
U Momentum	1.4×10^{-2} ; 7.1×10^{-4}	Error stabilised after 100 iterations
V Momentum	8.9×10^{-3} ; 7.2×10^{-4}	Error stabilised after 100 iterations
W Momentum	1.0×10^{-2} ; 5.1×10^{-4}	Error stabilised after 100 iterations
Continuity	4.1×10^{-2} ; 1.3×10^{-5}	
Energy	5.0×10^{-4} ; 6.8×10^{-5}	Error stabilised after 150 iterations
k	5.1×10^{-2} ; 5.6×10^{-3}	Error stabilised after 150 iterations
ε	3.4×10^{-2} ; 1.9×10^{-3}	Error stabilised after 150 iterations

 Table D.37: Details of numerical simulation: $M_\infty = 0.8$, 2ndhr, $k - \varepsilon$

Solution variable	Value	Comment
Run time	11:57	
Total number of iterations	150	
Advection time	0.028 s	
False time step	0.0007 s	Value chosen automatically by CFX
Target RMS residual	1×10^{-4}	
Error convergence		
U Momentum	1.8×10^{-2} ; 3.6×10^{-4}	
V Momentum	4.8×10^{-3} ; 1.1×10^{-4}	
W Momentum	8.1×10^{-3} ; 1.2×10^{-4}	
Continuity	4.1×10^{-2} ; 7.6×10^{-5}	
Energy	1.5×10^{-3} ; 2.7×10^{-5}	
k	2.1×10^{-1} ; 1.4×10^{-3}	
ε	9.6×10^{-2} ; 8.3×10^{-4}	

 Table D.38: Details of numerical simulation: $M_\infty = 0.9$, UDS, $k - \varepsilon$

Solution variable	Value	Comment
Run time	18:24	2000 MHz Intel P4, 1GB RAM
Total number of iterations	250	Started with UDS solution
Advection time	0.027 s	
False time step	0.0007 s	Value chosen automatically by CFX
Target RMS residual	1×10^{-5}	
Error convergence		
U Momentum	1.3×10^{-2} ; 6.9×10^{-4}	Error stabilised after 100 iterations
V Momentum	3.6×10^{-3} ; 5.9×10^{-4}	Error stabilised after 30 iterations
W Momentum	4.0×10^{-3} ; 4.9×10^{-4}	Error stabilised after 30 iterations
Continuity	4.2×10^{-2} ; 1.2×10^{-5}	
Energy	7.4×10^{-4} ; 9.6×10^{-5}	Error stabilised after 70 iterations
k	4.0×10^{-2} ; 3.4×10^{-3}	Error stabilised after 120 iterations
ε	3.8×10^{-2} ; 1.6×10^{-3}	Error stabilised after 120 iterations

 Table D.39: Details of numerical simulation: $M_\infty = 0.9$, 2ndhr, $k - \varepsilon$

References

- [1] Paterson J. - "Measuring Low Observable Technology's Effects on Combat Aircraft Survivability", AIAA-975544, SAE Transactions on Aerospace, 1997, pp.1515-27
- [2] Piccirillo Albert C. - "The Have Blue Technology Demonstrator and Radar Cross Section Reduction", AIAA-965538, SAE Transactions on Aerospace, 1996, pp. 1348-60
- [3] Aronstein, David C. and Piccirillo, Albert C. - *Have Blue and the F-117A: Evolution of the "Stealth Fighter"*, American Institute of Aeronautics and Astronautics, 1997
- [4] Knott E.F. - *Radar Cross Section, Second Edition*, Chapter 7: "Radar Cross Section Reduction", Artech House, 1993
- [5] Seddon, J. and Goldsmith, E.L. - *Intake Aerodynamics, Second Edition*, Blackwell Science Ltd., 1999
- [6] Oates, Gordon C. - *Aircraft Propulsion Systems Technology and Design*, AIAA Educational Series
- [7] US Navy Unmanned Air Vehicles Web Site:
<http://uav.navair.navy.mil/ucavn/default.htm>
Last access date: 11/06/2003
- [8] Janes Military Aerospace Web Site:
http://www.janes.com/aerospace/military/news/idr/idr010504_1_n.shtml
Last access date: 11/06/2003
- [9] White, F.M. - *Viscous Fluid Flow, Second Edition*, McGraw-Hill, 1991
- [10] CFX technical support, personal communication, March - May 2003
- [11] Houghton, E.L. and Carpenter, P.W. - *Aerodynamics for Engineering Students, Fourth Edition*, Arnold, 1993
- [12] White, F.M. - *Fluid Mechanics, Third Edition*, McGraw-Hill, 1994
- [13] Fox and MacDonald - *Introduction to Fluid Mechanics, Fifth edition*, John Wiley and Sons, 1999
- [14] Proceedings of 8th Workshop on Refined Turbulence modelling in Espoo, Finland, 17-18 June 1999:
<http://www.cfdthermo.hut.fi/wshop99/proceedings/>
Last access date: 11/06/2003

- [15] Fluid Dynamics Panel, Working Group 13- “Test Case 3 - Subsonic / Transonic Circular Intake”, AGARD Advisory Report 270, pp. 139-162, 1991
- [16] Menzies, R.D.D, Badcock, K.J. et al - “Validation of the simulation of flow in an S-duct”, AIAA-2002-2808, 20th Applied Aerodynamics Conference, June 24-27 2002, St. Louis, Missouri, USA
- [17] Menzies, R.D.D, Personal Communication, January 2003
- [18] AEA Technologies, CFX-5 Solver and Solver Manager manual, 2002
- [19] Ferziger, Joel H. and Perić, Milovan - *Computational Methods for Fluid Dynamics*, Springer, Berlin, 1996
- [20] Popular Science Website:
<http://www.popsci.com/popsci/aviation/article/0,12543,365576-3,00.html>
Last access date: 11/06/2003
- [21] Microturbo Inc. Web Site:
http://www.microturbo-usa.com/Products/Turbojet/Tri_60.htm
Last access date: 11/06/2003
- [22] Anderson, John D. - *Modern Compressible Flow with historical perspective, Second Edition*, McGraw-Hill, 1990
- [23] Thiart, G.D. - *Course notes for Numerical Fluid Dynamics 844*, Department of Mechanical Engineering, University of Stellenbosch, 2000
- [24] AEA Technologies, Installation & Introduction to CFX-5, 2002
- [25] AEA Technologies, CFX-Build Users manual, Chapter 9, 2002
- [26] Menter, F.R. - “Two-Equation Eddy-Viscosity Turbulence Models for Engineering Applications”, AIAA Journal, Volume 32 number 8, 1994, pp.1598-1605
- [27] Wilcox, D.C. - “Reassessment of the Scale-Determining Equation for Advanced Turbulence Models”, AIAA Journal, Volume 26 number 11, 1988, pp.1299-1310
- [28] Johnson, D.A. and King, L.S. - “Mathematically Simple Turbulence Closure Model for Attached and Separated Turbulent Boundary Layers”, AIAA Journal, Volume 23 number 11, 1985, pp.1684-1692
- [29] Driver, D.M. - “Reynolds Shear Stress Measurements in a Separated Boundary Layer”, AIAA Paper 91-1787, June 1991